ASSESSMENT OF THE THERAPEUTIC EFFECTS OF OKN-007 IN RODENT GLIOMA MODELS USING ADVANCED MRI TECHNIQUES

By

PATRICIA COUTINHO DE SOUZA

Master of Science in Experimental and Comparative
Pathology
University of São Paulo
São Paulo, SP
2010

Doctor of Veterinary Medicine
Federal University of Viçosa
Viçosa, MG
2005

Submitted to the Faculty of the
Graduate College of the
Oklahoma State University
in partial fulfillment of
the requirements for
the Degree of
DOCTOR OF PHILOSOPHY
May, 2015

ASSESSMENT OF THE THERAPEUTIC EFFECTS OF OKN-007 IN RODENT GLIOMA MODELS USING ADVANCED MRI TECHNIQUES

Dissertation Approved:

Rheal A. Towner

Dissertation Adviser

Jerry W. Ritchey

Melanie Breshears

Ashish Ranjan

Daqing Piao

Timothy Mather

Adjunct Faculty, *Ex officio* member

ACKNOWLEDGEMENTS

First and foremost, I would like to dedicate this dissertation to the memory of my esteemed friend Judith Kathleen Jenlink. Judy walked into my life on September 2010. She was a volunteer English teacher at the Stillwater Public Library, and for 15 months I had the enormous privilege of being her student. Judy was an extraordinary teacher, and she touched my life in a profound, unique, and special way. I will be always thankful for all her noble advices to my graduate program and personal life.

I am also grateful to God for being in every moment of my life and never left my side. Thank You for the constant direction and strength throughout this entire journey.

I would like also to express my sincerest gratitude and respect to my supervisor Dr Rheal Towner, who has dedicated his time and efforts towards the accomplishment of this dissertation. His valuable contributions and guidance, always suggested with a remarkable kindness, gave me enough encouragement and motivation to achieve this present work.

A very special thanks to Dr Jerry Ritchey for the outstanding supervision and constant inspiration. Thank you also for keeping your office door open and available for all the times when I needed it.

Furthermore, I would like to thank all members of my committee for their diligence, guidance, patience, and support through this arduous journey. I am very grateful to you all!

A special thank you to Debra Saunders and Nataliya Smith for their friendship and immeasurable support.

I am also very grateful to Dr Kar-Ming Fung for being a fundamental support to make this work feasible.

I extend my appreciation to my great and amazing friend Dr Sonia Crochik, for her immeasurable patience, precious comments, and invaluable advices.

I am also thankful for my family and new friends I have met in Oklahoma; you are loved, appreciated, and remembered.

Many thanks to Piotr Choroszczak for his friendship and for always listening to me.

I would like also to thank Jesse Espolt for his endless love, encouragement, kindness, and support during all this process.

Last but not least, I gratefully acknowledge Oklahoma State University and Oklahoma Medical Research Foundation for their financial support, which allowed me to pursue this unique and unforgettable opportunity to reach my academic and career goals.

Name: PATRICIA COUTINHO DE SOUZA

Date of Degree: MAY, 2015

Title of Study: ASSESSMENT OF THE THERAPEUTIC EFFECTS OF OKN-007 IN RODENT GLIOMA MODELS USING ADVANCED MRI TECHNIQUES

Major Field: VETERINARY BIOMEDICAL SCIENCES

Abstract: Glioblastoma is a malignant grade IV glioma with a poor prognosis in humans. New therapeutics are desperately required. The nitrone OKN-007 (2,4-disulfophenyl-PBN) has demonstrated effective anti-glioma properties in several rodent models and is currently being used as a clinical investigational drug for recurrent gliomas. In this study, we assessed the efficacy of OKN-007 in two adult (rat F98 and mouse GL261) and one novel pediatric (IC-3752GBM in nude mice) high grade glioma model. OKN-007 significantly reduced the percent necrosis (p<0.01) and tumor cell proliferation (p<0.05) in treated F98-tumor bearing rats compared to the untreated group. Based on molecular magnetic resonance imaging (MRI) results, OKN-007 was also found to significantly decrease (p<0.05) free radicals levels in treated F98 rats compared to the untreated group. We also assessed VEGFR-2 (vascular endothelial growth factor receptor 2) levels in untreated and OKN-007-treated GL261 mouse gliomas using molecular MRI. OKN-007 decreased significantly the levels of VEGFR-2 (p<0.05) in GL261 gliomas compared to the untreated group. Furthermore, OKN-007 was also able to decrease significantly the tumor volumes (p<0.01) and increase survival (p< 0.001) in GL261 treated mice. For the pediatric glioma study, MRI results showed that OKN-007 significantly decreased tumor volumes (p<0.05), increased diffusion (p<0.01) and perfusion rates (p<0.05) in a responsive cohort of IC-3752GBM treated animals. In addition, OKN-007 significantly increased animal survival (p<0.05), decreased tumor cell proliferation (p<0.05) and microvessel density (p<0.05) in responsive IC-3752GBM treated mice. Furthermore, the nitrone was also able to significantly decrease the immunoexpression of SULF2 (p<0.05) and PDGFRα (platelet-derived growth factor receptor-α) (p<0.05), and significantly increase the expression of decorin (p<0.05) in responsive IC-3752GBM pGBM tumor bearing mice. Taken together, our findings showed that OKN-007 mediated multiple effects in different rodent glioma models, indicating that the efficacy associated with OKN-007 is a result of anti-proliferative, free radical scavenging, and anti-angiogenic properties. Furthermore, OKN-007 might be also an effective anti-cancer agent for some patients with pediatric gliomas, possibly by inhibiting the PDGFRα pathway, and could be considered as an additional therapy for pediatric brain tumor patients.

TABLE OF CONTENTS

Chapter Page

Chapter Page

LIST OF FIGURES

Figure Page

CHAPTER I

OKN-007 decreases tumor necrosis and tumor cell proliferation and increases apoptosis in a pre-clinical F98 rat glioma model

1.1 INTRODUCTION

Gliomas are primary brain tumors that represent 30% of all central nervous system tumors and 80% of all malignant brain tumors [1-3]. Gliomas are classified into low grade (World Health Organization (WHO) grades I–II) and high grade (WHO grades III–IV) based on five main features: cytological atypia, anaplasia, mitotic activity, microvascular proliferation, and necrosis [4]. Glioblastoma (GBM) is categorized as a grade IV glioma, and it is the most common malignant and most aggressive type of primary brain tumor in adults [5]. Most patients diagnosed with this tumor die within one year from the diagnosis, and only 5% survive more than 5 years despite aggressive therapies [1]. Advances in genetics and molecular biology of the tumor and tumor microenvironment have led to the development of novel therapies for GBMs; however, better therapeutic options are still needed to cure patients diagnosed with GBM or to dramatically improve survival times.

The roles of different nitrones, such as the nitrone compound OKN-007 (Oklahoma Nitrone-007; disodium 4-[(tert-butyl-imino) methyl] benzene-1,3-disulfonate N-oxide or disufenton), as anticancer agents and their possible mechanisms of action in gliomas have been studied in detail [6]. OKN-007 is a small molecule that can traverse the blood–brain barrier and has anti-inflammatory, antioxidant, and proapoptotic properties [6]. Our group has established that OKN-007 is an effective anti-cancer agent in rodent pre-clinical models for adult GBMs [7-9], and it is currently undergoing clinical trial assessment as a new investigational drug in recurrent GBMs. In an orthotopic rat F98 glioma model and a human U87 xenograft model in athymic rats, OKN-007 was found to significantly increase the survival of treated versus untreated rats. Morphological magnetic resonance imaging (MRI) showed that tumor volumes in both of these models were significantly decreased in treated compared with untreated animals [8]. Despite these findings, the mechanism(s) of action of OKN-007 are not fully understood, and our research aims at identifying how OKN-007 mediates effects, such as necrosis and cell proliferation, on various tumor regions.

MRI is routinely used for the diagnosis, treatment planning, and assessment of response to therapy for patients with gliomas [9-21]. Proton magnetic resonance spectroscopy (^{1}H-MRS), which has been used in research and clinical settings to measure metabolite levels in the brain, and diffusion-weighted imaging (DWI), which is used to characterize tumor growth and vasculature by measuring microscopic translational motion of water molecules within tissues, have been shown to be among the most valuable techniques that can provide a more complete evaluation of functional, cellular, and metabolic information about human GBMs [22].

Here, we report the effects of OKN-007 within the necrotic tumor core and non-necrotic tumor parenchyma in a F98 rat glioma model assessed by DWI and supported by ^{1}H-MRS. The F98 rat glioma model was chosen as a suitable experimental model for this study because it has a characteristic infiltrative pattern of growth that resembles human GBM and is classified as an anaplastic malignant tumor. Supporting histological data for necrosis, immunohistochemistry for cell proliferation and apoptosis, and microarray data analysis are also presented.

1.2 METHODS

1.2.1 Glioma implantation

The animal studies were conducted with approval from the Institutional Animal Care and Use Committees of the Oklahoma Medical Research Foundation and the University of Utah Health Sciences Center. The F98 rat glioma cell implantation model was prepared as described previously [8]. F98 cells (10^5 in 10-µl volume) were intracerebrally implanted with a stereotaxic device (2 mm lateral and 2 mm anterior to the bregma at a 3-mm depth) in 24 Fischer 344 rats (male 200–250 gm). The animals were divided into two groups: OKN-007–treated (n = 12) and untreated (n = 12) groups. Both groups were stratified to ensure that tumor sizes were similar before initiation of treatment.

1.2.2 OKN-007 treatment

OKN-007 (Ryss Laboratories, Union City, CA) was administered to the rats in their drinking water at a concentration of 0.018% w/v. The treatment started at 15 days after glioma cell implantation, when the tumor volumes were between 10 and 15 mm^3, and was administered continuously until the end of the study. Rats receiving normal drinking water were used as untreated controls. The amount of OKN-007 consumed by each rat, which were housed in separate cages, was determined by weighing water bottles each day. No significant deviation was observed in the volume of liquid uptake of compound in these rats. The average intake of OKN-007 was ~10 mg/kg/day.

1.2.3 MR Imaging

1.2.3.1 ^{1}H-MR Spectroscopy

^{1}H-MRS values were obtained in untreated (n = 7) and OKN-007–treated (n = 8) animals bearing F98 gliomas as well as a group of 6 normal Fischer 344 rats. All MR imaging experiments were conducted on a Bruker Biospec 7.0 T (Bruker Biospin, Germany) using a 72-mm quadrature volume coil for signal transmission and a rat head surface coil for signal reception. Tumor morphology was observed on T2-weighted (T2W) images obtained with the application of the spin echo pulse sequence, rapid acquisition with relaxation enhancement (RARE) using a TR (repetition time) = 5000 ms, TE (echo time) = 63 ms, 20 transverse 1 mm-thick slices, and a field of view of 3.5 × 3.5 cm^2 with an in-plane resolution of 137 × 137 μm^2.

^{1}H-MRS was acquired using a stimulated-echo acquisition mode (STEAM) sequence with a TE of 4.4 ms, a TM (mixing time) of 10 ms, a TR of 3000 ms, 256 averages, and a spectral width of 4006 Hz. A nonsuppressed MR spectrum was acquired beforehand by applying eddy-current correction to maximize signal intensity and decrease the peak linewidth. Water was suppressed with a variable power radio frequency pulses and optimized relaxation delays (VAPOR) suppression scheme. For all cases, the peak width (full width at half maximum) of the water peak was less than 30 Hz following localized shimming, which was conducted by using first- and second-order adjustments in Fastmap. A cubic voxel with sides of 3.0 mm was positioned in either the tumor or the contralateral normal brain tissue, while maximizing the amount of tumor tissue present in the voxel at all times.

To analyze the MRS data, we used a Mathematica (version 6.0, Wolfram Research, Champaign, IL) notebook written by our group. The spectra were then scaled in ppm by calibrating on the water peak (4.78 ppm). The major brain metabolic peaks were identified as N-acetylaspartate (NAA) at 2.02 ppm, choline and choline-containing compounds (total Cho) at 3.22 ppm, creatine (Cr) and phosphocreatine (referred to as total Cr) at 3.02 ppm, and mobile lipids (absent in the normal brain tissue), which appeared sharply at 1.3 ppm for the methylene group, 0.9 ppm for the methyl group, and 5.3 ppm for the vinyl protons on unsaturated fatty acyl groups, in tumor tissue. The quantification of variations in metabolite levels were evaluated as peak length ratios: Cho/Cr, NAA/Cr, Lip5.3 (vinyl)/Cr, Lip1.3 (methylene)/Cr, and Lip0.9 (methyl)/Cr.

1.2.3.1 DWI

A coronal and axial multi-slice DWI sequence covering the entire tumor was performed using echo planar imaging–based pulse sequence with the following parameters: TR/TE = 3750/51.1 ms, matrix size = 28 × 128, diffusion gradient duration = 4 ms, diffusion gradient separation = 14 ms, and five b values ranging from 200 to 3000 s/mm^2. Apparent diffusion coefficient (ADC) maps were generated for all the slices in which the tumor was observed. Uniform circular regions of interest (ROIs) (0.1 cm^2) were drawn in the tumor parenchyma and tumor necrotic core in each slice of each animal from each group. The ADC of each ROI was recorded and the mean ADC value and standard deviation (x10^{-3} mm^2/s) were obtained for each region of the tumor. The numbers of ROIs for the tumor parenchyma in the untreated group (n = 12) and OKN-007–treated (n = 12) groups were >1600. The numbers of ROIs for the tumor necrotic core in the untreated group and OKN-007–treated groups were >500.

1.2.4 Quantification of tumor necrosis

Whole brains of one rat from the untreated group and one rat from the OKN-007–treated group were removed, preserved in 10% neutral buffered formalin, and processed under routine conditions. The paraffin-embedded brain tissues were completely sectioned in 4-μm slices in the axial plane to correspond to the plane of the MR images. Each tissue section was mounted on frosted glass slides and stained with hematoxylin and eosin (H&E). All histological slides from both animals were digitized using the Aperio ScanScope Image Analysis System (Aperio, Vista, CA) at the University of Oklahoma Health Sciences Center. Necrosis and whole tumor areas were measured in each histological slide using the Aperio ImageScope software. Percent tumor necrosis was calculated with the following formula: (total necrotic tumor area/total tumor area) × 100.

Percent tumor necrosis in untreated ($n = 10$) and OKN-007 ($n = 8$) treated animals was also calculated from T2W images. Tumor and necrotic volumes (mm^3) were measured by drawing freehand ROIs to measure their areas and multiplied by the slice thickness and number of slices where the tumor and necrotic tumor core were observed. Percent tumor necrosis was calculated with the following formula: (total necrotic tumor volume/total tumor volume) × 100.

1.2.5 Quantification of tumor cellularity

Tumor cellularity was calculated in one representative H&E-stained slide for animals from each group (untreated and OKN-007–treated) using the Aperio ScanScope Image Analysis System. The number of tumor cells was counted in three 1-mm^2 ROIs for each H&E-stained slide from each animal. Areas adjacent to or within necrotic or inflammatory regions were excluded while counting the tumor cellularity. The mean and standard deviation of the number of cells per mm^2 were determined for each group.

1.2.6 Immunohistochemistry

To characterize tumor cell proliferation and apoptosis in both untreated and OKN-007–treated groups, immunohistochemistry for Ki-67 antibody (1:100 dilution, rabbit polyclonal, clone PA5-19462, Thermo Fisher Scientific, IL) and active/cleaved Caspase 3 (1:200 dilution, rabbit polyclonal, clone NB600-1235, Novus Biologicals, CO) was performed using an automated immunostainer (Leica, Bond-III, Leica, Buffalo Grove, IL).

The Aperio ScanScope Image Analysis System was used to determine the KI-67 labeling index (Ki-67 LI) and apoptotic index (AI). The areas with the highest number of labeled nuclei were identified in each case. Ki-67 LI and AI were determined by counting 1000 cells and expressing this as the number of labeled cells per 1000 cells [23] for each animal from both untreated and OKN-007–treated groups. Labeled cells adjacent to or within necrotic areas were excluded while counting the Ki-67 LI and AI. The mean and standard deviation of Ki-67 LI and AI were determined for each group.

1.2.7 Microarray

RNA was isolated from the brain tissue and further purified using an RNeasy Mini Kit (Qiagen, Valencia, CA) and the RNA cleanup protocol provided. After purification, the RNA concentration was determined with a Nanodrop 2000c scanning spectrophotometer (Thermo Scientific, Wilmington, DE) and then qualitatively assessed for degradation using the ratio of 28:18s rRNA obtained from a capillary gel electrophoresis system (Agilent 2100 Bionalalyzer, Agilent Technologies, Santa Clara, CA).

The Illumina TotalPrep RNA Amplification Kit was used for labeling cRNA (Ambion, Austin, TX). Briefly, 200 ng of total RNA was primed with T7-oligo-dT and reverse transcribed; this was followed by production of double-stranded cDNA with *E coli* DNA polymerase. cRNA was transcribed *in vitro* from the T7 promoter using a biotinylated ribonucleotide analog. cRNA was hybridized to HumanRef-8 v2 Expression BeadChips as specified by Illumina (San Diego, CA). BeadChips were washed and stained according to the Illumina protocol and scanned with an Illumina BeadArray Reader.

Illumina BeadStudio software was used to quantitate the signal from BeadChips, and the MATLAB normalized values were imported into BRB ArrayTools (Biometric Research Branch, National Cancer Institute) where they were then log transformed. Genes that fell below the 50th percentile of gene variance were excluded from the results. We identified genes that were differentially expressed between any two classes by using a multivariate permutation test [24,25]. We used the multivariate permutation test to provide a median false discovery rate of 5% (90% confidence). The test statistics used were random variance t-statistics for each gene [26]. Genes that were differentially expressed (<5% false discovery rate) and had a ratio twofold or larger were used in further analyses.

Pathways were explored by placing the data of genes that only passed our significance/ratio threshold into Ingenuity Pathways Analysis (Ingenuity Systems, www.ingenuity.com).

1.2.8 Statistical analysis

Statistical analyses were performed using Graph Pad Prism 6 (GraphPad, San Diego, CA, USA). All p values < 0.05 were considered statistically significant. Peak area ratios [Cho/Cr, NAA/Cr, Lip1.3 (methylene)/Cr, Lip0.9 (methyl)/Cr, and Lip5.3 (vinyl protons)/Cr], ADC value, total percent necrosis, tumor cell density, Ki-67 LI, and AI were reported as the mean ± standard deviation. For statistical analysis, Student t-tests (independent-samples, two-tailed t-test) were used to assess the differences between means of the normal, untreated, and OKN-007–treated F98 glioma rats.

1.3 RESULTS

1.3.1 OKN-007 inhibited tumor necrosis in the F98 rat glioma model

^{1}H-MRS values were obtained in normal Fischer 344 rats (n = 6) and in untreated (n = 7) and OKN-007–treated (n = 8) rats bearing F98 gliomas. Figure 1.1 shows that the Lip5.3/Cr ($p < 0.0001$), Lip0.9/Cr ($p = 0.0012$), and Lip1.3/Cr ($p = 0.0015$) ratios were significantly lower in OKN-007–treated group than in the untreated F98 gliomas at the end phase of tumor progression.

A total of 24 (untreated, n = 12; OKN-treated, n = 12) rat F98 gliomas were subjected to DWI. ADC maps (Fig. 1.2A,B) were generated from the images and used to determine the ADC value of the necrotic tumor core in each animal from each group. ADC values at the necrotic tumor core of the OKN-007–treated group were significantly lower than in the untreated group ($p < 0.05$) (Fig. 1.2C).

Morphological TW2 images also were used to assess the percent necrosis tumor volume in both groups, which was significantly higher ($p < 0.01$) in the untreated group (20.08% ± 2.00, n = 10) than in the OKN-007–treated group (11.96% ± 1.80, n = 7) (Fig. 1.3).

The percentage of tumor necrosis compared with the total tumor area on H&E-stained tumor sections was higher in the untreated group (23.44%, n = 1) compared with the OKN-007–treated group (10.32%, n = 1) (Fig. 1.4).

Furthermore, a partial microarray pathway analysis of isolated RNA from untreated and OKN-007–treated F98 gliomas shows downregulation of genes associated with calcium-channel regulation due to OKN-007 (Fig. 1.5). The matrix Gla protein (MGP) and the microfibrillar-associated protein 4 (MFAP4), which are directly associated with calcium-channel regulation, were both down-regulated by OKN-007. Two other genes linked to calcium-channel regulation were down-regulated by OKN-007: fibronectin type III domain-containing 1 gene, which is associated with G-protein βγ, and ADAM metallopeptidase, which is associated with the tumor necrosis factor (TNF).

1.3.2 OKN-007 inhibited tumor cell proliferation in the F98 rat glioma model

The Cho/Cr ($p = 0.0004$) ratio obtained in ^{1}H-MRS data was significantly lower in the OKN-007–treated group compared with untreated F98 gliomas at the end phase of tumor progression (Fig. 1.1).

The OKN-007–treated group showed significantly higher ($p < 0.05$) ADC values for the non-necrotic tumor parenchyma in the treated group than for the untreated group (Fig. 1.2D).

The tumor cell density (number of tumor cells/mm^2) was evaluated on the H&E-stained tumor sections of both treatment groups. The OKN-007–treated group (7571 ± 251, n = 10) showed significantly lower ($p < 0.001$) cellularity compared with the untreated group (8442 ± 139, n = 10) (Fig. 1.6).

Tumor cell proliferation was also evaluated through the immunoexpression of the anti-Ki-67 antibody. The Ki-67 LI was significantly lower ($p < 0.05$) in the OKN-007–treated group (53.25 ± 5.72, n = 6) than in the untreated group (71.73 ± 5.31, n = 7) (Fig. 1.7A–C).

OKN-007 increased apoptosis in the F98 rat glioma model. The AI was significantly higher ($p < 0.01$) in the OKN-007–treated group (27.09 ± 2.25, n = 5) compared with the untreated group (11.69 ± 3.38, n = 7) (Fig. 1.7D–F).

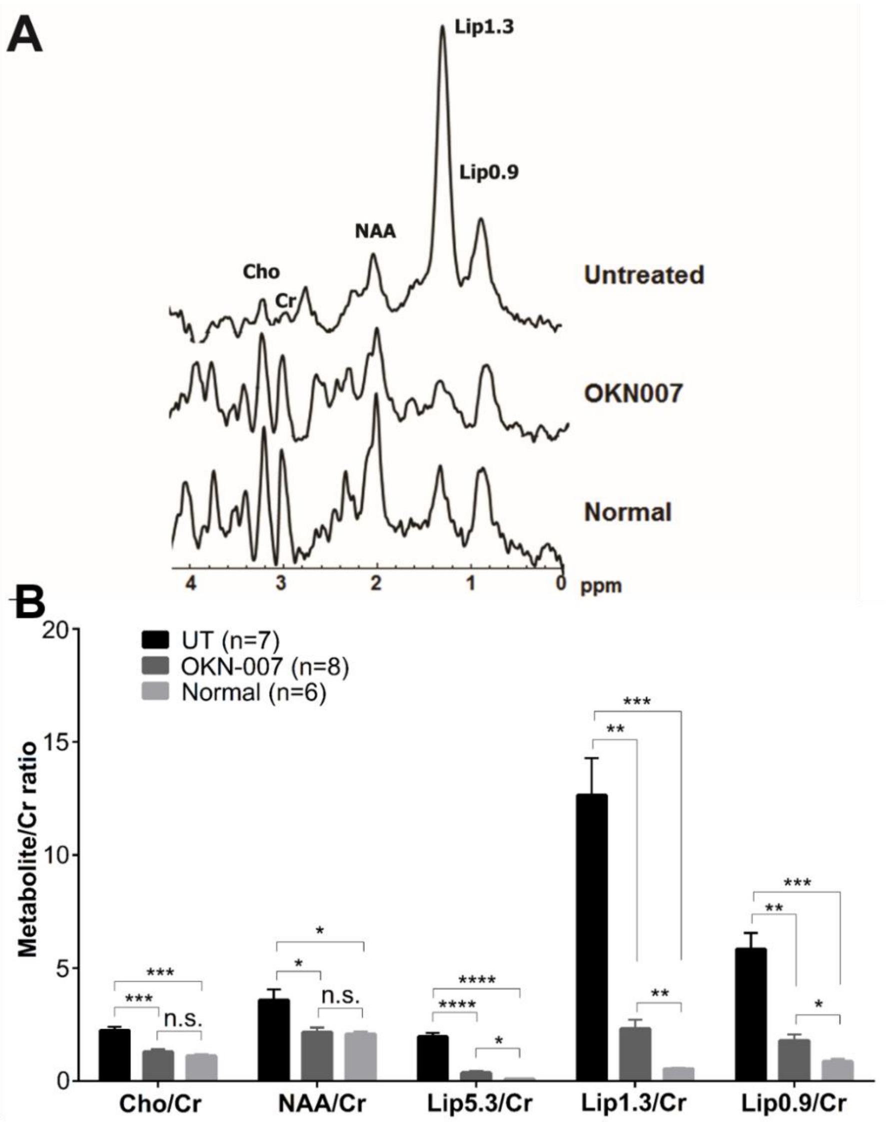

Figure 1.1. Effects of OKN-007 in a F98 glioma model assessed by ^{1}H MR spectroscopy. (A) Representative spectra from F98 gliomas depicting alterations in metabolite ratios from normal brain and OKN-007 treated and untreated (UT) glioma tissues. Spectra were obtained at the end-tumor time points. (B) Brain metabolite ratios measured by ^{1}H-MRSI in normal rat brain (n = 6) and UT (n = 7) and OKN-treated (n = 8) F98 rat gliomas. The UT group showed significantly higher Cho/Cr ($p<0.0001$), NAA/Cr ($p=0.0226$), Lip5.3 ($p<0.0001$), Lip1.3 ($p=0.0007$), and Lip0.9 ($p=0.0008$) compared to the normal rat brain. The Cho/Cr ($p=0.0004$), NAA/Cr ($p=0.0279$), Lip5.3/Cr ($p<0.0001$), Lip0.9/Cr ($p=0.0012$), and Lip1.3/Cr ($p=0.0015$) ratios significantly decreased in OKN-007 treated group compared to UT F98 gliomas at the end phase of tumor progression. The OKN-007 treated group demonstrated significantly higher Lip5.3/Cr ($p=0.0132$), Lip1.3/Cr ($p=0.0030$), and Lip0.9/Cr ($p=0.0114$) ratios compared to the normal rat brain. There was no significant difference between the Cho/Cr ($p=0.2436$) and NAA/Cr ($p=0.7281$) ratios from the OKN-007 treated group and normal rat brain. Values are represented as means ± SD. Asterisks indicate statistically significant difference (*$p < 0.05$, **$p < 0.01$, ***$p < 0.001$, ****$p < 0.0001$). n.s.: not statistically significant. Cho: choline, Cre: creatine, Lip5.3: vinyl, Lip1.3: methylene, Lip0.9: methyl.

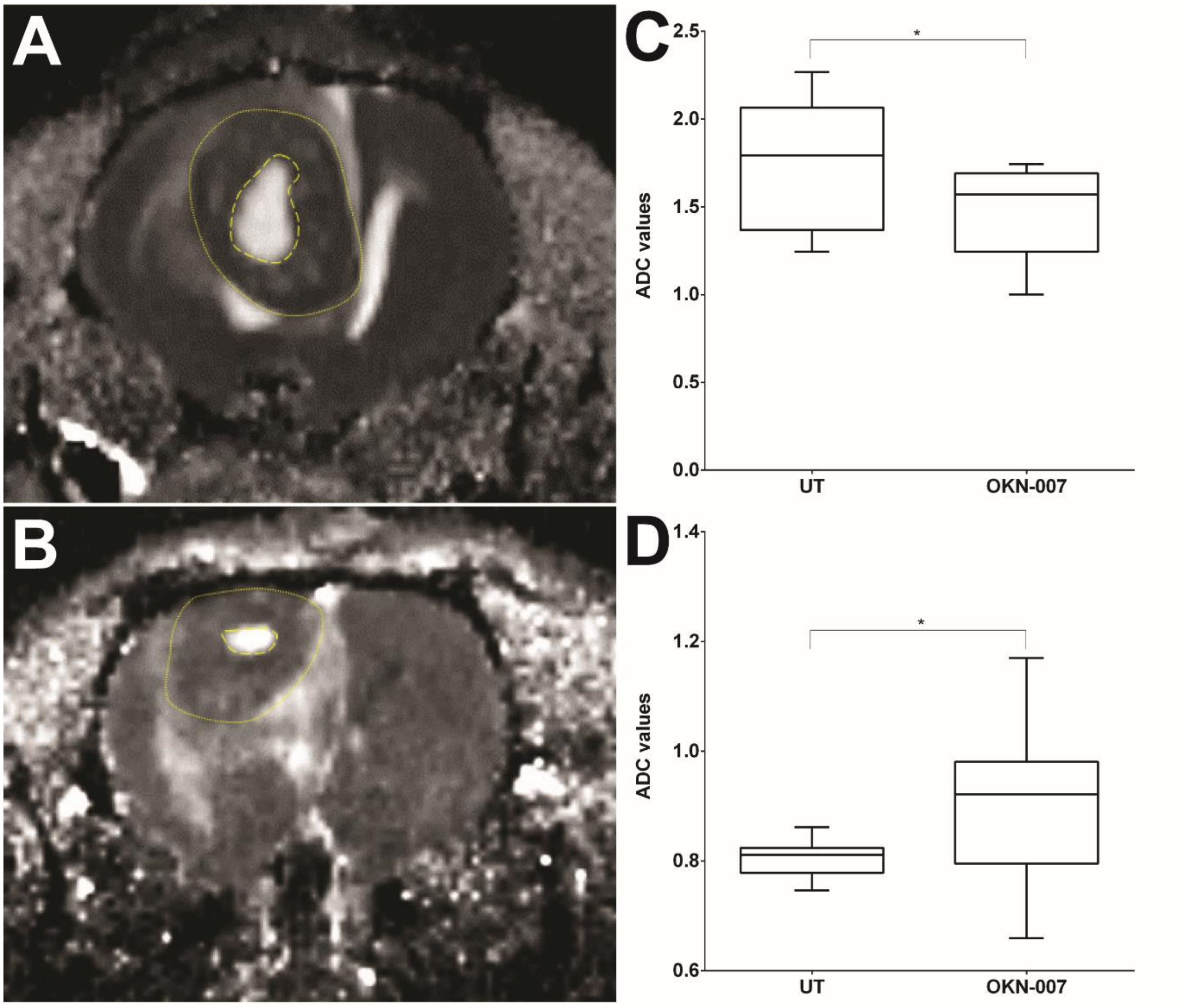

Figure 1.2. Regional changes in apparent diffusion coefficients (ADCs) after OKN-007 treatment of F98 gliomas. Representative ADC map for untreated (UT) (A) and OKN-007–treated (B) F98 rat gliomas. Dashed line indicates the necrotic core (hyperintense region in tumor interior) and solid line indicates the non-necrotic tumor parenchyma (hypointense region surrounding hyperintense necrotic core). (C) The ADC values at the necrotic core of the OKN-treated (1.474±0.080 $\times10^{-3}$ mm/sec^{2}, n=12, >500 ROIs) group were significantly lower than in the UT group (1.77±0.11 $\times10^{-3}$ mm/sec^{2}, n=12, 529 ROIs). (D) The ADC values at the non-necrotic tumor parenchyma of the OKN-treated (0.910±0.041 $\times10^{-3}$ mm/sec^{2}, n=12, >1600 ROIs) group was significantly higher compared with the UT group (0.807±0.010 $\times10^{-3}$ mm/sec^{2}, n=12, >1600 ROIs). In the box and whisker plots in C and D, the box extends from the 25th to the 75th percentile of ADC values, the line within the box is the median ADC value, and error bars are the minimum and maximum ADC values. Asterisks indicate statistically significant difference (*$p<0.05$).

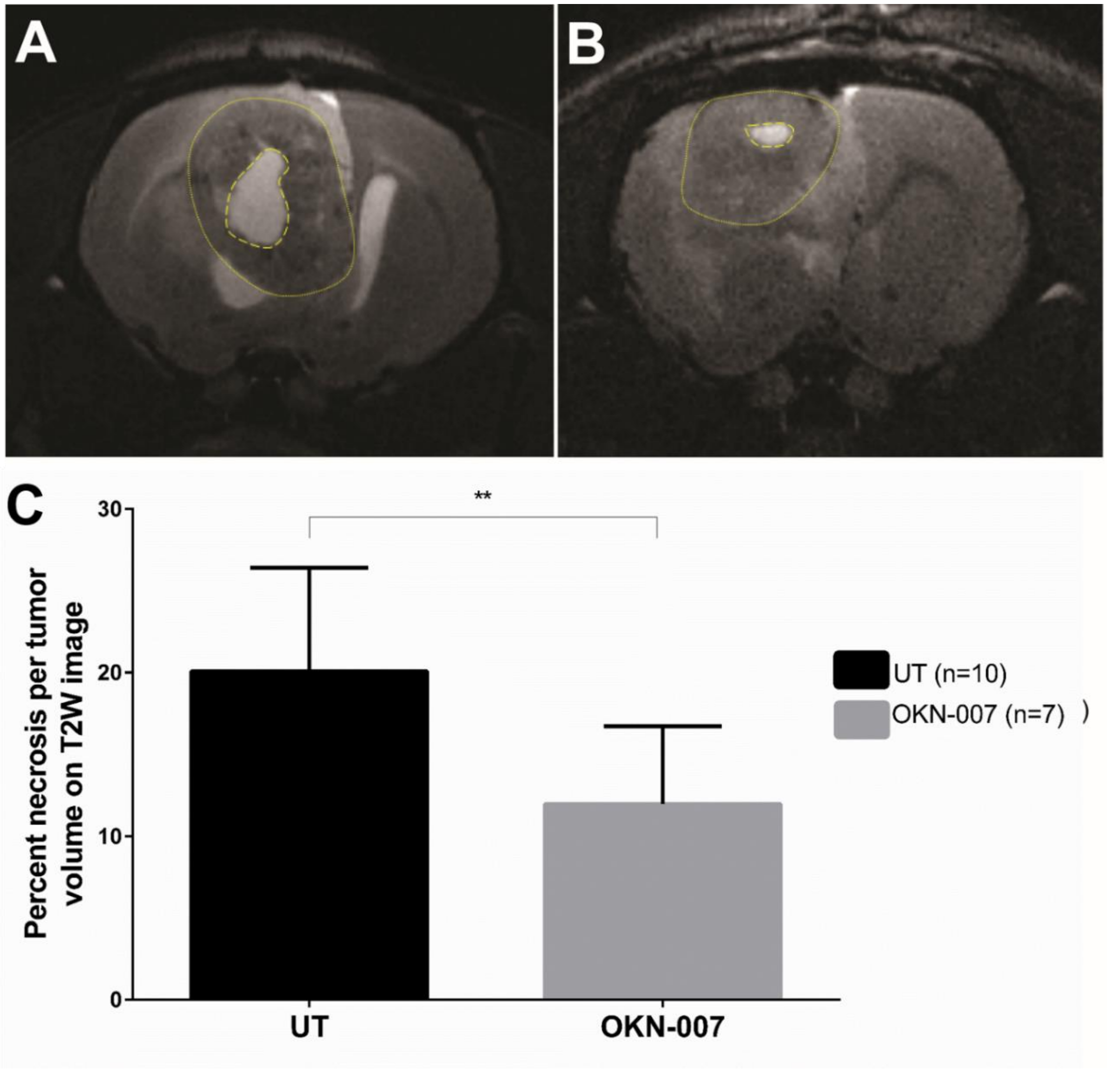

Figure 1.3. Representative T2W images for untreated (UT) (A) and OKN-007–treated (B) F98 rat gliomas. Dashed line indicates the necrotic core (hyperintense region in tumor interior) and solid line indicates the non-necrotic tumor parenchyma (hypointense region surrounding hyperintense necrotic core). (C) The percent necrosis tumor volume was significantly higher in the UT group (20.08±2.00, n=10) compared with the OKN-007 treated group (11.96±1.80, n=7) as measured on T2W images. Values are represented as means±SD. Asterisks indicate statistically significant difference (**p<0.01).

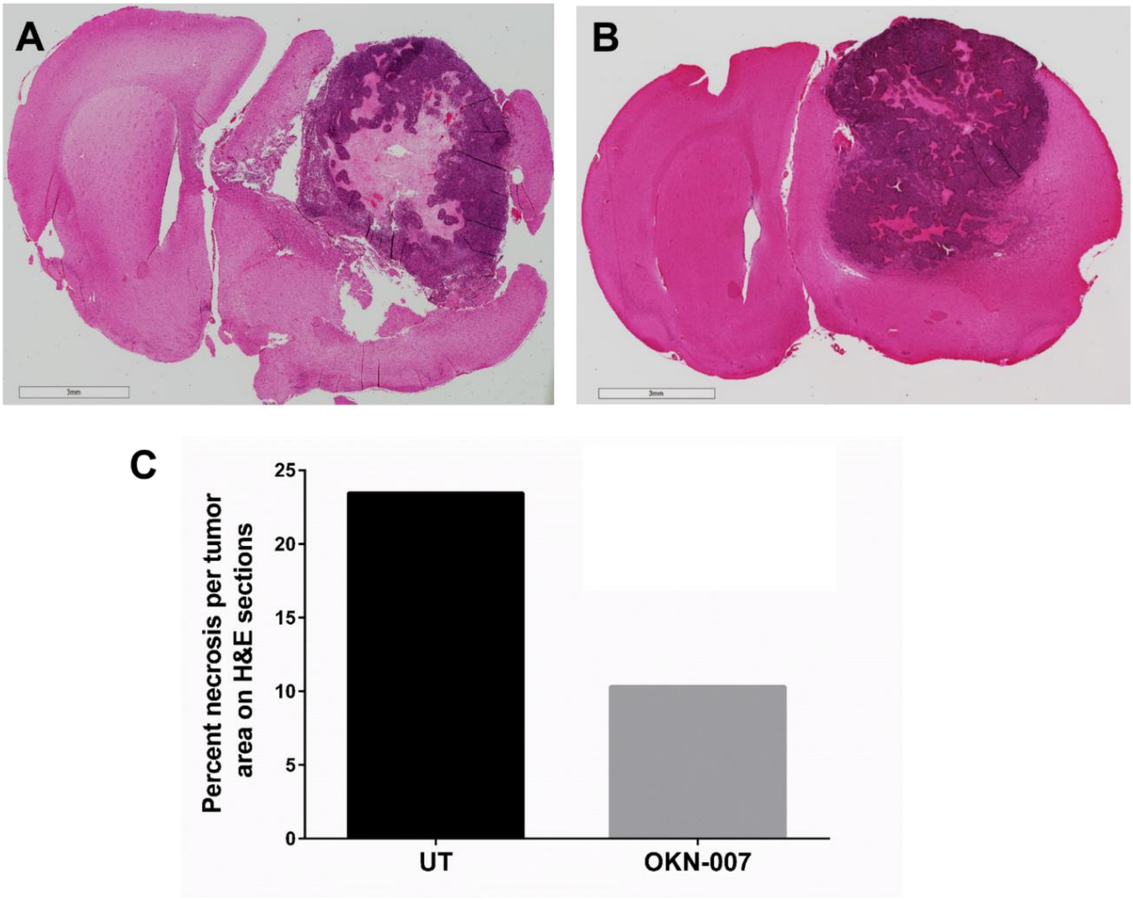

Figure 1.4. Representative histological (H&E) images from an untreated (UT) F98 glioma (A) and an OKN-007–treated F98 rat glioma (B). (C) The percent necrosis tumor volume as measured on H&E sections was higher in the UT group (23.44, n=1) than in the OKN-007–treated group (10.32, n=1). Values are represented as means±SD. Slides in A and B were digitized using Aperio ScanScope Image Analysis System (Aperio, Vista, CA).

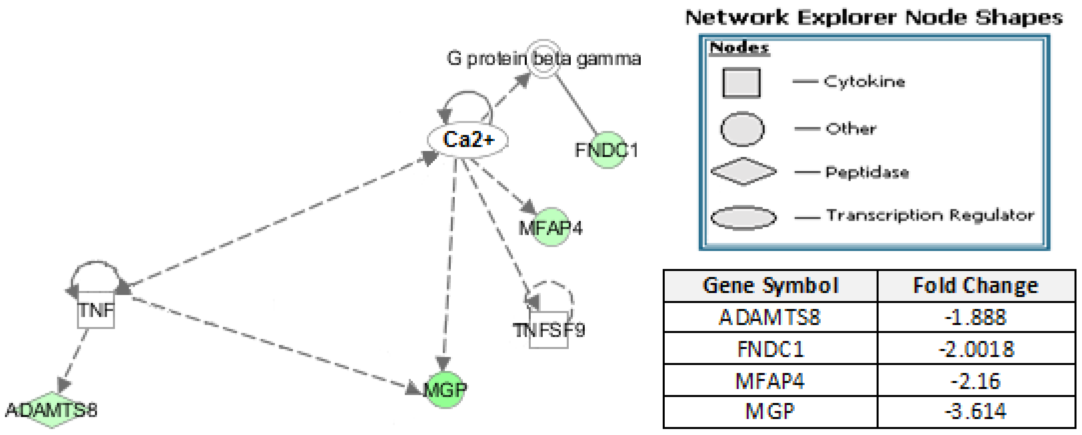

Gene Symbol	Fold Change
ADAMTS8	-1.888
FNDC1	-2.0018
MFAP4	-2.16
MGP	-3.614

Figure 1.5. Microarray assessment of the effect of OKN-007 on calcium (Ca^{2+}) channel regulation. Pathway analysis of isolated RNA from F98 gliomas that were untreated (n=5) compared with those that were OKN-007–treated (n=5) revealed down-regulation (depicted by a green color) in genes associated with calcium-channel regulation with a twofold difference and 5% false discovery rate. ADAMTS8: ADAM metallopeptidase with thrombospondin type 1 motif, 8; FNDC1: fibronectin type III domain containing 1; MFAP4: microfibrillar-associated protein 4; MGP: matrix Gla protein; TNF: tumor necrosis factor; TNFSF9: tumor necrosis factor superfamily, member 9.

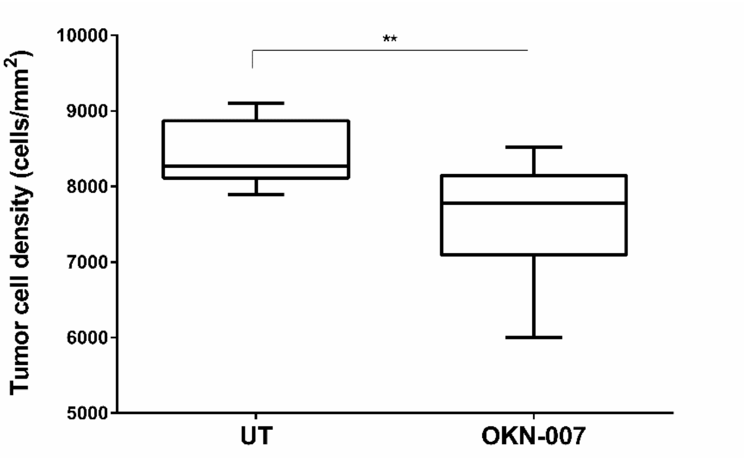

Figure 1.6. The tumor cell density (number of tumor cells/mm^2) obtained from histological sections was higher in the untreated (UT) group (8442±139, n=10) than in the OKN-007–treated group (7571±251, n=10). In this box and whisker plot, the box extends from the 25th to 75th percentiles of tumor cell density, the line within the box is the median tumor cell density, and error bars are the minimum and maximum values. Asterisks indicate statistically significant difference (** $p<0.01$).

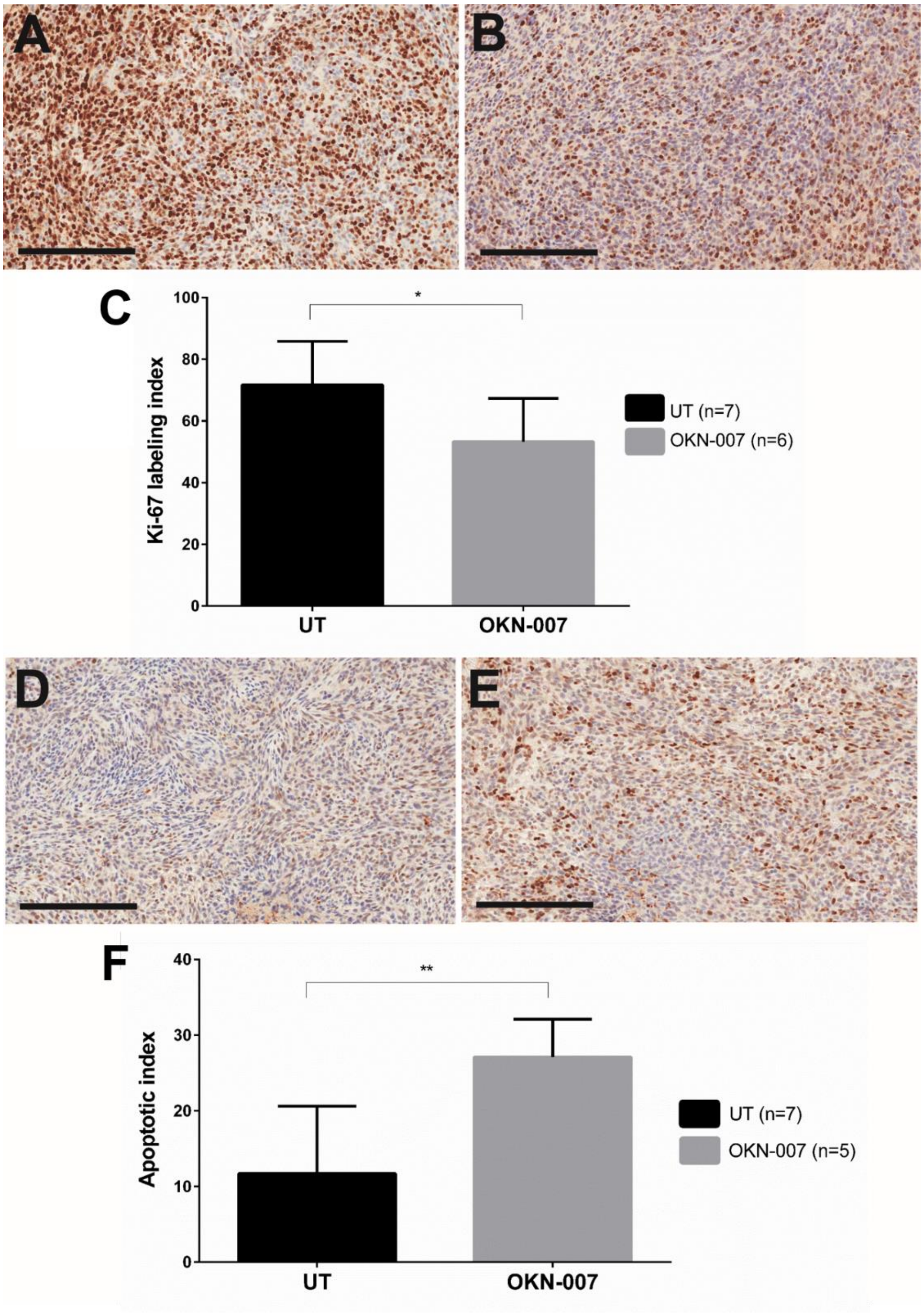

Figure 1.7. Immunohistochemical nuclear staining of Ki-67 in an untreated (UT) (A) (×200) and OKN-007–treated (B) F98 rat glioma (×200). (C) The Ki-67 labeling index was significantly lower in the OKN-007–treated group (53.25±5.72, n=6) compared with the UT group (71.73±5.31, n=7). Immunohistochemical nuclear staining of cleaved caspase-3 in an UT (D) (×200) and OKN-007–treated (E) F98 rat glioma (×200). (F) The apoptotic index was significantly higher in the OKN-007 treated group (27.09±2.24, n=5) compared with the UT group (11.69±3.37, n=7). Asterisks indicate statistically significant difference (*p<0.05, **p<0.01). Scale bars=200 µm.

1.4 DISCUSSION

The anti-cancer response to OKN-007 in F98 gliomas was previously reported by our group based on morphological (T2W) imaging, bioluminescence imaging, and immunohistochemistry assessments, in addition to survival data [8]. OKN-007 significantly decreased tumor volumes ($p < 0.05$), as measured by MRI, and increased survival ($p < 0.001$) in F98 glioma-bearing rats [8]. Assessment of treatment response using other MR parameters, such as ^{1}H-MRS, DWI, and perfusion rates, was also performed by our group in C6 glioma models [7,27], but the use of a multi-parametric approach has not been previously reported for the rat F98 glioma model.

^{1}H-MRS is a very useful method to obtain information on various tumor metabolites and to also assess treatment response. The principal metabolites that can be assessed by ^{1}H-MRS in brain tumors include Cho (3.2 ppm), Cr (3.0 ppm), NAA (2.0 ppm), and lipids (Lip; 0.9–1.3 ppm) [28]. Cho is involved in the synthesis and degradation of cell membranes, levels of which may increase in conditions of cell proliferation, inflammation, or demyelination. Furthermore, a linear correlation has been demonstrated between Cho and the cell proliferation index for Ki-67 positive cells [29-31]. Cr, consisting of creatine and phosphocreatine, is a marker for brain energy metabolism, which involves the production of extra energy when normal cellular energy production does not meet the needed energy demand. NAA, which is generated by neurons, diffuses along axons and is degraded in oligodendrocytes [32-34]. As a normal neuronal marker, NAA is reduced during any neuronal or axonal damage or loss. Membrane lipids are usually non-detectable by ^{1}H MRS, because of their decreased mobility and strong dipolar couplings; however, in pathological conditions, the release of fatty acids from membranes and/or lipid droplets increases the concentration of free lipids that appears as sharp peaks at 1.3 ppm (methylene group, CH_2) and 0.9 ppm (methyl group, CH_3) [34]. These lipid signals originate from fatty acyl chains of triacylglycerides that form mobile lipid droplets in the cytoplasm of intact cancer cells [35,36] or in the necrotic core of tumors [37-40]. Additionally, mobile polyunsaturated fatty acyl chain signals can be detected at 5.3–5.4 and 2.8 ppm and can be used to assess polyunsaturation of mobile lipids [36,41-43]. Intratumoral lipid droplets have been shown to correlate with drug resistance or therapy response [35]. Cytoplasmic accumulation of triacylglycerides in cancer cells and tumors has been attributed to diverse biological processes such as hypoxia, degeneration of mitochondria, differentiation, growth arrest [35,36], and apoptotic [44,45] and necrotic cell death [39,46-48].

Another useful magnetic resonance technique to assess tumor heterogeneity is DWI. DWI is routinely used to measure microscopic, random translational motion of water molecules within tissues. Any alterations in the tissue structure that disrupt the barriers of water diffusion, such as the breakdown of cell membranes or damage to fibers, would lead to changes in the diffusion properties within these regions. These diffusion characteristics can be quantified by estimating the ADC. DWI has been shown to be a very effective modality to characterize tumor growth and vasculature [7,49]. In tumors, ADC values can differentiate the cellular mechanisms involved in tumor development as well as responses to treatment such as cell proliferation, apoptosis, and/or necrosis [50]. Processes that degrade cellular integrity, such as necrosis caused by therapy or tumor growth, are thought to increase the ADC of tissue [51,52]. Conversely, since water molecules are more restricted in their movement within cells than in the extracellular space, high cell density is associated with a low ADC [53,54]. Studies have also shown the potential for ADC to be of diagnostic and prognostic value as a surrogate marker for assessment of therapeutic response in various cancers [54-64].

In this study, we attempted to understand the regional effect of OKN-007 in two different regions (the necrotic tumor core and the non-necrotic tumor parenchyma) in a F98 rat glioma model, considering the heterogeneous nature of the tumor and the multiple mechanisms of action effects mediated by OKN-007. We demonstrated that OKN-007 inhibited both tumor necrosis and cell proliferation in a F98 rat glioma model (Figure 1.8). The ^{1}H-MRS data showed a statistically significant decrease in the vinyl protons (5.3 ppm)/Cr, methylene (1.3 ppm)/Cr, and methyl (0.9 ppm)/Cr ratios for OKN-007–treated F98 rat gliomas compared with the untreated group (Fig. 1.1).

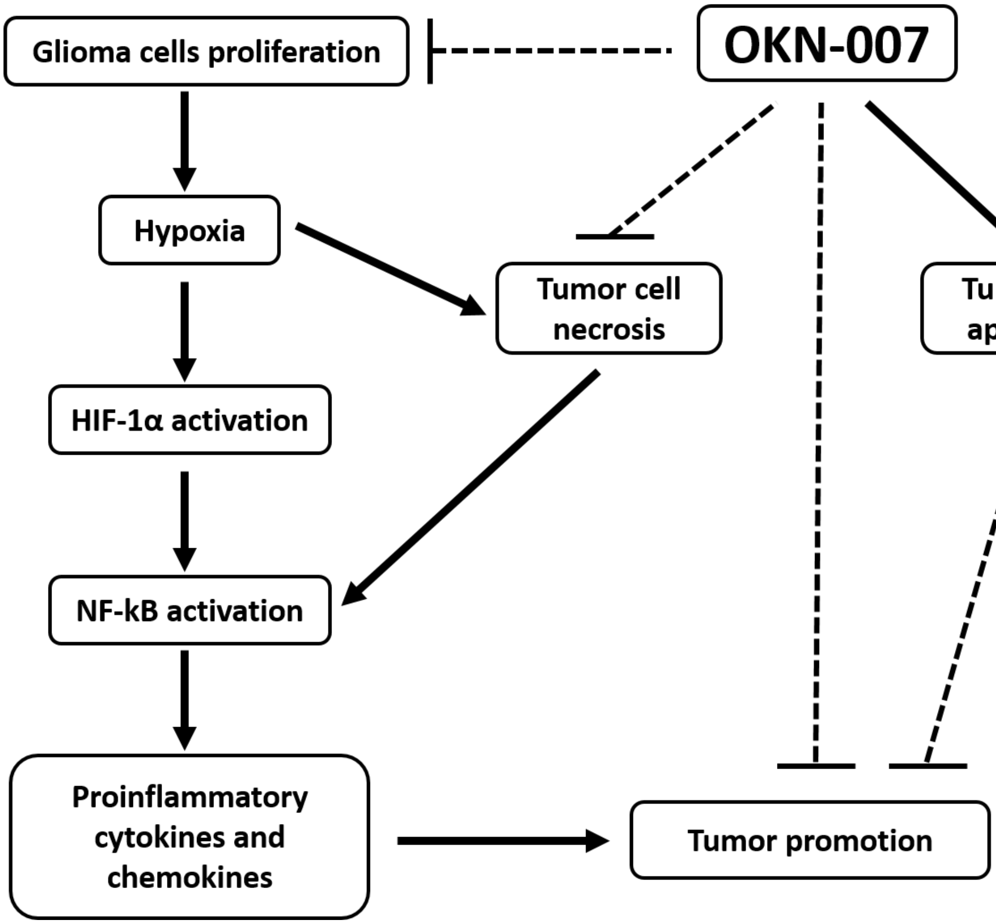

Figure 1.8. Schematic summary of the different mechanisms of action of OKN-007 therapy in a F98 rat glioma model. All solid malignancies, at some point outpace their blood supply and become oxygen and nutrient deprived. This results in necrotic cell death at the tumor's core and the release of pro-inflammatory mediators, leading to the tumor promotion. Tumor growth may also be stimulated in response to hypoxia-induced necrosis in the tumor's core. OKN-007 inhibits tumor necrosis and cell proliferation and promotes the tumor cell apoptosis in F98 rat gliomas based on the ^{1}H-MRSI, DWI, immunohistochemical, and microarray data analyses. HIF-1α: Hypoxia-inducible factor 1-alpha.

The role of mobile lipids in cancer has been the subject of many excellent reviews and articles [9,27,35,39,45,65-70]. In brain tumors, the elevation of the lipid levels usually correlates with necrosis [35,37,65,71], and lipids are considered as important biomarkers in the diagnosis and monitoring the effects of treatment response [65].

Necrosis is a hallmark of GBMs [4,72], with some studies suggesting it is present in over 85% of cases [73-76]. It is caused by tumor hypoxia as a result of increased cell proliferation and mitotic activity, as well as insufficient tissue perfusion [72,77]. The pathway of necrosis in glioblastoma begins with acute cellular ATP depletion as a result of electron transport chain collapse and subsequent decreased oxidative phosphorylation [78]. This lack of ATP leads to a failure in the ATP-dependent ion channels and pumps, which initiates a massive cell volume increase through Na^+ influx. The increased intracellular Na^+ concentration results in activation of the Na^+-K^+-ATPase, which further depletes cellular ATP stores [79]. This depletion leads to the opening of non-selective Ca^{2+} channels, resulting in elevated intracellular Ca^{2+} levels and activation of the Ca^{2+}-ATPase with eventual mitochondrial depolarization [79]. In addition, with severe ATP depletion, ionic homeostasis is no longer maintained by the K^+ efflux, leading to further Na^+ and water influxes that precipitate cellular swelling and collapse. As the cell membrane ruptures, the contents of the cells are released into the extracellular space, which will lead to the presence of high lipid peaks that are detected in ^{1}H-MRS.

A number of studies have also demonstrated that the increase in mobile lipids is associated with the onset of drug-induced apoptosis [47,65]. Interestingly, the OKN-007–treated F98 gliomas demonstrated significantly higher Lip5.3/Cr ($p = 0.0132$), Lip1.3/Cr ($p = 0.0030$), and Lip0.9/Cr ($p = 0.0114$) ratios compared with the normal rat brain, which might be due to an increase in apoptosis observed in the OKN-007–treated animals. In our study, the AI was significantly higher in the OKN-007–treated group (27.09 ± 2.24, n = 5) compared with the untreated group (11.69 ± 3.37, n = 7) (Fig. 1.7D-F).

These spectroscopic findings were also confirmed by DWI and histopathological data analyses. In our study, we effectively showed that ADC values at the necrotic tumor core of OKN-007–treated group were significantly lower than those in the untreated group ($p < 0.05$) (Fig. 1.2).

The inhibitory effect of OKN-007 in the necrotic tumor core of F98 gliomas was also noted based on the T2W images from each treatment group (Fig. 1.3). The percent necrosis tumor volume was significantly lower ($p < 0.01$) in the OKN-007–treated group (11.96% ± 1.80, n = 7) compared with the untreated group (20.08% ± 2.00, n = 10).

Necrosis volumes were also measured quantitatively from H&E-stained tumor sections, which is the gold-standard technique to evaluate tumor necrosis. The analysis was performed in H&E-staining sections of the whole tumor from one representative animal from each treatment group. OKN-007 also decreased the percentage of tumor necrosis compared with the total tumor area on H&E-stained tumor sections in a treated F98 glioma rat (10.32, n = 1, 1118 H&E sections) compared with an untreated animal (23.44, n = 1, 1215 H&E sections) (Fig. 1.4). The possible explanation for this observation could be that OKN-007 affects necrosis by down-regulating the genes associated with Ca^{2+} channels, thereby reducing the intracellular Ca^{2+} levels. The effect of OKN-007 on genes associated with Ca^{2+} channels was confirmed by our microarray results wherein OKN-007 was shown to down-regulate two genes, MGP and MFAP4, which are directly related to Ca^{2+} channels. MGP is down-regulated by a 3.16-fold change and MFAP4 is down-regulated by a 2.16-fold change as a result of OKN-007 treatment (Fig. 1.5). In addition, a few other genes associated with Ca^{2+} channels also seem to be down-regulated by OKN-007 as shown in Figure 1.5. Since TNFα is related to the genes associated with Ca^{2+} channels, down-regulation of Ca^{2+}-related genes could also lead to reduced expression of genes for TNFα, which in turn down-regulates the NF-κβ pathway, thereby causing a decrease in necrosis. There was also down-regulation of ADAMTS8, which is directly linked to TNF.

Furthermore, our study also demonstrated that OKN-007 inhibited tumor cell proliferation in the F98 rat glioma model. Previous studies have confirmed that the relative increase in choline in most high-grade gliomas is due to the increase in membrane synthesis and accelerated cell proliferation [80,81]. Total Cho, which resonates at 3.2 ppm, is a composite peak with contributions from choline, phosphocholine, and glycerophosphocholine. An increase in the total Cho resonance in tumors arises primarily from the synthesis and accumulation of phosphocholine, a metabolite produced by rapid uptake and phosphorylation of choline that is necessary for the downstream synthesis of phosphatidylcholine, a major membrane phospholipid constituting around 25% of mammalian cellular lipids [82,83]. Here, we demonstrated that OKN-007 significantly decreased the Cho/Cr ratio ($p = 0.0004$) at the end phase of tumor progression (Fig. 1.1B), because of a decrease in the tumor cell proliferation, which was also confirmed by our DWI and histopathological results.

Both intra- and extracellular spaces and their exchange contribute to the measured ADC. As cellular density increases, the added tortuosity to extracellular mobility paths reduces water mobility and, consequently, the ADC value [84]. Based on that observation, within a given tissue or cell type, ADC is useful as an indicator of the relative cellularity, such as in the evolution of tumor over time following therapy [85]. ADC is inversely proportional to cell density [86], and after an effective treatment the cellularity is reduced from apoptosis and necrosis, and the diffusivity increases [87]. A rise in ADC indicates a positive response to therapy. The observed increase in water ADC following therapy is directly related to the number of tumor cells killed and is thought to be due to the liberation of water into the extracellular space [85]. In our study, the ADC values in the non-necrotic tumor parenchyma of the OKN-treated group ($0.910 \pm 0.0041 \times 10^{-3}$ mm/sec^2, $n = 12$, >1600 ROIs) were significantly higher ($p < 0.05$) than in the untreated group ($0.807 \pm 0.010 \times 10^{-3}$ mm/sec^2, $n = 12$, >1600 ROIs) (Fig. 1.2D), reflecting less restricted diffusion consequent to a decrease in tumor cellularity in the OKN-007–treated F98 rat gliomas.

Tumor cell density (number of cells/mm^2) and cell proliferation were also evaluated using H&E-stained tumor sections and immunoexpression of the antibody anti-Ki-67, respectively. The OKN-007–treated group (7571 ± 251, $n = 10$) showed significantly lower cellularity ($p < 0.01$) compared with the untreated group (8442 ± 139, $n = 10$) (Fig. 1.6). Ki-67 LI was significantly lower ($p < 0.05$) in the OKN-007–treated group (53.25 ± 5.72, $n = 6$) compared with the untreated group (71.73 ± 5.31, $n = 7$) (Fig. 1.7A-C).

Finally, our results also corroborated the results from other studies [31] that confirmed the positive correlation of the glioma Cho signal with cell density and an inverse linear correlation between glioma cell density and ADC values.

1.5 CONCLUSION

Our results indicate that OKN-007 mediates multiple effects on different (tumor necrotic core and non-necrotic tumor parenchyma) regions of the tumor in F98 gliomas that can be detected *in vivo*, indicating the efficacy of OKN-007 as an anti-cancer agent and its clinical potential. Our ^{1}H-MRS, DWI, immunohistochemical, and microarray data analyses showed that OKN-007 reduced necrosis and tumor cell proliferation. There was also an increase in apoptosis after OKN-007 treatment that seemed to correlate with spectroscopic lipid alterations. Our results also indicated that both ADC and spectroscopic choline measures are related to glioma cell density in the F98 rat glioma model. This study further supports the use of OKN-007 as a potential anti-glioma agent.

1.6 REFERENCES

1. Central Brain Tumor Registry of the United States, CBTRUS statistical report: primary brain and central nervous system tumors diagnosed in the United States in 2004-2008, Hinsdale, IL, 2012.

2. Porter KR, McCarthy BJ, Freels S, Kim Y, Davis FG. Prevalence estimates for primary brain tumors in the United States by age, gender, behavior, and histology. Neuro Oncol. 2010;12:520-7.

3. Kelly PJ. Gliomas: Survival, origin and early detection. Surg Neurol Int. 2010;1:96.

4. Louis DN, Ohgaki H, Wiestler OD, Cavenee WK, Burger PC, Jouvet A, Scheithauer BW, Kleihues P. The 2007 WHO classification of tumours of the central nervous system. Acta Neuropathol. 2007;114:97-109.

5. Furnari FB, Fenton T, Bachoo RM, Mukasa A, Stommel JM, Stegh A, Hahn WC, Ligon KL, Louis DN, Brennan C, Chin L, DePinho RA, Cavenee WK. Malignant astrocytic glioma: genetics, biology, and paths to treatment. Genes Dev. 2007;21:2683-710.

6. Floyd RA, Chandru HK, He T, Towner R. Anti-cancer activity of nitrones and observations on mechanism of action. Anticancer Agents Med Chem. 2011;11:373-9.

7. Garteiser P, Doblas S, Watanabe Y, Saunders D, Hoyle J, Lerner M, He T, Floyd RA, Towner RA. Multiparametric assessment of the anti-glioma properties of OKN007 by magnetic resonance imaging. J Magn Reson Imaging. 2010;31:796-806.

8. Towner RA, Gillespie DL, Schwager A, Saunders DG, Smith N, Njoku CE, Krysiak RS 3rd, Larabee C, Iqbal H, Floyd RA, Bourne DW, Abdullah O, Hsu EW, Jensen RL. Regression of glioma tumor growth in F98 and U87 rat glioma models by the Nitrone OKN-007. Neuro Oncol. 2013;15:330-40.

9. He T, Doblas S, Saunders D, Casteel R, Lerner M, Ritchey JW, Snider T, Floyd RA, Towner RA. Effects of PBN and OKN007 in rodent glioma models assessed by 1H MR spectroscopy. Free Radic Biol Med. 2011;51:490-502.

10. Romano A, Calabria LF, Tavanti F, Minniti G, Rossi-Espagnet MC, Coppola V, Pugliese S, Guida D, Francione G, Colonnese C, Fantozzi LM, Bozzao A. Apparent diffusion coefficient obtained by magnetic resonance imaging as a prognostic marker in glioblastomas: correlation with MGMT promoter methylation status. Eur Radiol. 2013;23:513-20.

11. Catana C, Benner T, van der Kouwe A, Byars L, Hamm M, Chonde DB, Michel CJ, El Fakhri G, Schmand M, Sorensen AG. MRI-assisted PET motion correction for neurologic studies in an integrated MR-PET scanner. J Nucl Med. 2011;52:154-61.

12. Colonnese C, Romanelli P. Advanced neuroimaging techniques in the management of glioblastoma multiforme. Curr Radiopharm. 2012;5:300-7.

13. Hattingen E, Jurcoane A, Daneshvar K, Pilatus U, Mittelbronn M, Steinbach JP, Bähr O. Quantitative T2 mapping of recurrent glioblastoma under bevacizumab improves monitoring for non-enhancing tumor progression and predicts overall survival. Neuro Oncol. 2013;15:1395-404.

14. Park I, Larson PE, Zierhut ML, Hu S, Bok R, Ozawa T, Kurhanewicz J, Vigneron DB, Vandenberg SR, James CD, Nelson SJ. Hyperpolarized 13C magnetic resonance metabolic imaging: application to brain tumors. Neuro Oncol. 2010;12:133-44.

15. Artzi M, Blumenthal DT, Bokstein F, Nadav G, Liberman G, Aizenstein O, Ben Bashat D. Classification of tumor area using combined DCE and DSC MRI in patients with glioblastoma. J Neurooncol. 2015;121:349-57.

16. Kickingereder P, Wiestler B, Graf M, Heiland S, Schlemmer HP, Wick W, Wick A, Bendszus M, Radbruch A. Evaluation of dynamic contrast-enhanced MRI derived microvascular permeability in recurrent glioblastoma treated with bevacizumab. J Neurooncol. 2015;121:373-80.

17. Barajas RF Jr, Phillips JJ, Parvataneni R, Molinaro A, Essock-Burns E, Bourne G, Parsa AT, Aghi MK, McDermott MW, Berger MS, Cha S, Chang SM, Nelson SJ. Regional variation in histopathologic features of tumor specimens from treatment-naive glioblastoma correlates with anatomic and physiologic MR Imaging. Neuro Oncol. 2012;14:942-54.

18. Chawla S, Zhang Y, Wang S, Chaudhary S, Chou C, O'Rourke DM, Vossough A, Melhem ER, Poptani H. Proton magnetic resonance spectroscopy in differentiating glioblastomas from primary cerebral lymphomas and brain metastases. J Comput Assist Tomogr. 2010;34:836-41.

19. Lescher S, Jurcoane A, Veit A, Bähr O, Deichmann R, Hattingen E. Quantitative T1 and T2 mapping in recurrent glioblastomas under bevacizumab: earlier detection of tumor progression compared to conventional MRI. Neuroradiology. 2015;57:11-20.

20. Yun TJ, Park CK, Kim TM, Lee SH, Kim JH, Sohn CH, Park SH, Kim IH, Choi SH. Glioblastoma Treated with Concurrent Radiation Therapy and Temozolomide Chemotherapy: Differentiation of True Progression from Pseudoprogression with Quantitative Dynamic Contrast-enhanced MR Imaging. Radiology. 2014;21:132632.

21. Li X, Jin H, Lu Y, Oh J, Chang S, Nelson SJ. Identification of MRI and 1H MRSI parameters that may predict survival for patients with malignant gliomas. NMR Biomed. 2004;17:10-20.

22. Khayal IS, Crawford FW, Saraswathy S, Lamborn KR, Chang SM, Cha S, McKnight TR, Nelson SJ. Relationship between choline and apparent diffusion coefficient in patients with gliomas. J Magn Reson Imaging. 2008;27:718-25.

23. Ralte AM, Sharma MC, Karak AK, Mehta VS, Sarkar C. Clinicopathological features, MIB-1 labeling index and apoptotic index in recurrent astrocytic tumors. Pathol Oncol Res. 2001;7:267-78.

24. Simon R, Korn E, McShane L, Radmacher M, Wright W, Zhao Y. Design and Analysis of DNA Microarray Investigations, Springer Verlag, New York, 2003.

25. Korn E, Troendle J, McShane L, Simon R. Controlling the number of false discoveries: Application to high-dimensional genomic data, J. Stat. Plan. Inference. 2004, 124: 379-398.

26. Wright GW, Simon RM. A random variance model for detection of differential gene expression in small microarray experiments. Bioinformatics. 2003;19:2448-55.

27. Doblas S, He T, Saunders D, Hoyle J, Smith N, Pye Q, Lerner M, Jensen RL, Towner RA. In vivo characterization of several rodent glioma models by 1H MRS. NMR Biomed. 2012;25:685-94.

28. Bertholdo D, Watcharakorn A, Castillo M. Brain proton magnetic resonance spectroscopy: introduction and overview. Neuroimaging Clin N Am. 2013;23:359-80.

29. Barbarella G, Ricci R, Pirini G, Tugnoli V, Tosi MR, Bertoluzza A, Calbucci F, Leonardi M, Trevisan C, Eusebi V. In vivo single voxel 1H MRS of glial brain tumors: correlation with tissue histology and in vitro MRS. Int J Oncol. 1998;12:461-8.

30. Shimizu H, Kumabe T, Shirane R, Yoshimoto T. Correlation between choline level measured by proton MR spectroscopy and Ki-67 labeling index in gliomas. AJNR Am J Neuroradiol. 2000;21:659-65.

31. Gupta RK, Cloughesy TF, Sinha U, Garakian J, Lazareff J, Rubino G, Rubino L, Becker DP, Vinters HV, Alger JR. Relationships between choline magnetic resonance spectroscopy, apparent diffusion coefficient and quantitative histopathology in human glioma. J Neurooncol. 2000;50:215-26.

32. Panigrahy A, Blüml S. Neuroimaging of pediatric brain tumors: from basic to advanced magnetic resonance imaging (MRI). J Child Neurol. 200;24:1343-65. doi: 10.1177/0883073809342129.

33. Young GS. Advanced MRI of adult brain tumors. Neurol Clin. 2007;25:947-73, viii.

34. Griffin JL, Lehtimäki KK, Valonen PK, Gröhn OH, Kettunen MI, Ylä-Herttuala S, Pitkänen A, Nicholson JK, Kauppinen RA. Assignment of 1H nuclear magnetic resonance visible polyunsaturated fatty acids in BT4C gliomas undergoing ganciclovir-thymidine kinase gene therapy-induced programmed cell death. Cancer Res. 2003;63:3195-201.

35. Gillies RJ, Morse DL. In vivo magnetic resonance spectroscopy in cancer. Annu Rev Biomed Eng. 2005;7:287-326.

36. Hakumäki JM, Poptani H, Sandmair AM, Ylä-Herttuala S, Kauppinen RA. 1H MRS detects polyunsaturated fatty acid accumulation during gene therapy of glioma: implications for the in vivo detection of apoptosis. Nat Med. 1999;5:1323-7.

37. Kuesel AC, Sutherland GR, Halliday W, Smith IC. 1H MRS of high grade astrocytomas: mobile lipid accumulation in necrotic tissue. NMR Biomed. 1994 May;7(3):149-55.

38. Kuesel AC, Donnelly SM, Halliday W, Sutherland GR, Smith IC. Mobile lipids and metabolic heterogeneity of brain tumours as detectable by ex vivo 1H MR spectroscopy. NMR Biomed. 1994;7:172-80.

39. Zoula S, Hérigault G, Ziegler A, Farion R, Décorps M, Rémy C. Correlation between the occurrence of 1H-MRS lipid signal, necrosis and lipid droplets during C6 rat glioma development. NMR Biomed. 2003;16:199-212.

40. Lahrech H, Zoula S, Farion R, Rémy C, Décorps M. In vivo measurement of the size of lipid droplets in an intracerebral glioma in the rat. Magn Reson Med. 2001 Mar;45:409-14.

41. Melkus G, Mörchel P, Behr VC, Kotas M, Flentje M, Jakob PM. Short-echo spectroscopic imaging combined with lactate editing in a single scan. NMR Biomed. 2008;21:1076-86.

42. Griffitts J, Tesiram Y, Reid GE, Saunders D, Floyd RA, Towner RA. In vivo MRS assessment of altered fatty acyl unsaturation in liver tumor formation of a TGF alpha/c-myc transgenic mouse model. J Lipid Res. 2009;50:611-22.

43. Griffitts J, Saunders D, Tesiram YA, Reid GE, Salih A, Liu S, Lydic TA, Busik JV, Kang JX, Towner RA. Non-mammalian fat-1 gene prevents neoplasia when introduced to a mouse hepatocarcinogenesis model: Omega-3 fatty acids prevent liver neoplasia. Biochim Biophys Acta. 2010;1801:1133-44.

44. Boren J, Brindle KM. Apoptosis-induced mitochondrial dysfunction causes cytoplasmic lipid droplet formation. Cell Death Differ. 2012;19:1561-70.

45. Blankenberg FG, Katsikis PD, Storrs RW, Beaulieu C, Spielman D, Chen JY, Naumovski L, Tait JF. Quantitative analysis of apoptotic cell death using proton nuclear magnetic resonance spectroscopy. Blood. 1997;89:3778-86.

46. Fan G, Sun B, Wu Z, Guo Q, Guo Y. In vivo single-voxel proton MR spectroscopy in the differentiation of high-grade gliomas and solitary metastases. Clin Radiol. 2004;59:77-85.

47. Delikatny EJ, Cooper WA, Brammah S, Sathasivam N, Rideout DC. Nuclear magnetic resonance-visible lipids induced by cationic lipophilic chemotherapeutic agents are accompanied by increased lipid droplet formation and damaged mitochondria. Cancer Res. 2002;62:1394-400.

48. Martínez-Bisbal MC, Celda B. Proton magnetic resonance spectroscopy imaging in the study of human brain cancer. Q J Nucl Med Mol Imaging. 2009;53:618-30.

49. Liu ZL, Zhou Q, Zeng QS, Li CF, Zhang K. Noninvasive evaluation of cerebral glioma grade by using diffusion-weighted imaging-guided single-voxel proton magnetic resonance spectroscopy. J Int Med Res. 2012;40:76-84.

50. Castillo M, Smith JK, Kwock L, Wilber K. Apparent diffusion coefficients in the evaluation of high-grade cerebral gliomas. AJNR Am J Neuroradiol. 2001;22:60-4.

51. Mardor Y, Roth Y, Ochershvilli A, Spiegelmann R, Tichler T, Daniels D, Maier SE, Nissim O, Ram Z, Baram J, Orenstein A, Pfeffer R. Pretreatment prediction of brain tumors' response to radiation therapy using high b-value diffusion-weighted MRI. Neoplasia. 2004;6:136-42.

52. Chenevert TL, Sundgren PC, Ross BD. Diffusion imaging: insight to cell status and cytoarchitecture. Neuroimaging Clin N Am. 2006;16:619-32, viii-ix.

53. Sugahara T, Korogi Y, Kochi M, Ikushima I, Shigematu Y, Hirai T, Okuda T, Liang L, Ge Y, Komohara Y, Ushio Y, Takahashi M. Usefulness of diffusion-weighted MRI with echo-planar technique in the evaluation of cellularity in gliomas. J Magn Reson Imaging. 1999;9:53-60.

54. Chen J, Xia J, Zhou YC, Xia LM, Zhu WZ, Zou ML, Feng DY, Wang CY. Correlation between magnetic resonance diffusion weighted imaging and cell density in astrocytoma. Zhonghua Zhong Liu Za Zhi. 2005;27(5):309-11.

55. Jain R, Scarpace LM, Ellika S, Torcuator R, Schultz LR, Hearshen D, Mikkelsen T. Imaging response criteria for recurrent gliomas treated with bevacizumab: role of diffusion weighted imaging as an imaging biomarker. J Neurooncol. 2010;96:423-31.

56. Li XR, Cheng LQ, Liu M, Zhang YJ, Wang JD, Zhang AL, Song X, Li J, Zheng YQ, Liu L. DW-MRI ADC values can predict treatment response in patients with locally advanced breast cancer undergoing neoadjuvant chemotherapy. Med Oncol. 2012;29:425-31.

57. Nilsen L, Fangberget A, Geier O, Olsen DR, Seierstad T. Diffusion-weighted magnetic resonance imaging for pretreatment prediction and monitoring of treatment response of patients with locally advanced breast cancer undergoing neoadjuvant chemotherapy. Acta Oncol. 2010;49:354-60.

58. Schmainda KM. Diffusion-weighted MRI as a biomarker for treatment response in glioma. CNS Oncol. 2012 Nov;1:169-80.

59. Moffat BA, Hall DE, Stojanovska J, McConville PJ, Moody JB, Chenevert TL, Rehemtulla A, Ross BD. Diffusion imaging for evaluation of tumor therapies in preclinical animal models. MAGMA. 2004;17:249-59.

60. Vrabec M, Van Cauter S, Himmelreich U, Van Gool SW, Sunaert S, De Vleeschouwer S, Suput D, Demaerel P. MR perfusion and diffusion imaging in the follow-up of recurrent glioblastoma treated with dendritic cell immunotherapy: a pilot study. Neuroradiology. 2011;53:721-31.

61. Tomura N, Narita K, Izumi J, Suzuki A, Anbai A, Otani T, Sakuma I, Takahashi S, Mizoi K, Watarai J Diffusion changes in a tumor and peritumoral tissue after stereotactic irradiation for brain tumors: possible prediction of treatment response. J Comput Assist Tomogr. 2006;30:496-500.

62. Babsky AM, Hekmatyar SK, Zhang H, Solomon JL, Bansal N. Predicting and monitoring response to chemotherapy by 1,3-bis(2-chloroethyl)-1-nitrosourea in subcutaneously implanted 9L glioma using the apparent diffusion coefficient of water and 23Na MRI. J Magn Reson Imaging. 2006;24:132-9.

63. Oh J, Henry RG, Pirzkall A, Lu Y, Li X, Catalaa I, Chang S, Dillon WP, Nelson SJ. Survival analysis in patients with glioblastoma multiforme: predictive value of choline-to-N-acetylaspartate index, apparent diffusion coefficient, and relative cerebral blood volume. J Magn Reson Imaging. 2004;19:546-54.

64. Murakami R, Sugahara T, Nakamura H, Hirai T, Kitajima M, Hayashida Y, Baba Y, Oya N, Kuratsu J, Yamashita Y. Malignant supratentorial astrocytoma treated with postoperative radiation therapy: prognostic value of pretreatment quantitative diffusion-weighted MR imaging. Radiology. 2007;243:493-9.

65. Delikatny EJ, Chawla S, Leung DJ, Poptani H. MR-visible lipids and the tumor microenvironment. NMR Biomed. 2011;24:592-611.

66. Li X, Vigneron DB, Cha S, Graves EE, Crawford F, Chang SM, Nelson SJ. Relationship of MR-derived lactate, mobile lipids, and relative blood volume for gliomas in vivo. AJNR Am J Neuroradiol. 2005;26:760-9.

67. de Certaines JD, Le Moyec L, Sequin F, Eliat PA, Constans JM. Nuclear Magnetic Resonance Spectroscopy of Lipids in Cancer. Curr Org Chem. 2007; 11:529–546.

68. Hakumäki JM, Kauppinen RA. 1H NMR visible lipids in the life and death of cells. Trends Biochem Sci. 2000;25:357-62.

69. Bulik M, Jancalek R, Vanicek J, Skoch A, Mechl M. Potential of MR spectroscopy for assessment of glioma grading. Clin Neurol Neurosurg. 2013;115:146-53.

70. Negendank W, Sauter R. Intratumoral lipids in 1H MRS in vivo in brain tumors: experience of the Siemens cooperative clinical trial. Anticancer Res. 1996 May-Jun;16:1533-8.

71. Barba I, Cabañas ME, Arús C. The relationship between nuclear magnetic resonance-visible lipids, lipid droplets, and cell proliferation in cultured C6 cells. Cancer Res. 1999;59:1861-8.

72. Kao HW, Chiang SW, Chung HW, Tsai FY, Chen CY. Advanced MR imaging of gliomas: an update. Biomed Res Int. 2013;2013:970586.

73. Barker FG 2nd, Davis RL, Chang SM, Prados MD. Necrosis as a prognostic factor in glioblastoma multiforme. Cancer. 1996;77:1161-6.

74. Homma T, Fukushima T, Vaccarella S, Yonekawa Y, Di Patre PL, Franceschi S, Ohgaki H. Correlation among pathology, genotype, and patient outcomes in glioblastoma. J Neuropathol Exp Neurol. 2006;65:846-54.

75. Miller CR, Dunham CP, Scheithauer BW, Perry A. Significance of necrosis in grading of oligodendroglial neoplasms: a clinicopathologic and genetic study of newly diagnosed high-grade gliomas. J Clin Oncol. 2006;24:5419-26.

76. Pierallini A, Bonamini M, Pantano P, Palmeggiani F, Raguso M, Osti MF, Anaveri G, Bozzao L. Radiological assessment of necrosis in glioblastoma: variability and prognostic value. Neuroradiology. 1998;40:150-3.

77. Yamasaki F, Takaba J, Ohtaki M, Abe N, Kajiwara Y, Saito T, Yoshioka H, Hama S, Akimitsu T, Sugiyama K, Arita K, Kurisu K. Detection and differentiation of lactate and lipids by single-voxel proton MR spectroscopy. Neurosurg Rev. 2005;28:267-77.

78. Noch E, Khalili K. Molecular mechanisms of necrosis in glioblastoma: the role of glutamate excitotoxicity. Cancer Biol Ther. 2009;8:1791-7.

79. Padanilam BJ. Cell death induced by acute renal injury: a perspective on the contributions of apoptosis and necrosis. Am J Physiol Renal Physiol. 2003;284:F608-27.

80. Nelson SJ. Analysis of volume MRI and MR spectroscopic imaging data for the evaluation of patients with brain tumors. Magn Reson Med. 2001 Aug;46:228-39.

81. Matsumura A, Isobe T, Anno I, Takano S, Kawamura H. Correlation between choline and MIB-1 index in human gliomas. A quantitative in proton MR spectroscopy study. J Clin Neurosci. 2005;12:416-20.

82. Glunde K, Jie C, Bhujwalla ZM. Molecular causes of the aberrant choline phospholipid metabolism in breast cancer. Cancer Res. 2004;64:4270-6.

83. Podo F. Tumour phospholipid metabolism. NMR Biomed. 1999 Nov;12(7):413-39.

84. Chenevert TL, Sundgren PC, Ross BD. Diffusion imaging: insight to cell status and cytoarchitecture. Neuroimaging Clin N Am. 2006;16:619-32, viii-ix.

85. Chenevert TL, Stegman LD, Taylor JM, Robertson PL, Greenberg HS, Rehemtulla A, Ross BD. Diffusion magnetic resonance imaging: an early surrogate marker of therapeutic efficacy in brain tumors. J Natl Cancer Inst. 2000;92:2029-36.

86. Ellingson BM, Malkin MG, Rand SD, Connelly JM, Quinsey C, LaViolette PS, Bedekar DP, Schmainda KM. Validation of functional diffusion maps (fDMs) as a biomarker for human glioma cellularity. J Magn Reson Imaging. 2010;31:538-48.

87. Koh DM, Collins DJ. Diffusion-weighted MRI in the body: applications and challenges in oncology. AJR Am J Roentgenol. 2007;188:1622-35

CHAPTER II

OKN-007 decreases free radicals levels in a preclinical F98 rat glioma model

2.1 INTRODUCTION

Free radicals, or more generally, reactive oxygen species (ROS) and reactive nitrogen species (RNS), or collectively RONS, are products of normal cellular metabolism [1], and are formed continuously in cells as a consequence of both enzymatic and nonenzymatic reactions [2]. In normal cells, there is a balance between free radical generation and antioxidant defense [3]. Oxidative damage can occur when this balance is unfavorable, affecting a wide range of molecular species including lipids, proteins, and nucleic acids [4]. Oxidative stress plays a major role in the development of chronic and degenerative diseases such as arthritis, aging, autoimmune disorders, cardiovascular, neurodegenerative diseases, and cancer [5].

By combining molecular magnetic resonance imaging (mMRI) and immuno-spin trapping (IST) technologies it is possible to monitor the levels of free radicals *in vivo* in real time [6]. Free radicals that are generated as a result of oxidative stress processes can be trapped by the spin-trapping compound, 5,5-dimethyl-1-pyrroline N-oxide (DMPO), to form DMPO-R adducts (Fig 2.1A), which can be further assessed by IST, a method that uses an antibody against DMPO nitrone adducts. Therefore, the combined morphological image resolution of mMRI, the use of a gadolinium (Gd)-DTPA(diethylene triamine penta acetic acid)-albumin–based contrast agent

(Fig. 2.1B) for signal detection, and the specificity of antibodies for protein/lipid radicals (anti-DMPO antibody, which binds to DMPO-protein/lipid adducts resulting from oxidative-stress-induced formation of protein/lipid radicals), can used to detect *in vivo* oxidative stress–related processes (Fig. 2.1C) [6,7].

This technique allows *in vivo* assessment of oxidation products, permitting the study of specific cause-consequence relationships from specific oxidative events. Recently our group reported for the first time regarding the use of this non-invasive *in vivo* method to detect and quantify free radicals levels in a mouse GL261 glioma model [6].

OKN-007 (2, 4-disulfophenyl-PBN; or disodium 4-[(tert-butyl-imino) methyl] benzene-1,3-disulfonate N-oxide or disufenton; also previously known as NXY-059) is an anticancer drug [9-11] and free radical spin-trapping agent that inhibits upregulation of inducible nitric oxide synthase (iNOS), decreases glutamate excitotoxicity [8], and has exhibited efficacy as a neuroprotectant. Scientific advancements in our understanding and detection of free radicals in biological systems, their importance in carcinogenesis, as well as the introduction of novel therapeutics such as OKN-007 that act by influencing free radicals [8] have dramatically enhanced our ability to assess the role of free radicals in both disease and normal physiology. In this study, we combined mMRI with a Gd-DTPA-albumin-based contrast agent for signal detection with the specificity of an antibody for DMPO nitrone adducts (anti-DMPO probe), to detect *in vivo* free radicals levels in untreated and OKN-007 treated adult F98 rat glioma models. As a negative control, we used a non-specific IgG antibody covalently bound to the albumin-Gd-DTPA-biotin construct. Verification of the presence of the probe in tumor tissues and in glioma cell membranes is also presented.

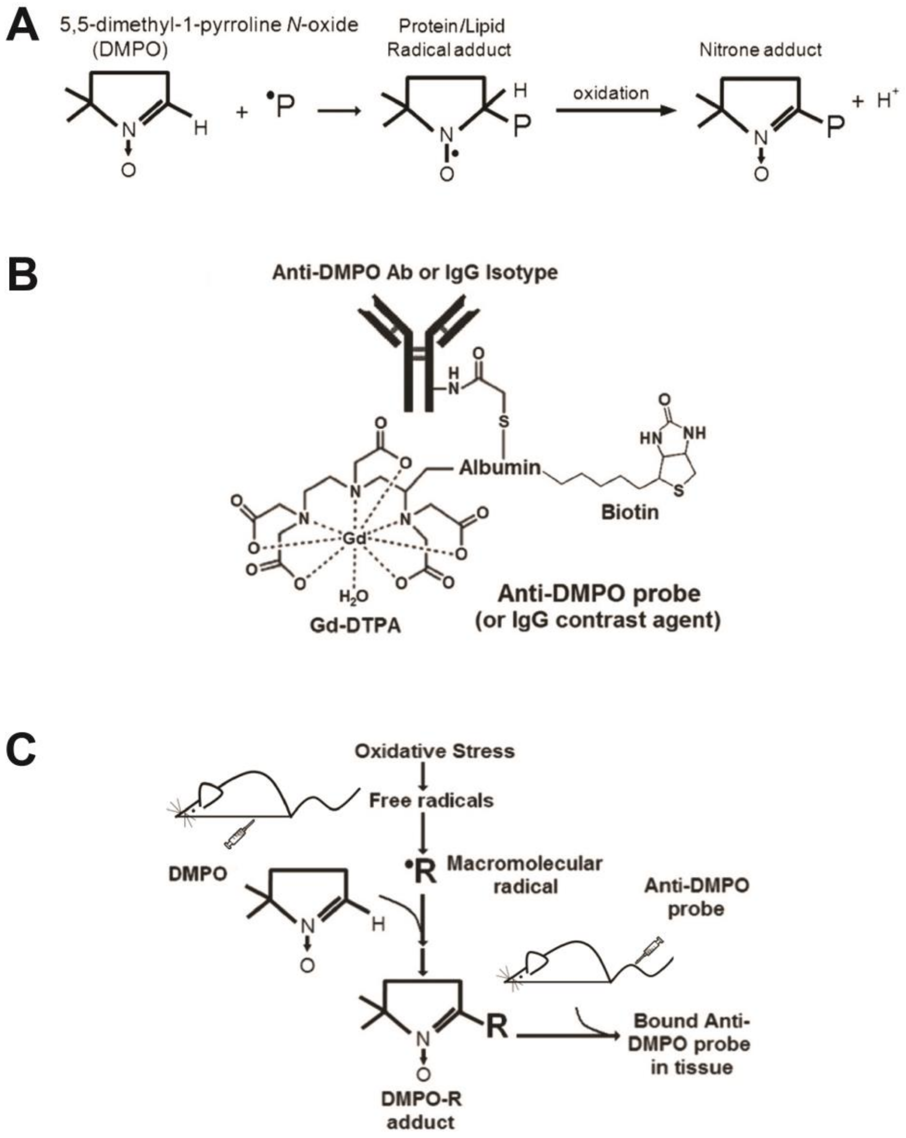

Figure 2.1. Approach for combined in vivo mMRI and IST. (A) Free radicals that are generated as a result of oxidative stress processes can be trapped by the spin-trapping compound, 5,5-dimethyl-1-pyrroline N-oxide (DMPO), to form DMPO-R adducts, which can be further assessed by immuno-spin trapping (IST), a method that uses an antibody against DMPO-nitrone adducts. (B) Schematic structure of anti-DMPO probe or non-specific IgG contrast agent. (C) Immuno-spin trapping of free radicals (•R) with mMRI anti-DMPO probe. DMPO is injected i.p. to trap free radicals and generate nitrone-radical (R) adducts. Anti-DMPO is injected i.v. to target nitrone-R adducts, which can be visualized by mMRI. Modified from Biochimica et Biophysica Acta, 1832(12), Towner RA et al. (2013) [6]. Copyright (2013), with permission from Elsevier.

2.2 MATERIAL AND METHODS

2.2.1 Glioma implantation

The animal studies were conducted with approval from the Institutional Animal Care and Use Committee of the Oklahoma Medical Research Foundation. The F98 rat glioma cell implantation model was prepared as described in our previous work [9]. F98 cells (10^5 in 10-µl volume) were intracerebrally implanted with a stereotaxic device (2 mm lateral and 2 mm anterior to the bregma, and at a 3 mm depth) in a total of 15 Fischer 344 rats (male 200–250 gm; Harlan Laboratories, Indianapolis, Indiana). The animals were divided into two groups: OKN-007 treated (n = 8) and untreated (UT) (n = 7) groups. Both groups were stratified to ensure that tumor sizes were similar before initiation of treatment.

2.2.2 Syntheses of DMPO-specific MRI contrast agents

To recognize the DMPO-radical adducts, we used an anti-mouse/rat monoclonal anti-DMPO antibody bound to a contrast agent. The macromolecular contrast material, biotin–BSA–Gd-DTPA, was prepared using a modification of the method of Dafni *et al*. [12]. The biotin moiety in the contrast material was added to allow histological localization. Biotin– BSA–Gd-DTPA was synthesized as described in Towner *et al.* [13]. A solution of biotin–BSA–Gd-DTPA was added directly to the solution of antibody (anti-DMPO, 200 μg/mL) for conjugation through a sulfo-NHS (N-succinimidyl-S-acetylthioacetate)–EDC (N-succinimidyl 3-(2-pyridyldithio)-propionate) link between albumin and antibody according to the protocol of Hermanson [14]. Sulfo-NHS was added to the solution of biotin–BSA–Gd-DTPA and EDC. This activated solution was added directly to the antibody (anti-DMPO, 200 μg/mL) for conjugation. The mixture was left to react for at least 2 h at 25 °C in the dark. The product was lyophilized and subsequently stored at 4 °C and reconstituted to the desired concentration for injections in phosphate buffer saline (PBS). The final amount of the product, anti-DMPO–biotin–BSA–Gd-DTPA (anti-DMPO probe), that was injected into the rats is estimated to be 200 μg anti-DMPO Ab/injection and 100 mg biotin–BSA–Gd-DTPA/injection. The estimated molecular weight of the anti-DMPO–biotin–BSA–Gd-DTPA probe is estimated to be 232 kDa. As negative control, normal rat-IgG conjugated to biotin–BSA–Gd-DTPA (control IgG contrast agent) was synthesized by the same protocol to generate an isotype contrast agent.

2.2.3 DMPO administration

DMPO (ALX-430-090-G001, Enzo Life Sciences) was administered i.p. (100 mg diluted in 200 μL of saline) 3× daily (every 6 h) for 3 days to trap free radicals during tumor formation. DMPO administration started when the tumor reached the volume of 70-80mm^3 (Fig. 2.2).

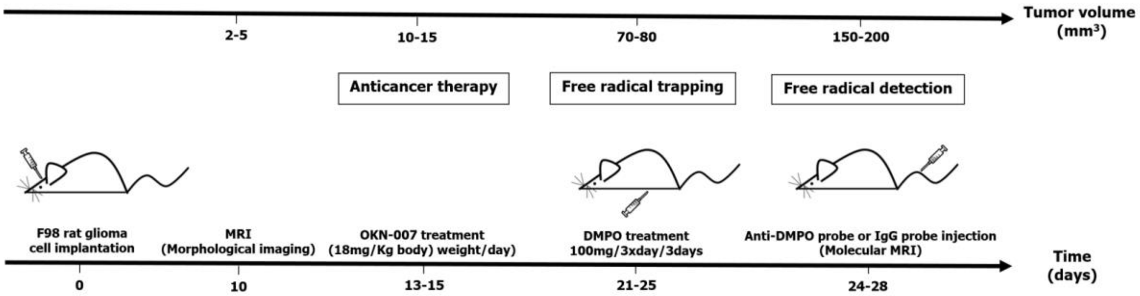

Figure 2.2 Schematic representation of the timeline for the experimental procedures used in this study. Top timeline represents tumor volumes (mm^3), and the bottom timeline refers to the procedures performed (days). F98 rat glioma cell implantation was performed on day 0. Morphological (T_2-weighted) MRI scans were started ten days after the F98 cell implantation and were performed every 2-3 days until the end of the study. OKN-007 treatment (anti-cancer therapy) was initiated when the tumor volumes were between 10 and 15 mm^3. DMPO administration (100 mg diluted in 200 μL of saline) (free radical trapping) was started when the tumor volumes were between 70 and 80 mm^3. After DMPO treatment (at 24-28 days post F98 cell implantation), injection of the anti-DMPO probe was done to detect the presence of free radicals, or the IgG contrast agent was administered as a control.

2.2.4 OKN-007 treatment

OKN-007 (2, 4-disulfophenyl-N-tert-butyl nitrone, Ryss Laboratories, Union City, CA) was administered as an anticancer agent to the rats in their drinking water at a concentration of 0.018% w/v. The treatment started at 13-15 days after glioma cell implantation, when the tumor volumes were between 10 and 15 mm^3 (Fig. 2.2). The treatment was administered continuously until the end of the study. Rats receiving normal drinking water were used as UT controls. The amount of OKN-007 consumed by each rat, which were housed in separate cages, was determined by weighing water bottles each day. No significant deviation was observed in the volume of liquid uptake of compound in these rats. The average intake of OKN-007 was approximately 10 mg/kg/day. The F98 glioma bearing rats were divided in three different treatment groups: (1) OKN-007 treated animals + DMPO administration + anti-DMPO probe (n=5), (2) Untreated animals + DMPO administration + anti-DMPO probe (n=7), (3) Untreated animals + DMPO administration + IgG probe (n=4). The overall experimental scheme is shown in Fig. 2.2.

2.2.5 MR Imaging

All MR imaging experiments were conducted on a Bruker Biospec 7.0 T (Bruker Biospin, Germany) using a 72-mm quadrature volume coil for signal transmission and a rat head surface coil for signal reception. Tumor morphology was observed on T_2-weighted images obtained with the application of the spin echo pulse sequence, RARE (Rapid acquisition with relaxation enhancement) using a TR (repetition time) = 5000 ms, TE (echo time) = 63 ms, 20 transverse 1 mm-thick slices, a field of view of 3.5 × 3.5 cm^2 with an in-plane resolution of 137 × 137 μm^2. Starting ten days after the F98 tumor cells inoculation, each rat brain was imaged *in vivo* every 2-3 days until the end of the study. Subsequently for the 3-day DMPO treatment, rats were injected intravenously with anti-DMPO or non-specific-IgG antibodies tagged with a biotin–Gd-DTPA–albumin-based contrast agent (200 μL/kg; 1 mg antibody/kg; 0.4 mmol Gd^{+3}/kg). Rat brains were imaged at 0 (pre-contrast), 20, 40, 60, 120 and 180 min intervals post-probe or -contrast agent injection.

T_1-weighted images were obtained using a variable TR RARE (rapid acquisition relaxation-enhanced) sequence (TR 200, 400, 800, 1200 and 1600 ms; TE 15 ms, FOV 2×2 cm2, matrix 256×256, slice thickness 0.5 mm, 2 slices, and 2 steps per acquisition).

2.2.6 Calculation of relative probe concentration

Relative probe (contrast agent) concentrations were calculated to assess the levels of free radicals in each animal. A contrast difference image was created from the pre- and (120 minutes) postcontrast datasets for the slice of interest, by computing the difference in signal intensity between the post-contrast and the pre-contrast image on a pixel basis. On the difference image, three regions of interest (ROI) of equal size ($0.02cm^2$) were drawn on the areas with the highest T_1 relaxation in the tumor parenchyma and contralateral side of the brain of each animal after the probe (anti-DMPO or non-immune-IgG) injection at the TR 800 ms. The values obtained from the ROIs in the tumor region were normalized to the contralateral side. The T_1 relaxation value of the specified ROIs was computed from all the pixels in the ROI by the following equation [15] (processed by ParaVision 4.0, Bruker): $S(TR) = S_0(1 - e^{-TR/T1})$, where TR is the repetition time, S_0 is the signal intensity (integer machine units) at $TR \gg T_1$ and TE = 0, and T_1 is the constant of the longitudinal relaxation time. An overlay of the contrast difference image and T_1-weighted image was generated using the 3D Analysis Software for Life Sciences Amira® (Fei, Hillsboro, Oregon).

2.2.7 Immunohistochemistry

Whole brains from each rat in each treatment group were removed and embedded in Optimal Cutting Temperature (OCT) compound and frozen in liquid nitrogen. Frozen tissue blocks were sectioned at 10 µm, mounted on positive-charged slides, and air-dried for 30 minutes. Sections were fixed in acetone, and incubated with Horseradish Peroxidase (HRP) polymer kit (Biocare Medical), stained with DAB chromogen (Vector Labs), and then counterstained with hematoxylin (Vector Labs).

2.2.8 Gold labeling immunoelectron microscopy

Brain tissue was removed and cut to size of about 2cm and 3-5mm thick then fixed in 4% paraformaldehyde + 0.1% glutaraldehyde in 0.1M phosphate buffer (PB) for 1 hour at room temperature or at 4°C, and then washed thoroughly with PB (pH 7.3). Tissue was trimmed further to 1-2mm pieces. Osmication was omitted for labelling procedure. Dehydration was in an ethanol series (50%, 70%, 80%, at 15 min each). Tissue was placed in 2:1 LR White resin (Electron Microscopy Sciences, PA) to 70% ethanol for 1 hour to avoid tissue shrinkage, and then further infiltrated in 100% LR White for 1 hour, overnight, and then two changes for 30 minutes. Tissue was added to gelatin capsules and LR White polymerized at 50°C for 24 hours. Gold-silver sections were placed on nickel grids coated with formvar or colloidin. Sections on grids were protein blocked in Aurion goat gold conjugate (Electron Microscopy Sciences, PA) for 30 minutes, washed in PBS-0.2% bovine serum albumin 3x for 5 minutes at pH 7.4 (Electron Microscopy Sciences, PA). Aurion ultra small gold conjugate – goat anti-Biotin (Electron Microscopy Sciences, PA) in PBS-0.2% BSA-c was applied at 1:100 for overnight at 4°C or for 4 hours at room temperature. Grids were washed in PBS-0.2% BSA-c (pH 7.4), 6x for 5minutes; in PBS, 3x for 5 minutes; in distilled water 5x for 2 minutes. Silver enhancement was done by placing grids on a droplet of Aurion R-Gent SE-EM enhancement mixture (Electron Microscopy Sciences, PA) for 90 minutes, then washed in distilled water. Controls involved sections with no secondary antibody (anti-Biotin) and no silver enhancement. Sections were stained with uranyl acetate for 15 minutes followed by lead citrate for 3 minutes. Sections were viewed with a Zeiss T109 electron microscope with Gatan digital micrograph software operated at 80kV.

2.2.9 Statistical analysis

Statistical differences between the probe-administered and control groups were analyzed with an unpaired, two-tailed Student t test using commercially available software (InStat; GraphPad Software, San Diego, CA, USA). A $p < 0.05$ was considered to indicate a statistically significant difference.

2.3 RESULTS

Representative examples of images obtained in F98 glioma-bearing rats are shown in Fig. 2.3. Pre- and post DMPO probe contrast images are shown in Figs. 2.3A and B, respectively. A T_2-weighted morphological image depicts the tumor location (outlined region in Fig. 2.3C). A difference image illustrating increased anti-DMPO probe accumulation is shown in Fig. 2.3D, along with representative ROIs in the tumor and contralateral (normal) brain regions.

There were differences in the levels of free radicals detected in the different treatment groups. OKN-007 was found to significantly decrease ($p = 0.0411$) the levels of free radicals detected in the treated group compared to the untreated animals who were both administered the anti-DMPO probe. There was no significant difference in the level of free radicals detected between the OKN-

007 treated group and the group that received the IgG probe (negative control group) (Fig 2.4A-D).

The difference between the amounts of anti-DMPO probe in untreated and OKN-007 treated F98 rat gliomas was confirmed by using a streptavidin horseradish peroxidase (HRP) detection system (Fig. 2.5), whereby the streptavidin-HRP bound to the biotin moiety of the anti-DMPO probe (Fig. 2.1B) in excised tumor tissues . The amount of anti-DMPO probe was elevated in the UT F98 glioma rats administered with the anti-DMPO probe (Fig 2.5A), but not the ones administered with OKN-007 (Fig 2.5B) and/or the UT glioma-bearing rats given the non-specific IgG contrast agent (Fig 2.5C).

Ex vivo immunoelectron microscopy of F98 rat glioma tissues after administration of gold-labeled anti-biotin was performed to determine the sub-cellular localization of the anti-DMPO probe (Fig 2.6). The gold-labeled anti-biotin was found to be distributed within the plasma membrane, as well as the nuclei of the F98 tumor cells in rats administered the anti-DMPO *in vivo* (Fig 2.6A). In comparison the control tumor cells (previously administered the non-specific IgG contrast agent in vivo) only had the gold-labeled anti-biotin within cell nuclei (Fig. 2.6B).

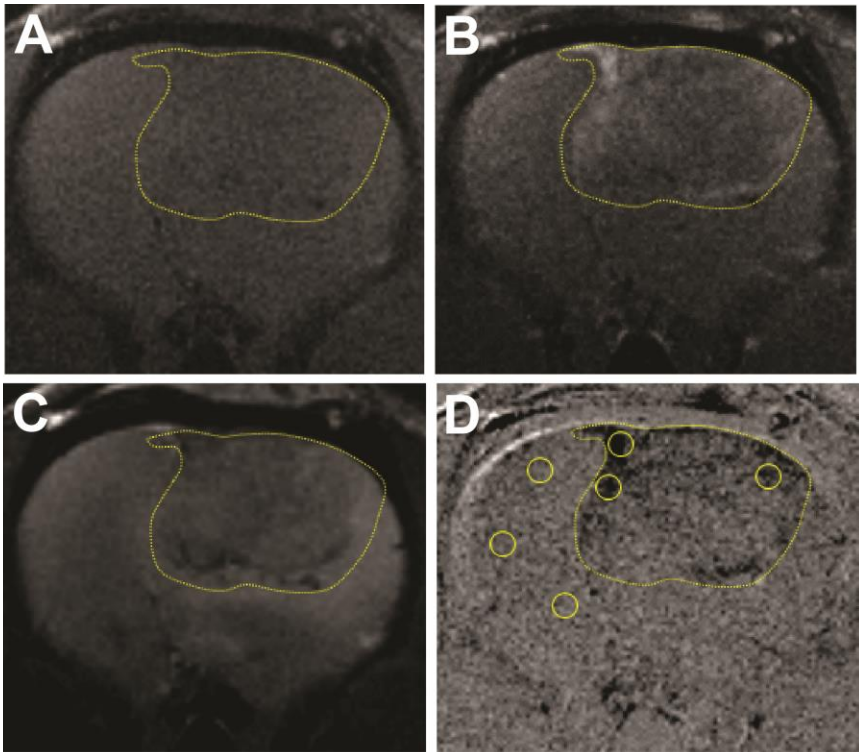

Figure 2.3. Morphological MR images obtained before and 2 hrs after injection of anti-DMPO probe (contrast agent) in a F98 rat glioma moldel. (A) Representative T_1-weighted image before injection of the anti-DMPO probe. (B) Representative T_1-weighted image 2 hours after injection of the anti-DMPO probe. (C) Representative T_2-weighted image of F98 rat glioma. (D) Representative difference image, which is the subtraction between the T_1 images of pre- and 2 hrs after injection of the contrast agent (A-B). The dark regions in the tumor depict areas of increased uptake of the anti-DMPO probe. Representative ROIs in the tumor and contralateral side of the brain are illustrated as circles in each region. The tumor is delineated by a dotted line in each panel.

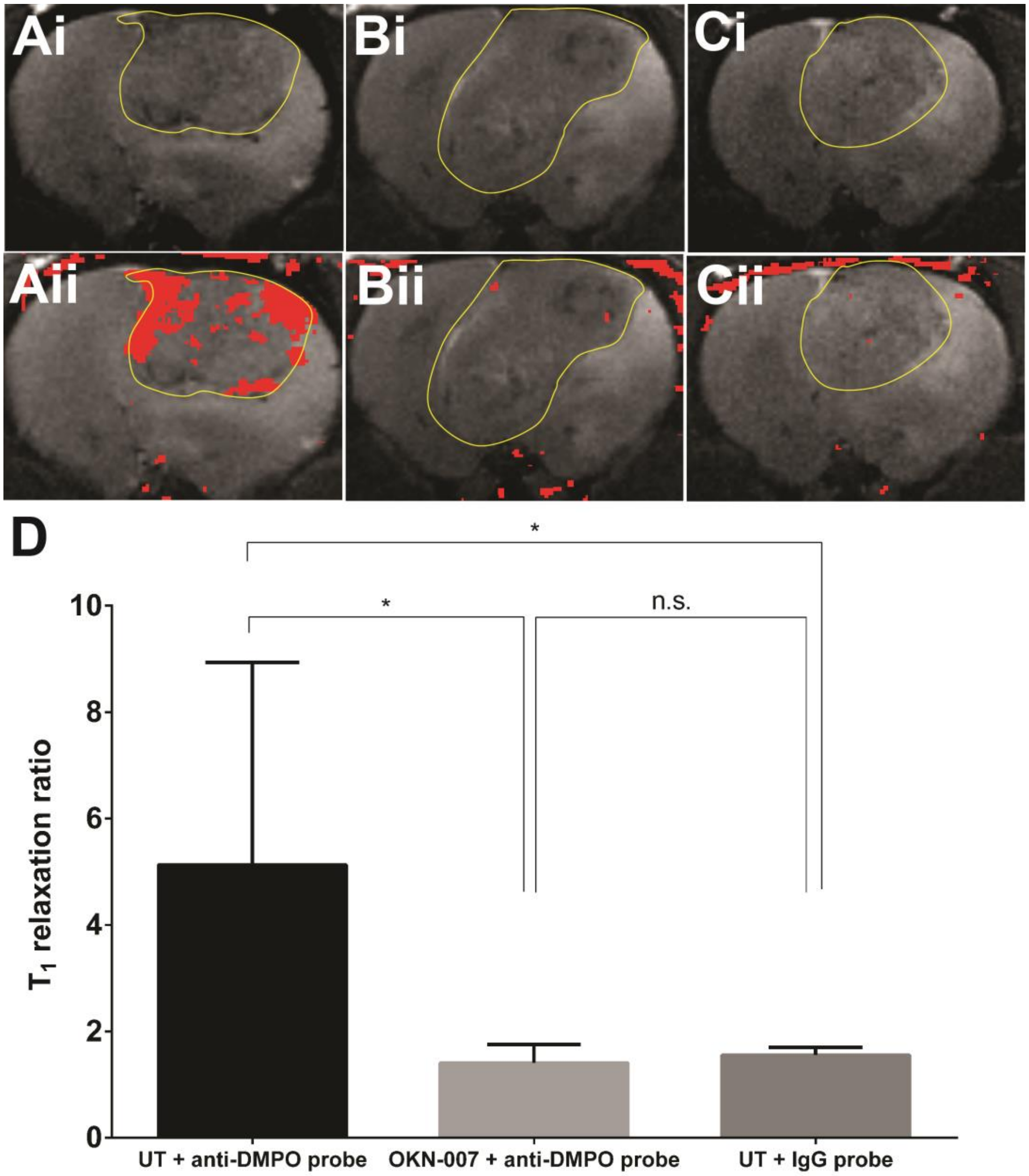

Figure 2.4. mMRI detection of free radical adducts in a F98 rat glioma model. Representative MR images from: (A) Untreated + anti-DMPO probe, (B) OKN-treatment + anti-DMPO probe, (C) Untreated + IgG probe, F98 rat gliomas. (A-Ci) T_2-weighted images of F98 glioma. (A-Cii) T_2-weighted images overlayed with a difference T_1-weighted image (red), which was the subtraction between the 2 hr post-contrast and the pre-contrast images after injection of either the anti-DMPO probe or the IgG contrast agent. Overlays of the contrast difference images and the T_2-weighet images were generated using the 3D Analysis Software for Life Sciences Amira®. (D) OKN-007 was found to significantly decrease (*p* = 0.0411) (1.407 ± 0.1548, n=5) the levels of free radicals in the treated group compared to the untreated animals (5.131 ± 1.437, n=7), which both received the anti-DMPO probe. There was no significant difference between the OKN-007 treated group and the untreated animals that received the IgG contrast (negative control group). Values are represented as means ± SD. Asterisks indicate statistically significant differences (*p < 0.05). UT: untreated animals.

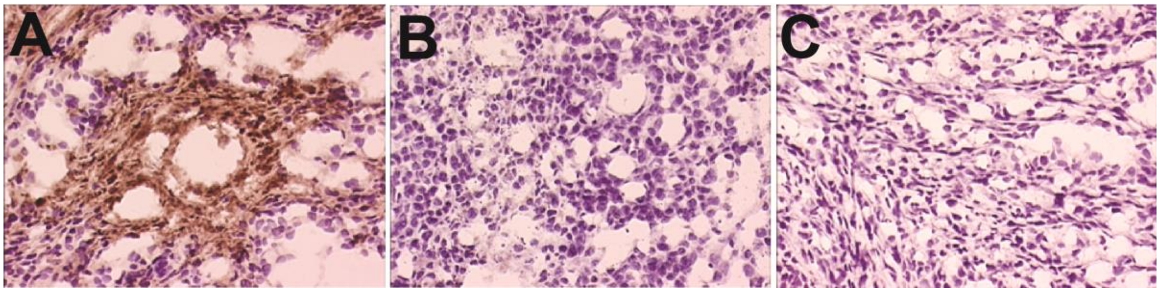

Figure 2.5. ***Ex vivo*** **detection of the anti-DMPO probe in F98 rat gliomas with streptavidin horseradish peroxidase (HRP).** Streptavidin-HRP binds to the biotin moiety of the anti-DMPO probe. The detection of the anti-DMPO probe is elevated in untreated F98 gliomas administered with the anti-DMPO probe (A, brown stain), but not for those treated with OKN-007 (B). There is no detection of sustained non-specific IgG contrast agent with streptavidin-HRP (C). Magnification = 200×.

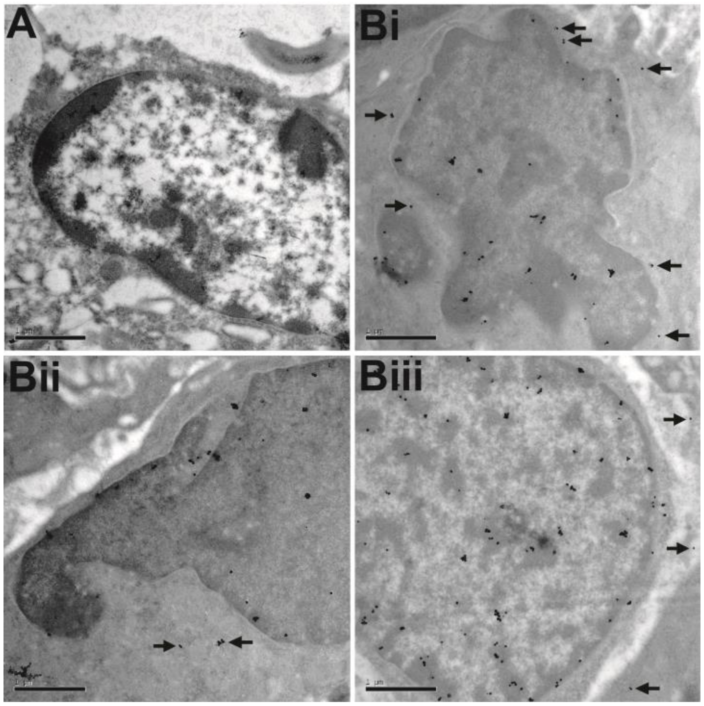

Figure 2.6. Immunoelectron microscopy detection of the anti-DMPO probe in the plasma membrane and cell nuclei in F98 rat gliomas. The biotin moiety of the anti-DMPO probe was targeted with gold-anti-biotin. (A) F98 glioma tumor cells administered a non-specific IgG contrast agent *in vivo*, and stained with gold-anti-biotin. Note no detection of gold-anti-biotin colloid in either the plasma membrane or cell nucleus. (Bi-iii) Gold-anti-biotin colloids were detected within the plasma membrane (black arrows) and cell nuclei of F98 tumor cells administered the anti-DMPO probe. Scale bar = 1μm. Magnification = 20,000×.

2.4 DISCUSSION

RONS are now appreciated to play a role in the signaling involved in the regulation of various physiological processes, and therefore are essential for maintaining normal cell function. However, overproduction and cumulative production of RONS can cause damage to DNA, proteins, lipids, and other macromolecules, and induce cell death. Consequently, oxidative stress and oxidative damage have been implicated in the pathogenesis and progression of many human diseases, including cancer [16]. Although the exact mechanism by which RONS promote tumorigenesis remains poorly understood, it is known that DNA damage appears to play a key role in cancer development. For instance, RONS induce DNA damage, where the reaction of free radicals with DNA generates strand breaks, base modifications, and DNA protein cross-links [2].

Apart from DNA damage, other mechanisms also have been proposed to explain the connection between free radicals and human cancer development, mutation, and transformation. One mechanism underlying these actions is the activation of transcription factors such as hypoxia inducible factor (HIF)-1α, which leads to the induction of VEGF (vascular endothelial growth factor), a key mediator of angiogenesis and tumor progression. Activation of HIF-1α also leads to the up regulation of metalloproteinases (MMP), which are important in tumor invasion and metastasis [17]. RONS also contribute to tumor survival and progression by facilitating immunosuppression. Both reactive species up regulate the activity of myeloid suppressor cells, which are abundant in the tumor microenvironment and function to inhibit anti-tumor adaptive immunity [18]. Furthermore, various reports have demonstrated that growth factors such as PDGF (platelet-derived growth factor) and EGF (epidermal growth factor) can stimulate RONS production. RONS, in turn, may directly or indirectly activate several mitogen-activated protein kinases (MAPKs) [19, 20], the AKT pathway [21], and the nuclear factor of kappa light polypeptide gene enhancer in B-cells (NF-kB) [22]. Also, NF-kB induces iNOS (inducible nitric oxide synthase) leading to increased production of reactive nitrogen species, which might result in generation and accumulation of additional DNA mutations that drive tumor progression (Fig. 2.7) [23]. Additionally, the expression of iNOS in tumor cells induce the expressions of MMP-1 and -2, and VEGF-C and -D, and is associated with tumor growth, invasion, and lymphangiogenesis [24-25].

All tissues and organs are susceptible to free radical damage. The human brain is especially vulnerable to free radical attack because of its high oxygen consumption and high concentrations of easily oxidizable polyunsaturated fatty acids [26]. In addition, the brain's antioxidant capacity is lower compared with other organs, and thus the brain may be more susceptible to oxidative damage [26].

Free radical scavengers, such as spin traps, have been studied by many researchers. The most widely studied spin trap agents are members of the nitrone class of free radical spin trapping agents, in which a nitrone moiety traps ROS in addition to other radical species [27-30]. Nitrone spin traps have become increasingly attractive prospects for the treatment of a variety of pathological conditions, particularly because of the stable nitroxides that are formed after ROS trapping [28, 31]. The nitrone chemical structure in its simplest form can be represented as X-CH=NO-Y. The N–O group effectively traps oxygen, carbon, and sulfur-centered radicals to produce a stable nitroxide radical (-N–O.) [32]. The nitroxide is then readily excreted from the body via the kidneys, as is the excess nitrone [33].

OKN-007 is a nitrone free radical spin-trapping agent that has exhibited efficacy as a neuroprotectant, and is involved in the inhibition of the upregulation of inducible nitric oxide synthase and decreasing glutamate excitotoxicity [8]. OKN-007 is a small molecule that can traverse the blood-brain barrier, and has anti-inflammatory, antioxidant, and proapoptotic properties [8, 34]. Our group has also established that OKN-007 is an effective anticancer agent in rodent pre-clinical glioma models [9-11], and it is currently undergoing clinical trial assessment as a new investigational drug for recurrent adult glioblastomas.

There are several methods that have been used to monitor the levels of free radicals *in vitro* and *in vivo*. Recently, our group reported the *in vivo* detection of free radicals in a G261 mouse glioma model by combining immuno-spin-trapping (IST) and molecular magnetic resonance imaging (mMRI) [6]. It was previously demonstrated *in vitro* that OKN-007 is an effective free radical scavenger for hydroxyl radicals [35]. In the present study we demonstrated, through the use of the combined IST and mMRI techniques, that OKN-007 was able to decrease the levels of free radicals in a preclinical F98 rat glioma model.

Specifically, we combined mMRI with a Gd-DTPA-albumin-based contrast agent for signal detection with the specificity of an antibody for DMPO nitrone adducts (anti-DMPO probe), to detect *in vivo* free radical levels in untreated and OKN-007 treated adult F98 rat gliomas. As a negative control, we used a non-specific IgG antibody covalently bound to the albumin-Gd-DTPA-biotin construct. To calculate the T_1 relaxation, we normalized the T_1 relaxation values from the tumor area to the contralateral side of the brain in each animal dataset. We used the contralateral side of the brain to normalize the T_1 relaxation values of the tumor region as we detected no significant difference in the T_1 relaxation values in the three treatment groups, 120 minutes after the administration of the either the anti-DMPO probe or non-specific IgG contrast agent (UT + anti-DMPO probe, 3426 ± 322.5ms; OKN-007 + anti-DMPO probe, 3363 ± 573.1ms; UT + IgG probe, 3498 ± 313.0ms). OKN-007 was found to significantly decrease ($p = 0.0411$) the levels of free radicals in the treated group compared to the untreated animals administered with the anti-DMPO probe. There was no significant difference between the OKN-007 treated group and the group that received the IgG probe (negative control group) (Fig 2.4A-D), indicating that OKN-007 reduced free radical levels to undetectable levels. The presence of the anti-DMPO probe was also confirmed by targeting the biotin moiety of the anti-DMPO probe with streptavidin HRP (Fig. 2.5A). There was little or no detection of HRP in the OKN-007-treated sample or the IgG administered tumor tissue (Figs. 2.5B and C).

We have already demonstrated with immunofluorescence that the anti-DMPO probe binds to membrane bound free radicals in GL261 glioma tumor cells [6]. Here we also used immunoelectronmicroscopy to demonstrate the presence of the anti-DMPO probe in the cytoplasm/membrane and cell nuclei of F98 glioma tumor cells. In this technique, anti-biotin-gold was used to bind specifically to the biotin group of the anti-DMPO probe. The IgG contrast agent, which also has a biotin moiety, was not detected with the anti-biotin-gold in the plasma membrane. Likewise the level of nuclear staining was lower for the IgG contrast agent administered sample. However, nuclei staining was found in the glioma cells administered the anti-DMPO probe. Due to the size of the anti-DMPO probe, we do not think that this probe could be taken up by the cell nuclei. There are three possible other reasons that could account for nuclear staining for biotin. It may be possible that the nuclear positive gold-staining could be caused by non-specific staining as a result of secondary labelling of biotin in newly replicated DNA [36, 37], or endogenous biotin, which has widely been taken up in the cell nuclei [38], or biotin could have come from biodegradation of the anti-DMPO probe. As the control IgG contrast agent sample had little staining for biotin, we surmise that the biotin detected in the cell nuclei from the glioma sample administered the anti-DMPO probe was from biodegradation of the probe which had accumulated in the glioma cells of untreated tumors.

Redox pathways may be potential targets for cancer therapy. Reduced intracellular RONS levels through the administration of antioxidants impairs cell proliferation and survival in some types of cancers, such as gliomas [39], colorectal cancer [40], and lymphomas [41]. Martín *et al* [39] demonstrated that N-acetylcysteine could decrease C6 glioma cell proliferation, inducing a cell cycle arrest in the G_0/G_1 phase and markedly up-regulating p21 expression [39]. *N*-acetylcysteine also decreased AKT activity, extracellular signal-regulated kinase 1/2, and the redoxsensitive transcription factor NF-κB, all of which are RONS-related, and seem to be in close connection with cell proliferation [39].

OKN-007 may share some of the antioxidant mechanisms of action of N-acetylcysteine. It has been previously shown that nitrones decrease iNOS (inducible nitric oxide synthase) activity (Fig. 2.7) [42], which occur in brain tumors [43]. Furthermore, they can also down-regulate cytokines [tumor necrosis factor alpha (TNF-α), interferon-gamma (IFN-γ)] and NF-κB expression [44], which promotes iNOS expression (Fig. 2.7) [45]. Our data also suggests that the the inhibition of the tumor growth by OKN-007 in different preclinical glioma models, as we have reported previously [9-11], may in part be due to the reduction of free radicals, as demonstrated in this study on F98 gliomas.

2.5 CONCLUSION

This is the first attempt at detecting *in vivo* levels of free radicals from a rat glioma model and assessing the free radical scavenging capability of a nitrone anticancer agent. OKN-007 was found to dramatically reduce free radical levels compared to untreated gliomas. mMRI provides the advantage of *in vivo* image resolution as well as the assessment of the spatial location of oxidative stress events in heterogeneous tissues or organs.

This method can potentially be applied towards other types of cancers for the *in vivo* assessment of macromolecular free radical levels. The results indicate that OKN-007 treatment substantially decreased free radical levels in a F98 rat glioma model.

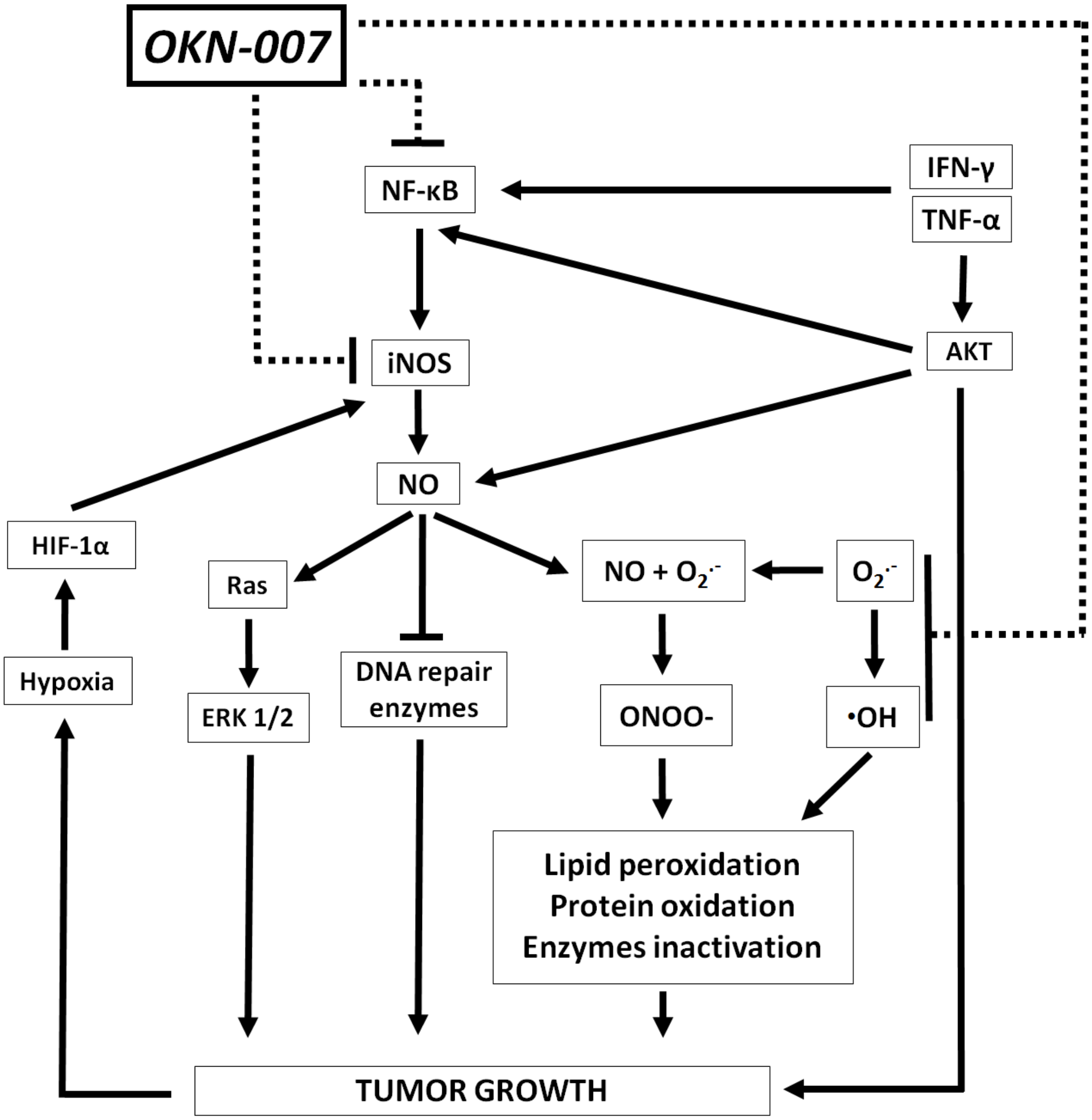

Figure 2.7. Schematic representation of possible antioxidant mechanisms-of-action for the anti-cancer agent OKN-007. OKN-007 scavenges radicals associated with tumor (e.g. glioma) growth. OKN-007 decreases iNOS (inducible nitric oxide synthase) activity and also down-regulates some proinflammatory cytokines (TNF-α and IFN-γ) and NF-κB expression, which promotes iNOS expression and NO formation. ERK 1/2: extracellular signal-regulated kinase 1/2; HIF-1α: hypoxia inducible factor-1α; IFN-γ: interferon-gamma; iNOS: inducible nitric oxide synthase; NO: nitric oxide; ONOO$^-$: peroxynitrite; $O_2^{\cdot -}$: superoxide anion, TNF-α: tumor necrosis factor alpha.

2.6 REFERENCES

1. Pala FS, Gürkan H. The role of free radicals in ethiopathogenesis of diseases. Adv. Mol. Biol. 2008: 1-9.

2. Lobo V, Patil A, Phatak A, Chandra N. Free radicals, antioxidants and functional foods: Impact on human health. Pharmacogn Rev. 2010;4:118-26.

3. Devi GS, Prasad MH, Saraswathi I, Raghu D, Rao DN, Reddy PP. Free radicals antioxidant enzymes and lipid peroxidation in different types of leukemias. Clin Chim Acta. 2000;293:53-62.

4. McCord JM. The evolution of free radicals and oxidative stress. Am J Med. 2000;108(8):652-9.

5. Pham-Huy LA, He H, Pham-Huy C. Free radicals, antioxidants in disease and health. Int J Biomed Sci. 2008;4: 89–96.

6. Towner RA, Smith N, Saunders D, De Souza PC, Henry L, Lupu F, Silasi-Mansat R, Ehrenshaft M, Mason RP, Gomez-Mejiba SE, Ramirez DC. Combined molecular MRI and immuno-spin-trapping for in vivo detection of free radicals in orthotopic mouse GL261 gliomas. Biochim Biophys Acta. 2013;1832:2153-61.

7. Towner RA, Smith N, Saunders D, Henderson M, Downum K, Lupu F, Silasi-Mansat R, Ramirez DC, Gomez-Mejiba SE, Bonini MG, Ehrenshaft M, Mason RP. In vivo imaging of immuno-spin trapped radicals with molecular magnetic resonance imaging in a diabetic mouse model. Diabetes. 2012;61:2405-13.

8. Floyd RA, Kopke RD, Choi CH, Foster SB, Doblas S, Towner RA. Nitrones as therapeutics. Free Radic Biol Med. 2008;45:1361-74.

9. Towner RA, Gillespie DL, Schwager A, Saunders DG, Smith N, Njoku CE, Krysiak RS 3rd, Larabee C, Iqbal H, Floyd RA, Bourne DW, Abdullah O, Hsu EW, Jensen RL. Regression of glioma tumor growth in F98 and U87 rat glioma models by the Nitrone OKN-007. Neuro Oncol. 2013;15:330-40.

10. He T, Doblas S, Saunders D, Casteel R, Lerner M, Ritchey JW, Snider T, Floyd RA, Towner RA. Effects of PBN and OKN007 in rodent glioma models assessed by 1H MR spectroscopy. Free Radic Biol Med. 2011;51:490-502.

11. Garteiser P, Doblas S, Watanabe Y, Saunders D, Hoyle J, Lerner M, He T, Floyd RA, Towner RA. Multiparametric assessment of the anti-glioma properties of OKN007 by magnetic resonance imaging. J Magn Reson Imaging. 2010;31:796-806.

12. Dafni H, Landsman L, Schechter B, Kohen F, Neeman M. MRI and fluorescence microscopy of the acute vascular response to VEGF165: vasodilation, hyper-permeability and lymphatic uptake, followed by rapid inactivation of the growth factor. NMR Biomed. 2002;15:120-31.

13. Towner RA, Smith N, Doblas S, Tesiram Y, Garteiser P, Saunders D, Cranford R, Silasi-Mansat R, Herlea O, Ivanciu L, Wu D, Lupu F. In vivo detection of c-Met expression in a rat C6 glioma model. J Cell Mol Med. 2008;12:174-86.

14. Hermanson, GT. Bioconjugate Techniques. San Diego: Academic, 1996.

15. Haacke, EM. Magnetic Resonance Imaging: Physical Principles and Sequence Design. New York, NY: Wiley-Liss, 1999.

16. Holmstrom KM, Finkel T. Cellular mechanisms and physiological consequences of redox-dependent signalling. Nat Rev Mol Cell Biol. 2014;15:411–421.

17. Halliwell B. Biochemistry of oxidative stress. Biochem Soc Trans. 2007; 35:1147-50.

18. Mantovani A, Sica A, Allavena P, Garlanda C, Locati M. Tumor-associated macrophages and the related myeloid-derived suppressor cells as a paradigm of the diversity of macrophage activation. Hum Immunol. 2009;70:325-30.

19. Mesquita FS, Dyer SN, Heinrich DA, Bulun SE, Marsh EE, Nowak RA. Reactive oxygen species mediate mitogenic growth factor signaling pathways in human leiomyoma smooth muscle cells. Biol Reprod. 2010;82:341-51.

20. Sundaresan M, Yu ZX, Ferrans VJ, Irani K, Finkel T. Requirement for generation of H2O2 for platelet-derived growth factor signal transduction. Science. 1995;270:296-269.

21. Mochizuki T, Furuta S, Mitsushita J, Shang WH, Ito M, Yokoo Y, Yamaura M, Ishizone S, Nakayama J, Konagai A, Hirose K,Kiyosawa K, Kamata T. Inhibition of NADPH oxidase 4 activates apoptosis via the AKT/apoptosis signal-regulating kinase 1 pathway in pancreatic cancer PANC-1 cells. Oncogene. 2006;25:3699-707.

22. Deshpande SS, Angkeow P, Huang J, Ozaki M, Irani K. Rac1 inhibits TNF-alpha-induced endothelial cell apoptosis: dual regulation by reactive oxygen species. FASEB J 200;14:1705–1714.

23. Bogdan C. Nitric oxide and the immune response. Nat Immunol. 2001;2:907-16.

24. Nakamura Y, Yasuoka H, Tsujimoto M, Yoshidome K, Nakahara M, Nakao K, Nakamura M, Kakudo K. Nitric oxide in breast cancer: induction of vascular endothelial growth factor-C and correlation with metastasis and poor prognosis. Clin Cancer Res. 2006;12:1201-7.

25. Viswanathan AN, Feskanich D, Schernhammer ES, Hankinson SE. Aspirin, NSAID, and acetaminophen use and the risk of endometrial cancer. Cancer Res. 2008;68:2507-2513.

26. Halliwell B, Gutteridge JM. Free Radicals in Biology and Medicine. Oxford: Oxford UP, 2007.

27. Anderson KM, Ells G, Bonomi P, Harris JE. Free radical spin traps as adjuncts for the prevention and treatment of disease. Med Hypotheses 1999;52:53–57.

28. Becker DA. Diagnostic and therapeutic applications of azulenyl nitrone spin traps. Cell Mol Life Sci 1999;56:626–633.

29. Floyd RA. Antioxidants, oxidative stress, and degenerative neurological disorders. Proc Soc Exp Biol Med 1999;222:236–245.

30. Hensley K, Carney JM, Stewart CA, Tabatabaie T, Pye Q, Floyd RA. Nitrone-based free radical traps as neuroprotective agents in cerebral ischaemia and other pathologies. Int Rev Neurobiol 1997;40:299–317.

31 Lapchak PA, Araujo DM. Reducing bleeding complications after thrombolytic therapy for stroke: Clinical potential of metalloproteinase inhibitors and spin trap agents. CNS Drugs 2001;15:819–829.

32. Lapchak PA, Araujo DM, Song D, Wei J, Zivin JA. Neuroprotective effects of the spin trap agent disodium-[(tert–butylimino)methyl]benzene-1,3-disulfonate N-oxide (generic NXY-059) in a rabbit small clot embolic stroke model: Combination studies with the thrombolytic tissue plasminogen activator. Stroke 2002;33:1411–1415.

33. Lapchak PA, Araujo DM. Development of the nitrone-based spin trap agent NXY-059 to treat acute ischemic stroke. CNS Drug Rev. 2003;9:253-262.

34. Floyd RA, Chandru HK, He T, Towner R. Anti-cancer activity of nitrones and observations on mechanism of action. Anticancer Agents Med Chem. 2011;11:373-379.

35 Williams HE, Claybourn M, Green AR. Investigating the free radical trapping ability of NXY-059, S-PBN and PBN. Free Radic Res. 2007;41:1047-52.

36. Zempleni J. Uptake, localization, and noncarboxylase roles of biotin. Annu Rev Nutr. 2005;25:175-96.

37. Hiriyanna KT, Varkey J, Beer M, Benbow RM. Electron microscopic visualization of sites of nascent DNA synthesis by streptavidin-gold binding to biotinylated nucleotides incorporated in vivo. J Cell Biol. 1988;107:33-44.

38. Nikiel B, Chekan M, Jarzab M, Lange D. Endogenous avidin biotin activity (EABA) in thyroid pathology: immunohistochemical study. Thyroid Res. 2009;2(1):5.

39. Martin V, Herrera F, Garcia-Santos G, Antolin I, Rodriguez-Blanco J, Rodriguez C. Signaling pathways involved in antioxidant control of glioma cell proliferation. Free Radic Biol Med. 2007;42:1715–1722.

40. Chinery R, Beauchamp RD, Shyr Y, Kirkland SC, Coffey RJ, Morrow JD. Antioxidants reduce cyclooxygenase-2 expression, prostaglandin production, and proliferation in colorectal cancer cells. Cancer Res. 1998;58:2323–2327.

41. Sharma R, Vinayak M. Antioxidant alpha-tocopherol checks lymphoma promotion via regulation of expression of protein kinase C-alpha and c-Myc genes and glycolytic metabolism. Leuk Lymphoma. 2012;53:1203–1210.

42. Tabatabaie T, Graham KL, Vasquez AM, Floyd RA, Kotake Y. Inhibition of the cytokine-mediated inducible nitric oxide synthase expression in rat insulinoma cells by phenyl N-tert-butylnitrone. Nitric Oxide. 2000;4:157–167.

43. Cobbs CS, Brenman JE, Aldape KD, Bredt DS, Israel MA. Expression of nitric oxide synthase in human central nervous system tumors. Cancer Res. 1995;55:727–730.

44. Pogrebniak HW, Merino MJ, Hahn SM, Mitchell JB, Pass HI. Spin trap salvage from endotoxemia: The role of cytokine down-regulation. Surgery. 1992;112:130–139.

45. Xie QW, Whisnant R, Nathan C. Promoter of the mouse gene encoding calciumin-dependent nitric oxide synthase confers inducibility by interferon gamma and bacterial lipopolysaccharide. J. Exp. Med. 1993;177:1779–1784

CHAPTER III

OKN-007 decreases VEGRF-2 levels in a preclinical GL261 mouse glioma model

3.1 INTRODUCTION

Angiogenesis, the formation of new blood vessels from preexisting vasculature, is a hallmark of cancer which plays pivotal roles in tumor development and metastasis [1-3]. Non-invasive and quantitative imaging of tumor angiogenesis is critical for lesion detection, patient stratification, and monitoring the therapeutic response of cancer patients, including brain tumors [4-5].

Physiological angiogenesis is tightly regulated by pro-endothelial and anti-endothelial growth factors (i.e. endogenous inhibitors) and occurs by a series of complex and interrelated steps [2, 6-7]. One of the most potent proangiogenic agents is the well-characterized vascular endothelial growth factor (VEGF) [7]. VEGF acts on vascular endothelial cells through compatible receptor tyrosine kinases VEGF receptor (VEGFR)-1, -2, and -3 [7]. VEGFR-1 is required for the recruitment of haematopoietic stem cells and the migration of monocytes and macrophages, VEGFR-2 regulates vascular endothelial function, and VEGFR-3 regulates lymphatic endothelial cell function [7]. In addition, VEGFR1 and VEGFR2 are highly expressed in different types of cancers such as gliomas [8].

Of the many different types of gliomas, glioblastoma (GBM) is the most common, accounting for about 40% of all primary brain tumors [9]. GBM is also one of the most vascular [10] and deadly cancers, with a very low 5-year survival rate of 6% [11].

A number of studies have shown that overexpression of VEGF and/or VEGFRs correlated with poor prognosis in multiple cancer types, including gliomas [12]. Furthermore, it has been also reported that intra-tumoral levels of VEGF and VEGFRs correlate with the histological grade of gliomas [13]. Knowing the dynamic distribution of VEGFRs, especially VEGFR-2, will lead to better understanding of the mechanisms underlying tumor angiogenesis, as well as provide a better tool for cancer diagnosis and treatment [14-15].

Recently, our group used molecular magnetic resonance imaging (mMRI) to evaluate the heterogeneous expression of VEGFR-2 in C6 and RG2 rat glioma models, using a specific VEGFR-2 contrast agent [16]. The study indicated that the C6 glioma likely have more active angiogenesis occurring in the relatively large vessels within the tumor periphery, whereas the RG2 glioma may have increased angiogenesis in the microcapillaries within the tumor interior [16].

Currently, antiangiogenic agents are routinely used for the treatment of patients with gliomas [17]. However, despite advances in pharmacological and surgical therapy, gliomas remain an incurable disease [17], highlighting the need for new treatment approaches.

OKN-007 (2, 4-disulfophenyl-PBN; or disodium 4-[(tert-butyl-imino) methyl] benzene-1,3-disulfonate N-oxide or disufenton; also previously known as NXY-059) is a very effective compound against *in vivo* adult glioma models [18-20], and it is currently undergoing clinical trial assessment as a new investigational drug for recurrent adult GBMs. OKN-007 is a small molecule that can traverse the blood-brain barrier and has also anti-inflammatory, antioxidant, proapoptotic [21-22], and anti-angiogenic properties [19-20].

In this study, we combined mMRI with an anti-VEGFR-2 gadolinium-based contrast agent to detect *in vivo* VEGFR-2 levels in untreated and OKN-007 treated adult GL261 mouse glioma models. Verification of the presence of the probe in tumor tissues and in glioma cell membranes through immunofluorescence and electron immunomicroscopy are also presented.

3.2 MATERIAL AND METHODS

3.2.1 Intracerebral glioma cell implantation

All animal studies were conducted with the approval of the Oklahoma Medical Research Foundation Institutional Animal Care and Use Committee. As a model for orthotopic intracranial brain tumors, a GL261 mouse glioma model was used (n = 17). GL261 mouse glioma cells were implanted intracerebrally in C57BL6/J mice. The heads of anesthetized mice were immobilized (stereotaxic unit; Kopf Instruments, Tujunga, CA), and with aseptic techniques, a 1 mm burr hole was drilled in the skull 1 mm anterior and 2 mm lateral to the bregma on the left side. A 20 μL gas-tight Hamilton syringe was used to inject 2×10^4 GL261 cells (in 10 μL of PBS) into the left frontal lobe at a depth of 1.5 mm relative to the dural surface in a stereotaxic unit. The cell lines were maintained and expanded immediately prior to inoculation. Following injection, the skin was closed with surgical sutures.

3.2.2 OKN-007 treatment

OKN-007 (2, 4-disulfophenyl-N-tert-butyl nitrone, Ryss Laboratories, Union City, CA) was administered to the mice in their drinking water at a concentration of 150 mg/kg/day (0.20% w/v for a 20g mouse). The treatment started at 13-15 days after glioma cell implantation, when the tumor volumes were between 10 and 15 mm^3. The treatment was administered continuously until the end of the study. Mice receiving normal drinking water were used as UT controls. The amount of OKN-007 consumed by each mouse, which were housed in separate cages, was determined by weighing water bottles each day. No significant deviation was observed in the volume of liquid uptake of compound in these mice. The average intake of OKN-007 was approximately 140-150 mg/kg/day. Mortality was recorded daily along the study period to calculate the percentage survival of all animals.

3.2.3 Synthesis of anti-VEGFR-2 MRI contrast agent

The contrast agent, biotin-BSA (bovine serum albumin)-Gd-DTPA, was prepared as previously described by our group [23], based on the modification of the method developed by Dafni *et al*. [24]. The estimated molecular weight for the biotin-albumin-Gd-DTPA moiety is ~80 kDa. It is estimated that there are 1.3 biotin and 23 Gd-DTPA groups bound to each BSA molecule. Briefly, anti-VEGFR-2 mAb (Santa Cruz Biotech, Inc., CA, USA) was conjugated to the albumin moiety through a sulfo-NHS (N-succinimidyl-S-acetylthioacetate)–EDC (N-succinimidyl 3-(2-pyridyldithio)-propionate) link according to the protocol of Hermanson [25]. Each animal was injected with 200 μl anti-VEGFR-2-BSA-Gd-DTPA-biotin (VEGFR-2 probe) [16, 26-27] intravenously via the tail vein with an amount estimated to be 200 μg anti-VEGFR-2 and 100 mg biotin-BSA-Gd-DTPA per injection. The estimated molecular weight of the VEGFR-2 probe is 232 kDa. For the immunoelectronmicroscopy study, an IgG contrast agent was used for a non-specific isotype control [16, 27].

3.2.4 Magnetic resonance techniques

3.2.4.1 Morphological imaging

Nude mice were anesthetized and positioned in a stereotaxic cradle. A 30-cm horizontal bore Bruker Biospin magnet operating at 7 Tesla (T; Bruker BioSpin GmbH, Karlsruhe, Germany), was used with a S116 gradient set to perform all MRI experiments. A mouse head coil was used for signal detection and a 72 mm quadrature volume coil for transmission. Multiple-slice, multiple echo (MSME) imaging (FOV= 2.50 x 2.50 cm^2, TR = 2000 ms, TE = 17.5 or 58.2 ms, matrix = 192, averages = 2, slices = 16, slice thickness = 1 mm) was used to calculate tumor volumes and to inspect tumor morphology. Starting ten days after the GL261 tumor cells inoculation, each mouse brain was imaged *in vivo* every 2-3 days until the end of the study.

3.2.4.2 Molecular MRI

Molecular MRI was performed when the tumors volume were close to their maximum tumor volumes (120-180 mm^3). A variable-TR RARE sequence (rapid acquisition with refocused echoes, with multiple TRs of 200, 400, 800, 1200 and 1600 ms, TE of 15 ms, FOV of 3.5×3.5 cm_2, matrix size of 256×256 and a spatial resolution of 0.137 mm) was used to obtain T_1-weighted images before and after administration of probe or control contrast agents.

3.2.4.3 Calculation of relative probe concentration

Relative probe (contrast agent) concentrations were calculated to assess the levels of VEGFR-2 in each animal. A contrast difference image was created from the pre- and (120 minutes) postcontrast datasets for the slice of interest, by computing the difference in signal intensity between the post-contrast and the pre-contrast image on a pixel basis. From a difference image, ten regions of interest (ROI) of equal size (0.05cm^2) were drawn within areas with the highest T_1 relaxation in the tumor parenchyma and contralateral side of the brain for each animal after the VEGFR-2 probe injection at the TR 800 ms. The values obtained from the ROIs in the tumor regions were normalized to the corresponding contralateral sides. The T_1 relaxation value of the specified ROIs was computed from all the pixels in the ROI by the following equation [28] (processed by ParaVision 4.0, Bruker): $S(TR) = S_0(1 - e^{-TR/T1})$, where TR is the repetition time, S_0 is the signal intensity (integer machine units) at $TR \gg T_1$ and TE = 0, and T_1 is the constant of the longitudinal relaxation time. An overlay of the contrast difference image and T_1-weighted image was generated using the 3D Analysis Software for Life Sciences Amira® (Fei, Hillsboro, Oregon).

3.2.5 Fluorescence staining

The whole brain of each rat from each treatment group was removed and fixed in 4% paraformaldehyde solution in phosphate buffered saline, then embedded in Optimal Cutting Temperature (OCT) compound and frozen in liquid nitrogen. Frozen tissue blocks were sectioned at 10 μm, mounted on positive-charged slides, and air-dried for 30 minutes. The tissue samples were permeabilized with 0.01% saponin in PBS (PBS/SAP) (10 minutes at 20°C) and incubated in a mixture of 3% bovine serum albumin and 5% normal donkey serum (host animal of the conjugated detection antibody) in PBS/SAP (1 hour at 20°C). Saponin was kept in all incubation buffers throughout the staining procedure, to ensure a proper penetration of the antibodies. Saponin exclusively removes cholesterol molecules from lipid-containing structures, leaving stable holes large enough for penetration of antibodies.

Next, the tissue sections were incubated with anti-CD31 antibody (BD Pharmingen Purified Rat anti-mouse CD31, catalog number: 550274) overnight at 4°C. The samples were washed 3 × 10 minutes in PBS/SAP, and incubated for 1 hour at 20°C with combinations of appropriate detection antibodies conjugated with fluorescein isothiocyanate and Cy_3 diluted 1:100 in 1% bovine serum albumin in PBS/SAP. After washing as above, the sections were mounted between glass slides and coverslips using Vectashield hardset mounting medium (Vector Laboratories, Burlingame, CA) containing TO-PRO-3 iodine (Molecular Probes, Eugene, OR) as nuclear counterstain.

As negative controls for polyclonal antibody staining, the primary antibodies were replaced with equivalent amounts of rat nonimmune serum. Specimens were examined by epifluorescence confocal imaging using a Nikon C1 confocal laser-scanning unit equipped with a three-laser launcher (488, 543, and 633 nm emission lines) installed on an Eclipse TE200-U inverted microscope (Nikon, Melville, NY). Images were taken with a ×20 plan achromat objective (NA 0.46). Image collection parameters (neutral density filters, pinhole, and detector gains) were kept constant during image acquisition, to make reliable semiquantitative comparisons between the linear and branched regions of the arteries.

3.2.6 Gold labeling immunoelectron microscopy

Brain tissue was obtained from GL261 glioma bearing mice that were administered either VEGFR-2 probe or a non-specific IgG contrast agent with gadolinium(Gd)-DTPA(diethylene triamine penta acetic acid)-albumin construct. Tissues were removed and cut to size of about 2cm and 3-5mm thick then fixed in 4% paraformaldehyde + 0.1% glutaraldehyde in 0.1M phosphate buffer (PB) for 1 hour at room temperature or at 4°C, washed thoroughly with with PB (pH 7.3). Tissue was trimmed further to 1-2mm pieces. Osmication was omitted for labelling procedure. Dehydration was in an ethanol series (50%, 70%, 80%, at 15 min each). Tissue was placed in 2:1 LR White resin (Electron Microscopy Sciences, PA) to 70% ethanol for 1 hour to avoid tissue shrinkage, and then further infiltrated in 100% LR White for 1 hour, overnight, and then two changes for 30 minutes. Tissue was added to gelatin capsules and LR White polymerized at 50°C for 24 hours. Gold-silver sections were placed on nickel grids coated with formvar or colloidin. Sections on grids were protein blocked in Aurion goat gold conjugate (Electron

Microscopy Sciences, PA) for 30 minutes, washed in PBS-0.2% bovine serum albumin 3x for 5 minutes at pH 7.4 (Electron Microscopy Sciences, PA). Aurion ultra small gold conjugate – goat anti-Biotin (Electron Microscopy Sciences, PA) in PBS-0.2% BSA-c was applied at 1:100 for overnight at 4°C or for 4 hours at room temperature. Grids were washed in PBS-0.2% BSA-c (pH 7.4), 6x for 5minutes; in PBS, 3x for 5 minutes; in distilled water 5x for 2 minutes. Silver enhancement was done by placing grids on a droplet of Aurion R-Gent SE-EM enhancement mixture (Electron Microscopy Sciences, PA) for 90 minutes, then washed in distilled water. Controls involved sections with no secondary antibody (anti-Biotin) and no silver enhancement. Sections were stained with uranyl acetate for 15 minutes followed by lead citrate for 3 minutes. Sections were viewed with a Zeiss T109 electron microscope operated at 80kV and equipped with a Gatan digital camera and micrograph acquisition software.

3.2.8 Statistical analysis

Statistical analyses were performed using the Graph Pad Prism 6 (GraphPad Prism 6 Software, San Diego, CA, USA). Tumor volumes and the VEGRF-2 levels were reported as the mean ± standard deviation. Student t-tests (independent-samples, two-tailed t-test) were used to assess the differences between means of untreated and OKN-007 treated GL261 glioma mice. For statistical analysis, Kaplan-Meier survival curves and Log-rank (mantel-cox) test were used to compare the survival times among the untreated and OKN-007 treated groups. All *p* values <0.05 were considered statistically significant.

3.3 RESULTS

Starting ten days after the GL261 tumor cell inoculations, all animals from each group were imaged *in vivo* every 2-3 days until the end of the study. The tumor volumes of ONK-007-treated animals were significantly smaller (p = 0.0054; 32.95 ± 7.130, n=4) than the untreated group (103.0 ± 16.96, n=7) at day 21 after tumor cell injection (Fig 3.1A-C).

For the entire study, animal survival was assessed by comparing OKN-007–treated animals with untreated animals. OKN-007-treated mice were found to survive significantly longer (p = 0.0005; median survival = 30 days; n = 7), compared with untreated animals (median survival = 22 days; n = 10) (Fig 3.1D).

Representative examples of images obtained in GL261 glioma-bearing mice are shown in Fig. 3.2. T_2-weighted and T_1-weighted morphological images obtained before injection of the VEGFR-2 probe are shown in Fig 3.2A and Fig. 3.2B respectively. A difference image, which is the subtraction between the T_1 images of pre- and 2 hrs after injection of the contrast agent, shows increased anti-VEGFR-2 probe accumulation in Fig. 3.2C, along with representative ROIs in the tumor and contralateral (normal) brain regions.

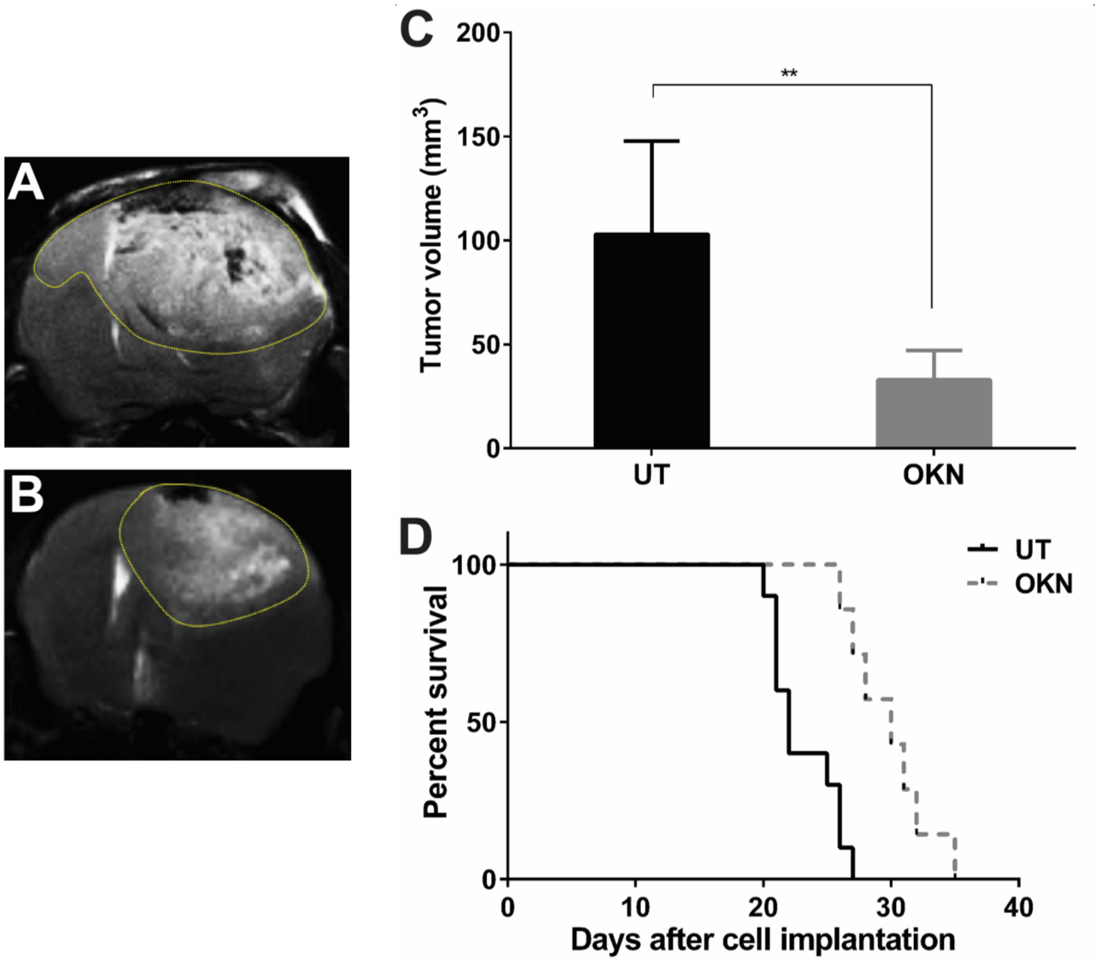

Figure 3.1. Effect of OKN-007 on tumor volumes and survival for GL261 tumor bearing mice. Representative T_2-weighted MR images of UT (A) and OKN-007 (B) treated GL261 gliomas. (C) The OKN-007-treated animals demonstrated significantly smaller tumors (p = 0.0054) when compared with UT animals. (D) The OKN-007-treated animals demonstrated significantly longer survival times (p = 0.0005, median survival = 30) when compared with UT animals (median survival = 22). Values are represented as means ± SD. Asterisks indicate statistically significant differences (**$p < 0.01$). UT: untreated animals.

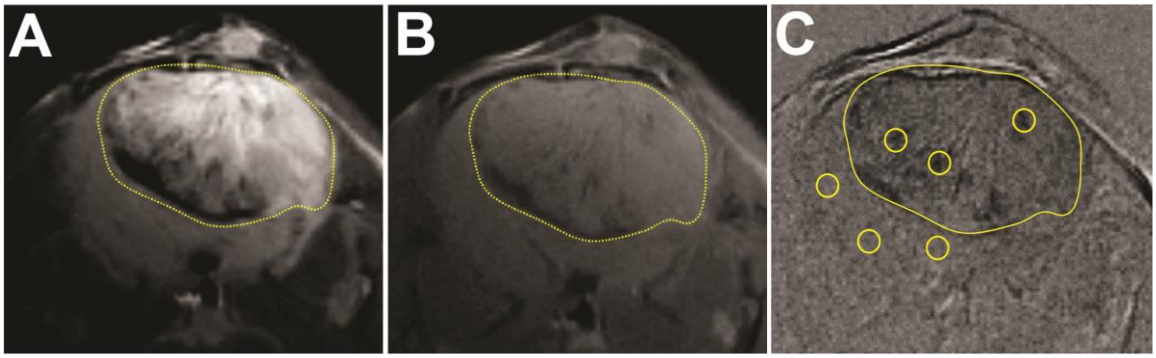

Figure 3.2. Morphological MR images obtained before and 2 hrs after injection of anti-VEGFR-2 probe (contrast agent) in a F98 rat glioma moldel. Representative T_2-weighted (A) and T_1-weighted image (B) before injection of the VEGFR-2 probe. (C) Representative difference image, which is the subtraction between the T_1 images of pre- and 2 hrs after injection of the contrast agent. The dark regions in the tumor depict areas of increased uptake of the anti-VEGFR-2 probe. Representative ROIs in the tumor and contralateral side of the brain are illustrated as circles in each region. The tumor is delineated by a dotted line in each panel.

There were differences in the levels of VEGFR-2 detected in the two different treatment groups. OKN-007 was found to significantly decrease (p = 0.04137) the levels of VEGFR-2 detected in the treated group (2.54 ± 2.02) compared to the untreated animals (10.12 ± 2.25) (Fig 3.3).

The fluorescence agent Cy3 (red) attached to streptavidin targets the biotin moiety of the anti-VEGFR-2 probe that is present in *ex vivo* excised tumor tissue from a GL261 glioma-bearing mouse administered the anti- VEGFR-2 probe *in vivo*. Co-localization (represented as yellow-orange regions) of the anti- VEGFR-2 probe (red) with the endothelial cell marker CD31 (green) was observed in some areas of glioma tissue from GL261 glioma-bearing mice administered the anti-VEGFR-2 probe(Fig 3.4).

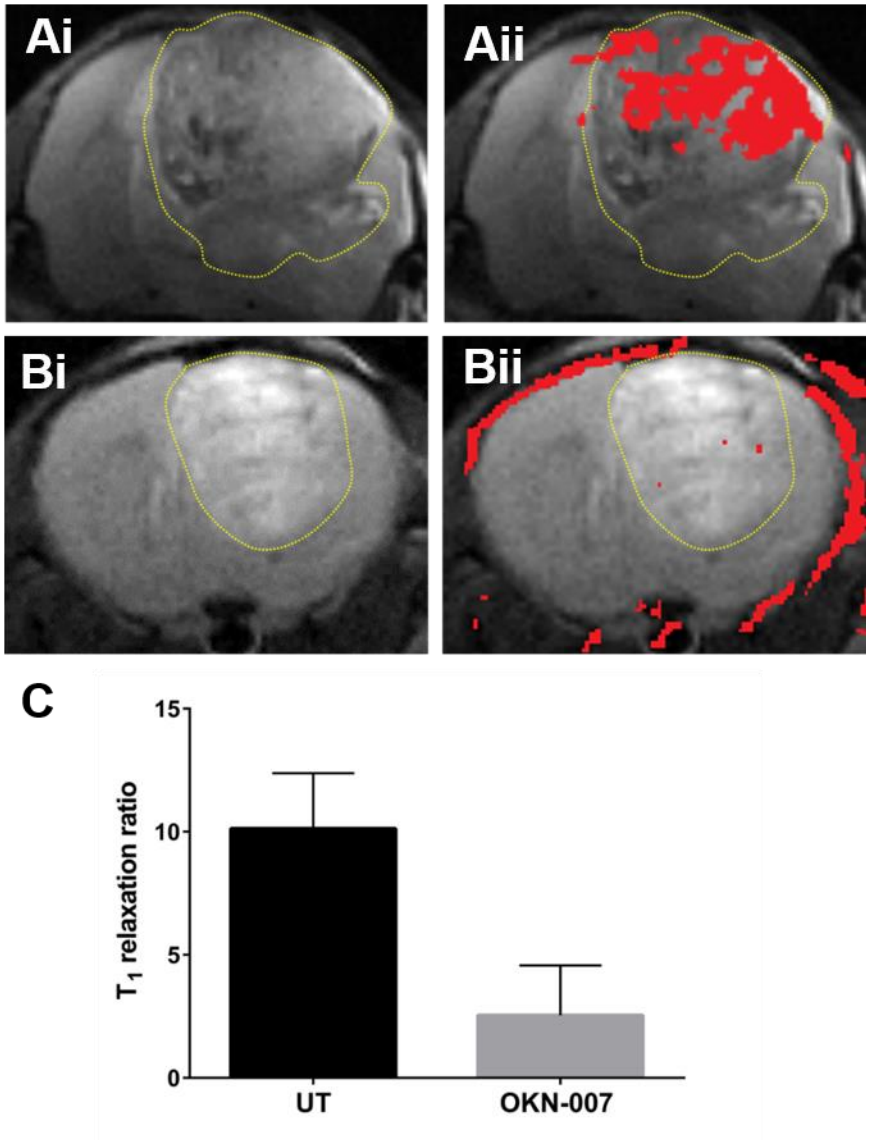

Figure 3.3. mMRI detection of VEGFR-2 in a GL261 mouse glioma model. Representative MR images from: (A) Untreated and (B) OKN-007 treated GL261 mouse gliomas. (Ai-Bi) T_2-weighted images of GL261 glioma. (Aii-Bii) T_2-weighted images overlayed with a difference T_1-weighted image (red), which was the subtraction between the 2 hr post-contrast and the pre-contrast images after injection of either the anti-VEGFR-2 probe contrast agent. Overlays of the contrast difference images and the T_2-weighet images were generated using the 3D Analysis Software for Life Sciences Amira®. (C) OKN-007 was found to significantly decrease (p = 0.4137) (2.54 ± 2.02) the levels of VEGFR-2 in the treated group compared to the untreated animals (10.12 ± 2.25). Values are represented as means ± SD. Asterisks indicate statistically significant differences (*p < 0.05). UT: untreated animals.

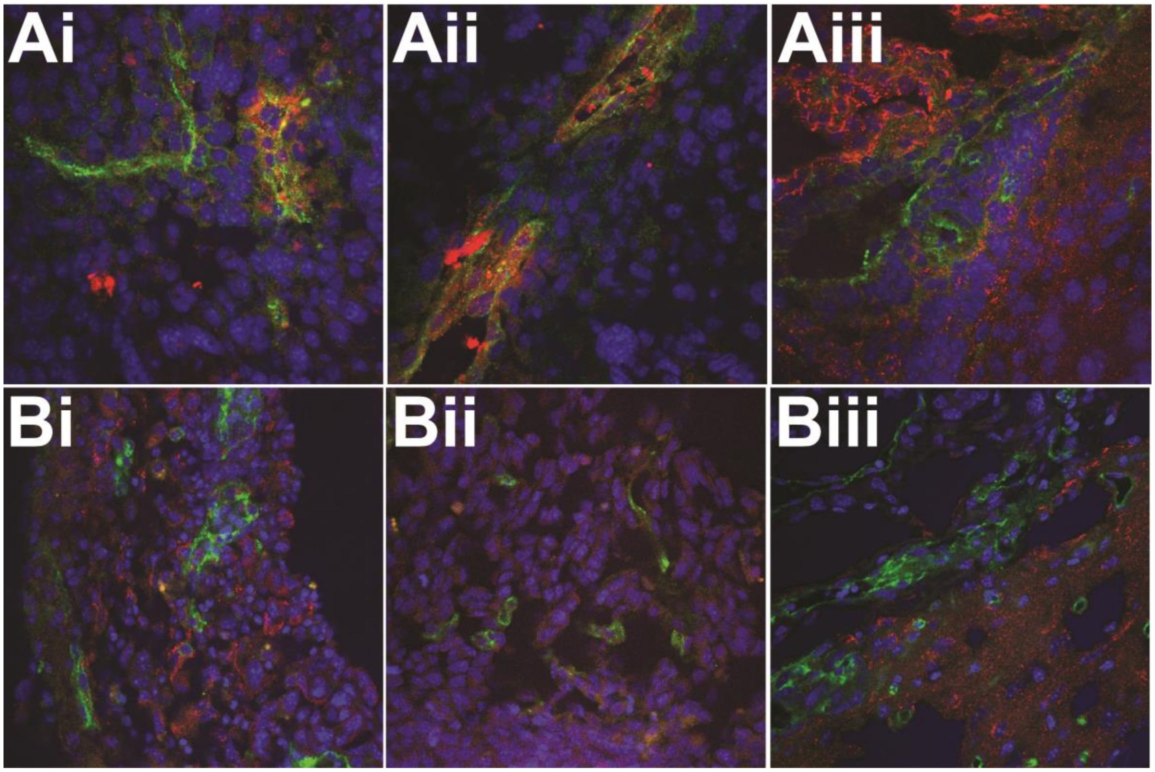

Figure 3.4. ***Ex vivo*** **detection of the anti-VEGFR-2 probe and colocalization with endothelial cell marker CD31 in untreated and OKN-007-treated GL261 mouse gliomas.** Fluorescence images of the anti-VEGFR-2 probe (red) and the endothelial marker CD31 (green) in untreated (Ai-Aiii) GL261 tumor-bearing animals and OKN-007-treated (Bi-Biii) GL261 tumor-bearing animals. Note colocalization (yellow-orange) of the anti- VEGFR-2 probe with some endothelial cells in the untreated group.

Ex vivo immunoelectron microscopy of GL261 mouse glioma tissues after post-embedding incubation with gold-labeled anti-biotin antibody was performed to determine the sub-cellular localization of the anti-VEGFR-2 probe (Fig 3.5). The gold-labeled anti-biotin was found to be distributed within the endothelial cell and glioma cell plasma membrane/cytoplasm, as well as the nuclei of the GL261 tumor cells in mice administered the anti- VEGFR-2 *in vivo* (Fig 3.5A). A control was found to only have uptake of the gold-anti-biotin in the endothelial cell nucleus (Fig. 3.5B).

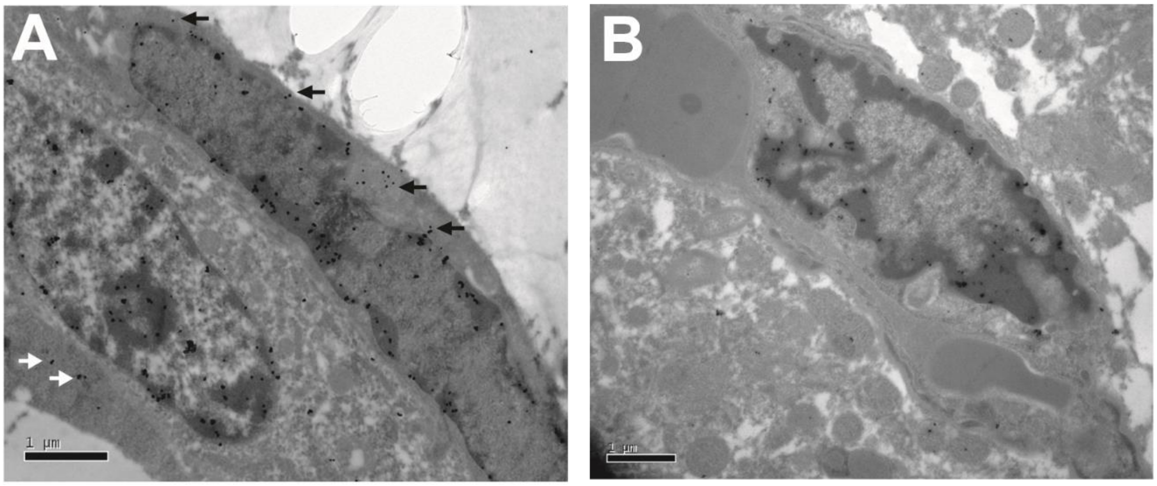

Figure 3.5. Electron immunomicroscopy detection of the anti-VEGFR-2 probe in the endothelial plasma membrane/cytoplasm and cell nuclei within GL261 rat gliomas. (A) Electron immunomicroscopy of a GL261 glioma-bearing mouse administered the anti-VEGFR2 probe. The biotin moiety of the anti-VEGFR-2 probe was targeted with gold-anti-biotin. Note uptake of the gold-anti-biotin in the endothelial plasma membrane/cytoplasm (black arrows) and the glioma cell plasma membrane/cytoplasm (white arrows). Also note increased gold-anti-biotin in the endothelial and glioma cell nuclei. (B) GL261 glioma-bearing mouse administered the non-specific IgG-albumin-Gd-DTPA-biotin probe (Control). Note some uptake of the gold-anti-biotin in the endothelial cell nucleus. Scale bar = 1μm. Magnification = 20,000×.

3.4 DISCUSSION

Angiogenesis, the formation of new blood vessels, is a critical step during tumorigenesis and represents a pathological hallmark of cancer [1], and plays a crucial role in glioma development and growth [29].

Briefly, the start of the angiogenesis process requires some exogenous angiogenic stimulus, such as hypoxia, current metabolic requirements, and tumor growth. More than 25 different growth factors and cytokines related to the induction of angiogenesis have been reported [30]. The production of these proangiogenic factors is a result of genetic alterations or is induced by hypoxia. Intratumor hypoxia occurs at the time when there is an imbalance between oxygen supply and demand, due to irregular and chaotic blood flow [31].

Furthermore, when a solid tumor, such as a brain tumor, grows larger than a critical size (1-2mm in diameter), it must recruit new blood vessels to supply the required oxygen and nutrition levels necessary for its survival and proliferation [17, 32]. This process comprises the formation of new blood vessels from preexisting ones, and is a crucial step in the progression of cancer from a small and localized neoplasm to a highly aggressive tumor [17]. Additional details about the angiogenesis process in gliomas can be found in a number of outstanding review articles [17, 29, 33-35].

Gliomas are highly vascularized tumors [35]. Furthermore, the formation of abnormal tumor vasculature and glioma cell invasion along white matter tracts are proposed to be the major causes of the therapeutic resistance of these tumors [17]. Thus, inhibition of angiogenesis has emerged as a promising strategy for the treatment of brain cancers.

In this study, we demonstrated through conventional and molecular MRI that OKN-007 inhibited the tumor levels of VEGFR-2, tumor growth, and increased survival time in treated GL261 mouse gliomas when compared to the untreated group.

Our group has already established that OKN-007 is an effective anti-cancer agent in rodent pre-clinical models for adult GBMs, including F98 [19], U87 [19], and C6 [18, 20] glioma models. Furthermore, in an orthotopic rat F98 glioma model and a human U87 xenograft model in athymic rats, OKN-007 significantly increased the survival of treated versus untreated rats [20]. Similarly to our previous studies, OKN-007 was also able to decrease the tumor volumes in the GL261 mouse glioma model. In the present study, the tumor volumes of OKN-007-treated GL261 gliomas were significantly smaller (p = 0.0054) when compared to the untreated group (Fig 3.1C).

The survival time of GL261-tumor bearing mice was also significantly increased after OKN-007 therapy, as we also have previously reported in other adult glioma models [19-20]. The OKN-

007-treated group (n = 7) had a median survival of 30 days, which was significantly longer (p = 0.0005) than the median survival of 22 days for the untreated group (n = 10) (Fig. 3.1D). OKN-007 was able to increase the survival time by 8 days in the treated group compared to the untreated animals. Considering that one mouse month is equivalent to ∼2.6 human years, based on a 4-year maximum life span [36], OKN-007 could potentially increase survival time in adult GBM patients by ~7-8 months.

There are several methods that have been used to monitor the levels of VEGFR-2 *in vitro* and *in vivo*. Recently, our group reported the *in vivo* characterization and distribution of VEGFR-2 in C6 [16, 27] and RG2 [16] glioma models using molecular magnetic resonance imaging (mMRI) and an anti-VEGFR-2 gadolinium-based contrast agent. MRI signal enhancement of the VEGFR-2 probe in the RG2 tumor interior was more than twice that for the C6 tumor interior, suggesting more VEGFR-2 from microvessels inside the RG2 tumor [16]. However, compared to C6 gliomas, RG2 gliomas have a relatively more homogeneous pattern for VEGFR-2 levels in the tumor overall [16]. In the C6 glioma, distinctively higher levels of VEGFR-2 were found in peri-tumor and peri-necrotic regions compared to tumor interior regions [27].

It was also previously demonstrated *in vivo* that OKN-007 is an effective anti-angiogenic compound, for decreasing the microvessel density and HIF-1α levels in both F98 and U87 glioma models [19] and the levels of VEGFR-2, as determined from Western blots, in C6 rat gliomas [20]. In the present study we confirmed using the mMRI technique, that OKN-007 was also able to decrease the levels of VEGFR-2 in a preclinical GL261 mouse glioma model (Fig 3.3).

Specifically, we combined mMRI with a Gd-DTPA-albumin-based contrast agent for signal detection with the specificity of an antibody for VEGFR-2 (anti-VEGFR2 probe), to detect *in vivo* VEGFR-2 levels in untreated and OKN-007 treated adult GL261 mouse gliomas. To calculate the T_1 relaxation, we normalized the T_1 relaxation values from the tumor area to the contralateral side of the brain in each animal datasets. We used the contralateral side of the brain to normalize the T_1 relaxation values of the tumor region as we detected no significant difference (p = 0.1824) in the T_1 relaxation values in the two treatment groups, 120 minutes after the administration of the anti-VEGFR-2 probe.

We have already demonstrated with immunofluorescence that the anti-VEGFR-2 probe binds to the VEGFR-2 present on tumor cells and endothelial cells in a rat C6 glioma model [27]. In the present study in the mouse GL261 glioma model, the fluorescence staining at 2 hours post administration of the probe confirmed the distribution of VEGFR2 similarly to our previous study [27]. Furthermore, the probe showed localization with the endothelial marker CD31 (Fig 3.4A).

Here we additionally used immunoelectron microscopy to demonstrate the presence of the anti-VEGFR-2 probe in the cell membrane/cytoplasm and cell nuclei of the endothelial cells and GL261 glioma tumor cells (Fig. 3.5A). During this technique, anti-biotin-gold was used to bind specifically to the biotin group of the anti-VEGFR-2 probe. The IgG contrast agent, which also has a biotin moiety, was not detected at very high levels with the anti-biotin-gold in the plasma membrane/cytoplasm of endothelial or glioma cells. Likewise the level of nuclear staining was less for the IgG contrast agent administered sample in the endothelial and glioma cells (Fig. 3.5B). However, more nuclear staining was found in the endothelial and glioma cells administered the anti-VEGFR-2 probe. Due to the size of the anti-VEGFR-2 probe, we do not think that this probe could be taken up by the cell nuclei. There are three possible other reasons that could account for nuclear staining for biotin. It may be possible that the nuclear positive gold-staining could be caused by non-specific staining as a result of secondary labelling of biotin in newly replicated DNA [37-38], or endogenous biotin, which has widely been taken up in the cell nuclei [39], or biotin could have come from biodegradation of the anti- VEGFR-2 probe. As the control IgG contrast agent sample had little staining for biotin, we surmise that the biotin detected in the cell nuclei from the glioma sample administered the anti- VEGFR-2 probe was from biodegradation of the probe which had accumulated in the glioma cells of untreated tumors.

Figure 3.6 depicts the possible anti-angiogenic mechanism of action of OKN-007 in glioma models. We already know that OKN-007 decreases levels of VEGFR-2 [20] and HIF-1α [19] in rat gliomas, and that nitrones such as PBN (α-phenyl-tert-butyl nitrone) decrease NF-κB in a mouse endotoxemia model [40]. There is also evidence that OKN-007 effectively traps free radicals *in vitro* [41]. Consequently, based on the possible mechanisms-of-action and our data reported in this study, OKN-007 is an effective agent that can inhibit tumor angiogenesis.

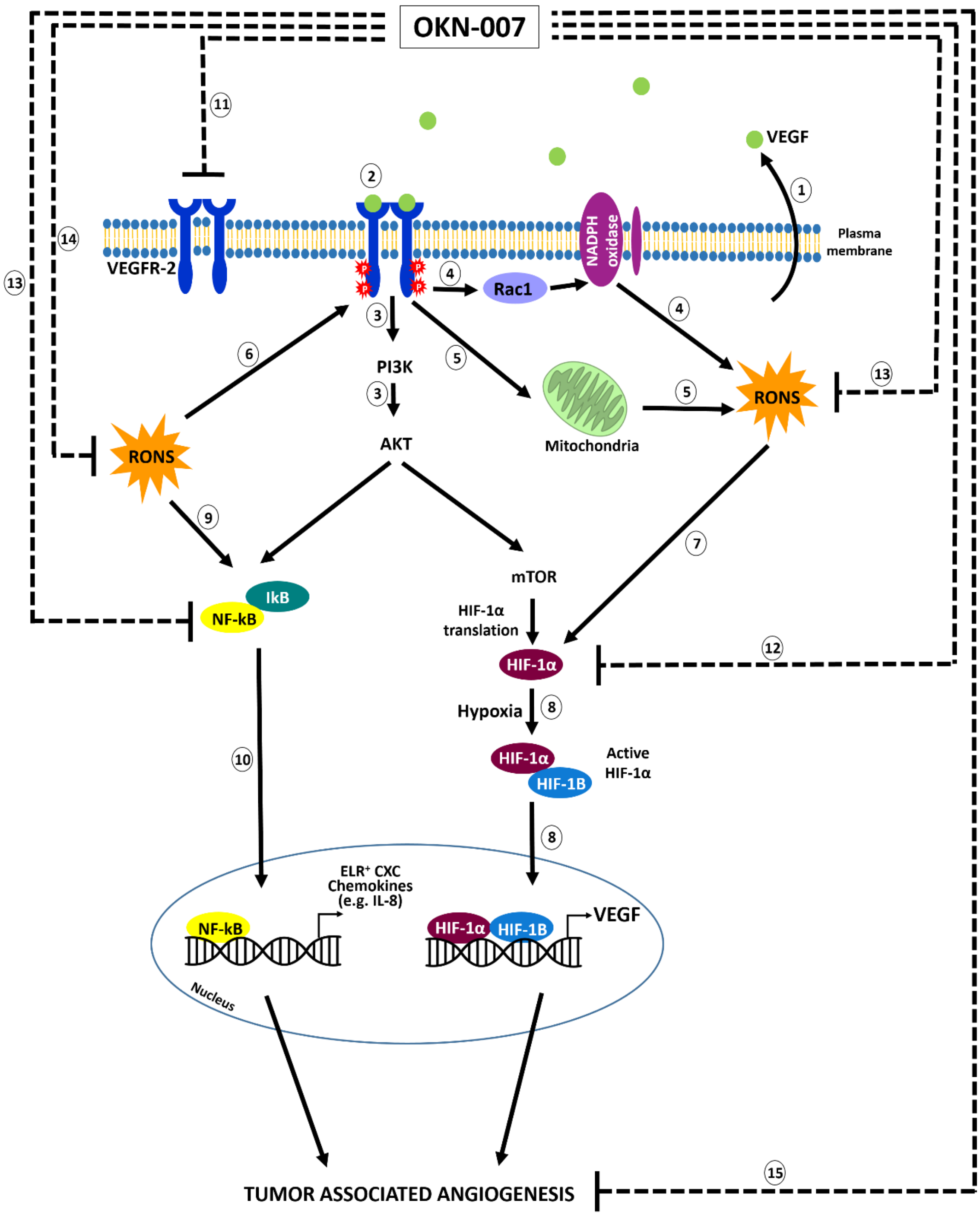
OKN-007
11
2
VEGF
1
14
13
VEGFR-2
Plasma membrane
NADPH oxidase
4
Rac1
4
3
PI3K
3
AKT
5
5
Mitochondria
6
RONS
13
RONS
9
7
mTOR
IkB
NF-kB
HIF-1α translation
HIF-1α
12
Hypoxia
8
10
HIF-1α
HIF-1B
Active HIF-1α
8
ELR⁺ CXC Chemokines (e.g. IL-8)
NF-kB
HIF-1α
HIF-1B
VEGF
Nucleus
15
TUMOR ASSOCIATED ANGIOGENESIS

Figure 3.6. Schematic representation of possible anti-angiogenic mechanisms of action for the anti-cancer agent OKN-007. (1) VEGF is ubiquitously expressed in almost all tumors. Glioma cells have been demonstrated to secrete VEGF, which leads to increased angiogenesis [42]. (2) VEGF exerts its action through binding to VEGFR-2, leading to autophosphorylation of tyrosine residues in the cytoplasmic domain of VEGFR-2 and driving downstream pathway such as PI3K/AKT and MAPK to promote endothelial cells proliferation and migration (3). VEGF also stimulates reactive oxygen and nitrogen species (RONS) production via Rac1-mediated NADPH oxidase activation (4) [43] and also increases mitochondria-derived hydrogen peroxide (H_2O_2) (5) [44]. (6) RONS, in turn, potentiate VEGFR phosphorylation [43]. RONS can also upregulate VEGF secretion and VEGFR expression through induction of transcription factors HIF-1α (hypoxia-inducible factor-1α) (7) [44-46]. (8) Under hypoxic conditions, the active HIF-1α recognizes and binds to *cis* elements in the promoter of genes that mediate angiogenesis, such as the gene encoding VEGF [47]. (9) NF-kB (nuclear factor of kappa light polypeptide gene enhancer in B-cell) is normally under strict regulation by its sequestration in the cytoplasm in association with a heterotrimeric complex of NF-kB with the inhibitor of kB (IkB) [47]. (10) Generation of reactive oxygen and nitrogen species (RONS) and activation of PI3 kinase–AKT pathway can converge and activate NF-kB. NF-kB also activates several genes that mediate angiogenesis, such ELR^+ CXC chemokines [47]. OKN-007 decreases levels of VEGFR-2 [20] (11) and HIF-1α [19] (12) in rat gliomas, and that nitrones such as PBN (α-phenyl-tert-butyl nitrone) decrease NF-κB (13) in a mouse endotoxemia model [40]. There is also evidence that OKN-007 effectively traps free radicals (14) *in vitro* [41]. Consequently, based on the possible mechanisms-of-action and our data reported in this study, OKN-007 is an effective agent that can inhibit tumor angiogenesis (15). The schematic is a modification of combined schemes obtained from Oxidative Medicine and Cellular Longevity, Article ID 374963, Zhou Y et al. (2013) [Copyright (2013) with permission from Hindawi Publishing Corporation] [48], and from Nature Medicine, 11(9):925-7, Strieter RM. (2005) [Copyright (2005) with permission from Nature Publishing Group] [47].

3.5 CONCLUSION

This is the first attempt at detecting *in vivo* levels of VEGFR-2 in a mouse GL261 glioma model and assessing the anti-angiogenic capability of an anticancer nitrone. Our study confirmed that *in vivo* VEGFR2 levels can be monitored and can be used to assess the efficacy of an anti-angiogenic therapy.

This method can potentially be applied towards other types of cancers for the *in vivo* assessment of VEGFR-2 levels, and assess various anti-angiogenic agents. The results indicate that OKN-007 treatment substantially decreased VEGFR-2 levels in a GL261 glioma model, and can be considered as an anti-angiogenic therapy in human gliomas.

3.6 REFERENCES

1. Hanahan D, Weinberg RA. Hallmarks of cancer: the next generation. Cell. 2011; 144:646-74.

2. Bergers G, Benjamin LE. Tumorigenesis and the angiogenic switch. Nat Rev Cancer. 2003;3:401-10.

3. Folkman J. Angiogenesis in cancer, vascular, rheumatoid and other disease. Nat Med. 1995;1:27–31.

4. Price SJ, Gillard JH. Imaging biomarkers of brain tumour margin and tumour invasion. Br J Radiol. 2011;84 Spec No 2:S159–67.

5. Gagner JP, Law M, Fischer I, Newcomb EW, Zagzag D. Angiogenesis in gliomas: imaging and experimental therapeutics. Brain Pathol. 2005;15:342–363.

6. Gasparini G, Longo R, Toi M, Ferrara N. Angiogenic inhibitors: a new therapeutic strategy in oncology. Nat Clin Pract Oncol. 2005;2:562-77.

7. Hoeben A, Landuyt B, Highley MS, Wildiers H, Van Oosterom AT, De Bruijn EA. Vascular endothelial growth factor and angiogenesis. Pharmacol Rev. 2004;56:549-80.

8. Plate KH, Breier G, Weich HA, Risau W Vascular endothelial growth factor is a potential tumour angiogenesis factor in human gliomas in vivo. Nature. 1992;359:845-8.

9. CBTRUS Statistical Report: Primary Brain and Central Nervous System Tumors Diagnosed in the United States in 2004-2008. Central Brain Tumor Registry of the United States (CBTRUS) 2012.

10. Behin A, Hoang-Xuan K, Carpentier AF, Delattre JY. Primary brain tumours in adults. Lancet. 2003;361:323–331.

11. Johnson, D.R., Ma, D. J., Buckner, J. C., & Hammack, J. E. Conditional probability of long-term survival in glioblastoma. Cancer. 2012;118:5608-13.

12. Jain RK, di Tomaso E, Duda DG, Loeffler JS, Sorensen AG, Batchelor TT. Angiogenesis in brain tumours. Nat Rev Neurosci. 2007;8:610–622.

13. Samoto K, Ikezaki K, Ono M, Shono T, Kohno K, Kuwano M, Fukui M. Expression of vascular endothelial growth factor and its possible relation with neovascularization in human brain tumors. Cancer Res. 1995;55:1189-93.

14. Cai W, Chen X. Multimodality molecular imaging of tumor angiogenesis. J Nucl Med. 2008;49(Suppl 2):113S–128S.

15. Cai W, Chen X. Multimodality imaging of vascular endothelial growth factor and vascular endothelial growth factor receptor expression. Front Biosci. 2007;12:4267–4279.

16. He T, Smith N, Saunders D, Pittman BP, Lerner M, Lightfoot S, Silasi-Mansat R, Lupu F, Towner RA. Molecular MRI differentiation of VEGF receptor-2 levels in C6 and RG2 glioma models. Am J Nucl Med Mol Imaging. 2013;3:300-11.

17. Cea V, Sala C, Verpelli C. Antiangiogenic therapy for glioma. J Signal Transduct. 2012;2012:483040.

18. He T, Doblas S, Saunders D, Casteel R, Lerner M, Ritchey JW, Snider T, Floyd RA, Towner RA. Effects of PBN and OKN007 in rodent glioma models assessed by 1H MR spectroscopy. Free Radic Biol Med. 2011;51:490-502.

19. Towner RA, Gillespie DL, Schwager A, Saunders DG, Smith N, Njoku CE, Krysiak RS 3rd, Larabee C, Iqbal H, Floyd RA, Bourne DW, Abdullah O, Hsu EW, Jensen RL. Regression of glioma tumor growth in F98 and U87 rat glioma models by the Nitrone OKN-007. Neuro Oncol. 2013;15:330-40.

20. Garteiser P, Doblas S, Watanabe Y, Saunders D, Hoyle J, Lerner M, He T, Floyd RA, Towner RA. Multiparametric assessment of the anti-glioma properties of OKN007 by magnetic resonance imaging. J Magn Reson Imaging. 2010;31:796-806.

21. Floyd RA, Kopke RD, Choi CH, Foster SB, Doblas S, Towner RA. Nitrones as therapeutics. Free Radic Biol Med. 2008;45:1361-74.

22. Floyd RA, Chandru HK, He T, Towner R. Anti-cancer activity of nitrones and observations on mechanism of action. Anticancer Agents Med Chem. 2011;11:373-379.

23. Towner RA, Smith N, Asano Y, He T, Doblas S, Saunders D, Silasi-Mansat R, Lupu F, Seeney CE. Molecular magnetic resonance imaging approaches used to aid in the understanding of angiogenesis in vivo: implications for tissue engineering. Tissue Eng Part A. 2010;16:357-64.

24. Dafni H, Landsman L, Schechter B, Kohen F, Neeman M. MRI and fluorescence microscopy of the acute vascular response to VEGF165: vasodilation, hyper-permeability and lymphatic uptake, followed by rapid inactivation of the growth factor. NMR Biomed. 2002;15:120-31.

25. Hermanson, GT. Bioconjugate Techniques. San Diego: Academic, 1996.

26. Chen F, Zhang Y, Cai W. Molecular MRI of VEGFR-2 reveals intra-tumor and inter-tumor heterogeneity. Am J Nucl Med Mol Imaging. 2013;3:312-6.

27. He T, Smith N, Saunders D, Doblas S, Watanabe Y, Hoyle J, Silasi-Mansat R, Lupu F, Lerner M, Brackett DJ, Towner RA. Molecular MRI assessment of vascular endothelial growth factor receptor-2 in rat C6 gliomas. J Cell Mol Med. 2011;15:837-49.

28. Haacke, EM. Magnetic Resonance Imaging: Physical Principles and Sequence Design. New York, NY: Wiley-Liss, 1999.

29. Bello L, Giussani C, Carrabba G, Pluderi M, Costa F, Bikfalvi A. Angiogenesis and invasion in gliomas. Cancer Treat Res. 2004;117:263-84.

30. Wong ML, Prawira A, Kaye AH, Hovens CM. Tumour angiogenesis: its mechanism and therapeutic implications inmalignant gliomas. J Clin Neurosci. 2009;16:1119-30.

31. Jensen RL. Hypoxia in the tumorigenesis of gliomas and as a potential target for therapeutic measures. Neurosurg Focus. 2006;20:E24.

32. Zetter BR: Angiogenesis and tumor metastasis. Annu Rev Med. 1998, 49:407-424.

33. Bulnes S, Bengoetxea H, Ortuzar N, Argandoña EG, Garcia-Blanco A, Rico-Barrio I, Lafuente JV. Angiogenic signalling pathways altered in gliomas: selection mechanisms for more aggressive neoplastic subpopulations with invasive phenotype. J Signal Transduct. 2012;2012:597915.

34. Jain RK, di Tomaso E, Duda DG, Loeffler JS, Sorensen AG, Batchelor TT. Angiogenesis in brain tumours. Nat Rev Neurosci. 2007;8:610-22.

35. Plate KH1, Breier G, Weich HA, Mennel HD, Risau W. Vascular endothelial growth factor and glioma angiogenesis: coordinate induction ofVEGF receptors, distribution of VEGF protein and possible in vivo regulatorymechanisms. Int J Cancer. 1994;59:520-9.

36. Miller RA, Harper JM, Dysko RC, Durkee SJ, Austad SN. Longer life spans and delayed maturation in wild-derived mice. Exp Biol Med (Maywood). 2002;227:500-8.

37. Zempleni J. Uptake, localization, and noncarboxylase roles of biotin. Annu Rev Nutr. 2005;25:175-96.

38. Hiriyanna KT, Varkey J, Beer M, Benbow RM. Electron microscopic visualization of sites of nascent DNA synthesis by streptavidin-gold binding to biotinylated nucleotides incorporated in vivo. J Cell Biol. 1988;107:33-44.

39. Nikiel B, Chekan M, Jarzab M, Lange D. Endogenous avidin biotin activity (EABA) in thyroid pathology: immunohistochemical study. Thyroid Res. 2009;2:5.

40. Pogrebniak HW, Merino MJ, Hahn SM, Mitchell JB, Pass HI. Spin trap salvage from endotoxemia: The role of cytokine down-regulation. Surgery. 1992;112:130–139.

41. Williams HE, Claybourn M, Green AR. Investigating the free radical trapping ability of NXY-059, S-PBN and PBN. Free Radic Res. 2007;41:1047-52.

42. Yoshino Y, Aoyagi M, Tamaki M, Duan L, Morimoto T, Ohno K. Activation of p38 MAPK and/or JNK contributes to increased levels of VEGF secretion in human malignant glioma cells. Int J Oncol. 2006;29:981-7.

43 Ushio-Fukai M, Tang Y, Fukai T, Dikalov SI, Ma Y, Fujimoto M, Quinn MT, Pagano PJ, Johnson C, Alexander RW. Novel role of gp91(phox)-containing NAD(P)H oxidase in vascular endothelial growth factor-induced signaling and angiogenesis. Circ Res. 2002;91:1160-7.

44. Wang Y, Zang QS, Liu Z, Wu Q, Maass D, Dulan G, Shaul PW, Melito L, Frantz DE, Kilgore JA, Williams NS, Terada LS,Nwariaku FE. Regulation of VEGF-induced endothelial cell

migration by mitochondrial reactive oxygen species. Am J Physiol Cell Physiol. 2011;301:C695-704.

45. Arbiser JL, Petros J, Klafter R, Govindajaran B, McLaughlin ER, Brown LF, Cohen C, Moses M, Kilroy S, Arnold RS,Lambeth JD. Reactive oxygen generated by Nox1 triggers the angiogenic switch. Proc Natl Acad Sci U S A. 2002;99:715-20.

46. Xia C, Meng Q, Liu LZ, Rojanasakul Y, Wang XR, Jiang BH. Reactive oxygen species regulate angiogenesis and tumor growththrough vascular endothelial growth factor. Cancer Res. 2007;67:10823-30.

47. Strieter RM.Masters of angiogenesis. Nat Med. 2005;11:925-7.

48. Zhou Y, Yan H, Guo M, Zhu J, Xiao Q, Zhang L. Reactive Oxygen Species in Vascular Formation and Development. Oxid Med Cell Longev. 2013, Article ID 374963, 14 pages, 2013. Hindawi Publishing Corporation.

CHAPTER IV

Inhibition of pediatric glioblastoma tumor growth by the anti-cancer agent OKN-007 in orthotopic mouse xenografts

4.1 INTRODUCTION

High grade gliomas (HGG) represent one of the most common central nervous system (CNS) tumors among adults. This contrasts significantly to the pediatric population where HGGs only comprise approximately 8–12% of all primary CNS tumors [1]. These tumors are classified by the World Health Organization (WHO) as either grade III or IV meaning that they are highly malignant tumors with characteristic features such as hypercellularity, nuclear atypia, and high mitotic activity with or without microvascular proliferation and necrosis [2]. The most common pediatric HGGs include anaplastic astrocytoma (WHO grade III) and glioblastoma (GBM; WHO grade IV). Pediatric glioblastoma (pGBM) is one of the leading causes of cancer-related deaths in children [3] with a median overall survival for patients of 11 months [4]. Despite improvements in neurosurgery, radiotherapy, and chemotherapy, the outcome for children with pediatric HGG remains poor [5-6]. No effective chemotherapy regimens have yet been identified for any pediatric HGG [5]. Furthermore, novel molecularly targeted agents have demonstrated little efficacy in early phase clinical trials [7-9], highlighting the need for new treatment approaches.

Similarly, the improvement of *in vitro* and *in vivo* models for pediatric HGGs is also needed. Tumor cell lines and animal models derived from CNS tumors are essential tools to study the biology of the disease, to comprehend the mechanisms of resistance to therapy, and to carry out preclinical therapeutic testing. There is abundant information on animal models of adult HGG [10-13], including chemically induced, genetically engineered mice, and xenograft models [10]. However, to date only a few pediatric brain tumor models have been established and/or characterized [14-21].

We have shown that the anti-cancer agent OKN-007 (OKlahoma Nitrone-007; disodium 4-[(tert-butyl-imino) methyl] benzene-1,3-disulfonate N-oxide or disufenton) is very effective against adult gliomas in preclinical models [12,22-23], and it is currently undergoing clinical trial assessment as a new investigational drug for recurrent adult glioblastomas. OKN-007 is a small molecule that can traverse the blood-brain barrier and has anti-inflammatory, antioxidant, and proapoptotic properties [24-25]. In an orthotopic rat F98 glioma model and a human U87 xenograft model in athymic rats, OKN-007 significantly increased the survival of treated versus untreated rats [23]. Tumor volumes in both of these models were significantly decreased in treated compared to untreated animals based on magnetic resonance imaging (MRI) assessment [23].

MRI has been used in preclinical [14-15] and clinical [26-33] studies to diagnose and predict therapy outcomes for pediatric brain tumors. The techniques most commonly used include *in vivo* ^{1}H magnetic resonance spectroscopy (^{1}H-MRS) [34-36], diffusion-weighted imaging (DWI) [37-38], and arterial spin labeling perfusion (ASL) [39]. ^{1}H-MRS has been used in research and clinical settings to measure metabolite levels in the brain, and is well suited to perform the diagnosis, characterization, and assessment of tumor response to treatment [40]. DWI can qualitatively and quantitatively assess molecular motion on the basis of microstructural organization of tissues by characterizing water mobility [41], and can provide a more complete evaluation of cellular and metabolic information about human brain cancer [42]. ASL allows the assessment of measuring tumor blood flow [43], which assists in the characterization of tumor grade [39] and response to cancer therapy [44].

Here we describe the MRI characterization of a novel orthotopic xenograft pediatric HGG mouse (IC-3752GBM) model and the effects of OKN-007 to inhibit *in vivo* pediatric glioblastoma IC-3752GBM tumor growth using conventional (morphological imaging) and advanced MRI techniques (^{1}H-MRS, DWI, and ASL). Immunohistochemical staining was also used to evaluate the levels of tumor-related proteins and to assess tumor cell proliferation. To the best of our knowledge, the current study is the first report of MRI characterization of an orthotopic xenograft murine model of pGBM, and the assessment of the anti-cancer agent, OKN-007, in a pGBM model.

4.2 MATERIAL AND METHODS

4.2.1 Brain tumor specimen

A fresh tumor specimen (IC-3752GBM), from a 5-year-old female who underwent craniotomy at the Texas Children's Hospital, was obtained in a cryostat laboratory with signed consent following an Institutional Review Board-approved protocol. Final pathological diagnosis was consistent with pediatric glioblastoma (pGBM) [45]. The tumor sample was directly implanted into right cerebral cortex of immunedeficient mice. Xenograft tumor cells harvested from donor mice were passaged in nude mice via six subsequent implantations as we described previously [45-46] Institutional Animal Care and Use Committee approvals were obtained for the mouse xenograft tumor tissue implantations at the Texas Children’s Cancer Center.

4.2.2 Intracranial mouse brain tumor model

The animal studies were conducted with approval from the Institutional Animal Care and Use Committee of the Oklahoma Medical Research Foundation. The passaged pediatric glioblastoma cells IC-3752GBM were implanted intracerebrally in athymic nude mice (n= 19). The heads of anesthetized mice were immobilized (stereotaxic unit; Kopf Instruments, Tujunga, CA), and with aseptic techniques, a 1 mm burr hole was drilled in the skull 1 mm anterior and 2 mm lateral to the bregma on the left side. A 20 µL gas-tight Hamilton syringe was used to inject 5-10 × 10^6 IC-3752GBM cells/mL suspended in 4 µL in cell culture media with 1.0% agarose into the left frontal lobe at a depth of 1.5 mm relative to the dural surface in a stereotaxic unit. The cell lines were maintained and expanded immediately prior to inoculation. Following injection, the skin was closed with surgical sutures. The animals were divided into two groups: OKN-007–treated (n = 11) and untreated (n = 8) groups. Both groups were stratified to ensure that tumor sizes were similar before treatment started in the treated group.

4.2.3 OKN-007 treatment

OKN-007 (Ryss Laboratories, Union City, CA) was administered to the mice in their drinking water at a concentration of 150 mg/kg/day (0.20% w/v for a 20g mouse). The treatment started when the tumor volumes were between 10 and 15 mm^3, and was administered continuously until the end of the study. Mice receiving normal drinking water were used as untreated controls. The amount of OKN-007 consumed by each mouse, which were housed in separate cages, was determined by weighing water bottles each day. No significant deviation was observed in the volume of liquid uptake of compound in these mice. The average intake of OKN-007 was approximately 130-150 mg/kg/day. For the entire study, the therapeutic response to OKN-007 was evaluated as either responsive (OKN-007-R) or non-responsive (OKN-007-NR). Mortality was recorded daily during the study period to calculate the percentage survival of all animals.

4.2.4 Magnetic resonance techniques

4.2.4.1 Morphological imaging

Nude mice were anesthetized and positioned in a stereotaxic cradle. A 30-cm horizontal bore Bruker Biospin magnet operating at 7 Tesla (T; Bruker BioSpin GmbH, Karlsruhe, Germany), was used with a S116 gradient set to perform all MRI experiments. An EPI (echo planar imaging) transceiver ^{1}H 50W coil with a 38.0 mm inner diameter was used for signal transmission and detection. Multiple-slice, multiple echo (MSME) imaging (FOV= 2.50 x 2.50 cm^2, TR = 2000 ms, TE = 17.5 or 58.2 ms, matrix = 192, averages = 2, slices = 16, slice thickness = 1 mm) was used to calculate tumor volumes and to inspect tumor morphology. Multi slice spin echo T_1-weighted images (TR = 1000.0 ms, TE = 14 ms, FOV = 2.50 × 2.50 cm^2, averages=2, slices=16, matrix size = 256 × 256) were also performed and acquired before and 15 min after intravenous contrast agent injection (Gd-DTPA, Magnevist, Bayer Inc., Wayne, NY, USA; 0.4 mmol/kg).

4.2.4.2 ^{1}H-MR Spectroscopy

^{1}H-MRS was acquired using a PRESS (Point REsolved SpectroScopy) sequence with a TE of 24.0 ms, a TR of 2500.0 ms, 512 averages, and a spectral width of 4006 Hz. A non-suppressed MR spectrum was acquired beforehand by applying eddy-current correction to maximize signal intensity and decrease the peak linewidths. Water was suppressed with a VAPOR (variable power radio frequency pulses and optimized relaxation delays) suppression scheme. In all cases, the peak width (full width at half maximum) of the water peak was less than 30 Hz following localized shimming, which was conducted by using first and second order adjustments with Fastmap. A cubic voxel of 2.0 x 2.0 x 2.0 mm^3 was positioned in either the tumor or the contralateral normal brain tissue, while maximizing the amount of tumor tissue present in the voxel at all times.

To analyze the MRS data, an in-house Mathematica program was used (version 6.0, Wolfram Research, Champaign, IL, USA). The spectra were scaled in ppm by calibrating against the water peak (4.78 ppm). The major brain metabolic peaks were identified as: N-acetylaspartate (NAA) at 2.02 ppm, choline (Cho) at 3.22 ppm, creatine (Cre) at 3.02 ppm, and mobile lipids at 1.3 ppm (Lip1.3) for the methylene group ($-CH_2-$) and 0.9 ppm (Lip0.9) for the methyl group ($-CH_3$) in the tumor tissue. The peak area measurements of the metabolites were used to calculate the following ratios: tumor NAA to tumor Cho (NAA^t/Cho^t), tumor Cho to contralateral (normal tissue) Cre (Cho^t/Cre^n), tumor Cho to tumor NAA (Cho^t/NAA^t), tumor Lip0.9 to contralateral Cre ($Lip0.9^t/Cre^n$), and tumor Lip1.3 to contralateral Cre ($Lip1.3^t/Cre^n$).

4.2.4.3 Diffusion-Weighted Imaging

A coronal axial multi-slice DWI sequence covering the entire tumor was performed using an echo planar imaging–based pulse sequence with the following parameters: TR = 4000 ms, TE = 51.1 ms, matrix size = 128 × 128, slice thickness = 1mm, diffusion gradient duration = 4 ms, diffusion gradient separation = 14 ms. Five images were obtained with different gradient scalings, resulting in b-values of 100, 200, 500, 700, and 850 s/mm^{-2}. ADC maps were generated for all the slices in which the tumor was observed. The apparent diffusion coefficient (ADC) values were obtained by drawing a single freehand ROI along the border of the tumor normalized to the contralateral normal brain.

4.2.4.4 Arterial spin-labeling perfusion

Perfusion maps were obtained on a single axial slice of the brain located on the point of the rostro–caudal axis where the tumor had the largest cross-section. The imaging geometry was a 25.6 × 25.6 mm^2 field-of-view (FOV) of 2 mm in thickness, with a single shot echo-planar encoding over a 64 × 64 matrix. An echo time (TE) of 13.5 ms, a repetition time (TR) of 18 s, and an inversion time (TIR) of 26.0 ms were used, and images were not submitted to time averaging. To obtain perfusion contrast, the flow alternating inversion recovery scheme was used. Briefly, inversion recovery images were acquired using a slice-selective inversion of the same geometry as the imaging slice or a nonselective inversion slice concentric with the imaging slice with a slice package margin of 5.0 mm. For each type of inversion, 22 images were acquired with inversion times evenly spaced from 26.0 ms to 8,426.0 ms (with an increment of 400 ms between each TIR). CBV (cerebral blood flow) values were obtained by drawing a single freehand ROI along the border of the tumor normalized to the contralateral normal brain to obtain normalized relative CBF (rCBF) values. Negative ASL CBF values were assumed to be zero [47].

4.2.5 Gross and microscopic histology

Necropsies were performed on all mice. The extent of tumor at necropsy was evaluated by gross and microscopic examination of the brain for each animal from the untreated and OKN-007–treated groups. Brain tissues were fixed in 10% phosphate buffered formalin, embedded in paraffin, serially sectioned at 4 µm, and were stained with hematoxylin eosin (H&E) for histological examination.

4.2.6 Immunohistochemistry

Immunohistochemical staining was performed using an automated immunostainer (Leica, Bond-III, Leica, Buffalo Grove, IL) with the following primary polyclonal antibodies: platelet-derived growth factor receptor alpha (PDGFRα) (1:1000 dilution, rabbit polyclonal, clone ab61219, ABCAM), decorin (1:500 dilution, rabbit polyclonal, clone LS-B 8177 / 45156), LSBIO LifeSpan BioSciences), heparan sulfate sulfatase SULF2 (1:100 dilution, rabbit polyclonal, clone AV49338, Sigma Aldrich), and CD31 (1:25 dilution, rabbit polyclonal, clone ab28364, ABCAM, Ki-67 (1:100 dilution, rabbit polyclonal, clone PA5-19462, Thermo Fisher Scientific, IL). All antibodies were initially optimized on control tissues, and positive and negative controls were processed in parallel to the tissue sections.

4.2.7 IHC Scoring

All IHCs were analyzed using the Aperio ScanScope Image Analysis System (Aperio, Vista, CA). PDGFRα, SULF2, and decorin IHCs were analyzed using a Positive Pixel Count algorithm with the Aperio ImageScope viewer. Only areas containing tumor tissue were analyzed for IHC expression. Areas without tumor tissue and areas with necrosis or significant artifacts (e.g. tissue folding) were deselected and excluded from analysis. The number of positive pixels was divided by the total number of pixels (negative and positive) in the analyzed area, and multiplied by 100, to derive the percentage of positive pixels.

Microvessel density (MVD, number of vessels per mm^2) and Mean Vessel Area (MVA, Vascular area/2 + lumen area), using CD31 as a marker, were determined using an Aperio microvessel analysis algorithm. Three representative non-overlapping regions of interest (ROIs) for tumor samples were randomly selected, and the MVD and MVA were quantified for each animal from both untreated and OKN-007–treated groups.

An Aperio ScanScope Image Analysis System was also used to determine the KI-67 labeling index (Ki-67 LI). Three ROIs with the highest number of labeled nuclei were identified in each case. Ki-67 LI was determined by counting 1000 cells and expressing this as the number of labeled cells per 1000 cells [48] for each animal from both untreated and OKN-007–treated groups. Labeled cells adjacent to or within necrotic areas were also excluded while counting the Ki-67 LI. The means and standard deviations of Ki-67 LI were determined for each group.

4.2.8 Statistical analysis

Statistical analyses were performed using Graph Pad Prism 6 (GraphPad Prism 6 Software, San Diego, CA, USA). All p values <0.05 were considered statistically significant. Tumor volumes, metabolite peak length ratios [(NAA^t/Cho^t), (Cho^t/Cre^n), (Cho^t/NAA^t), ($Lip0.9^t/Cre^n$), and ($Lip1.3^t/Cre^n$)], normalized ADC, rCBF, Ki-67 LI, and immunoexpression of PDGFRα, SULF2, and decorin were reported as means ± standard deviations. For statistical analysis, Student t-tests (independent-samples, two-tailed t-test) were used to assess the differences between means of the normal, untreated, and OKN-007 treated pediatric IC-3752GBM glioma mice. Kaplan-Meier survival curves and a Log-rank (mantel-cox) test were used to compare the survival times among the untreated and OKN-007 treated groups.

4.3 RESULTS

Macroscopic, histological, immunohistochemical and MRI characteristics of the novel orthotopic xenograft pediatric glioblastoma (pGBM) model IC-3752GBM and the effects of OKN-007 to inhibit IC-3752GBM tumor cell growth were described in this report.

Gross and microscopic characteristics of the IC-3752GBM pGBM model are presented in Figure 4.1A–E. Macroscopically the tumors were characterized as a yellowish gray, poorly demarcated mass, with multifocal areas of necrosis and hemorrhage. Histological examination revealed highly cellular poorly demarcated, unencapsulated infiltrating neoplasm with marked cell atypia, high mitotic index, and multifocal areas of necrosis and hemorrhage.

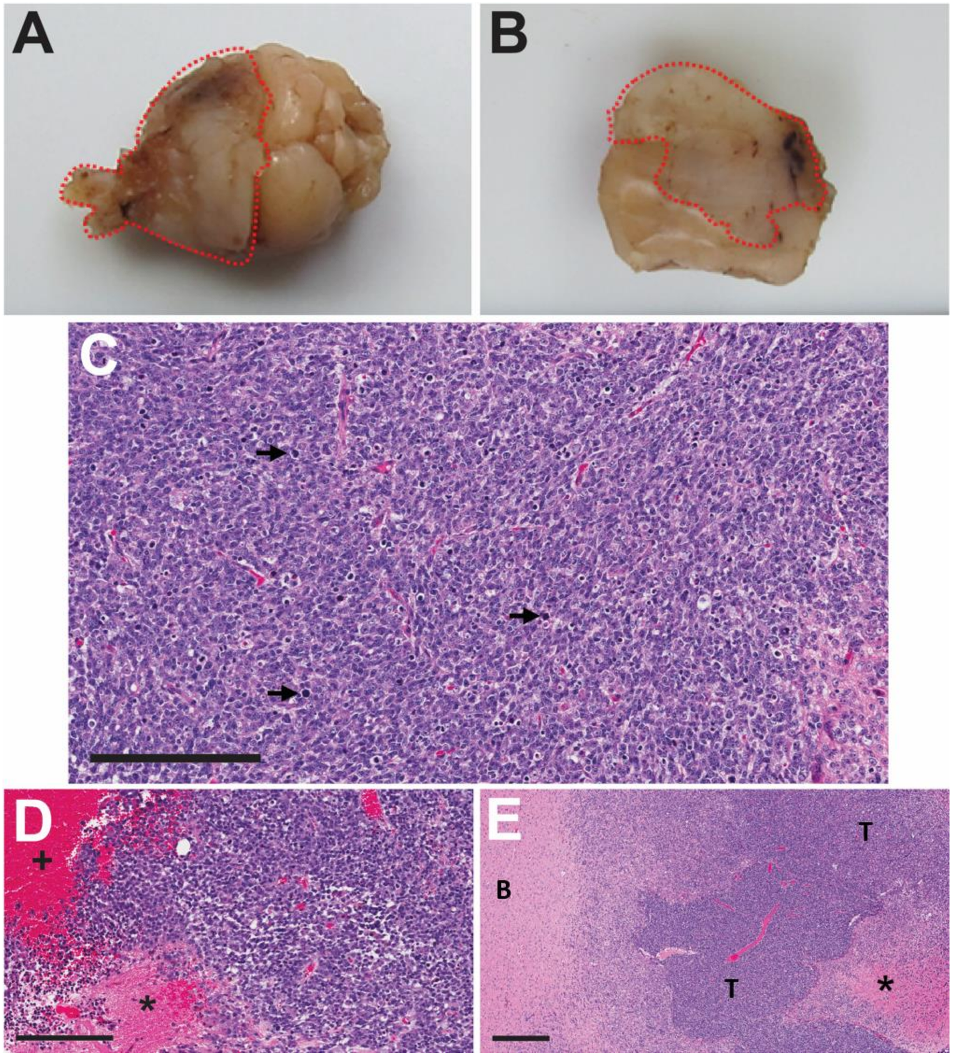

Figure 4.1. Gross and microscopic lesions of the IC3752 pediatric glioma tumor. (A-B) Formalin fixed IC3752 pGBM tissue, characterized as a yellowish gray and poorly demarcated mass, with multifocal areas of necrosis and hemorrhage. (C-E) Histological examination revealed highly cellular, poorly demarcated, unencapsulated, and invasive neoplasms (E) characterized by marked cell atypia, a numerous mitotic figures (black arrows) (C), and multifocal areas of necrosis (asterisks) and hemorrhage (plus sign) (D). T = Tumor, B = normal brain. Scale bar=200 µm (C-D). Scale bar=400 µm (E).

To calculate the whole tumor volume in some animals, MSME T_1-weighted images were performed and acquired before (Fig. 4.2A) and 15 min after (Fig. 4.2B) intravenous contrast agent injection (Gd-DTPA, Magnevist, Bayer Inc., Wayne, NY, USA). Figure 4.3D shows the quantitative mean IC-3752GBM tumor volumes calculated from MR images. Five animals were found to respond to OKN-007 treatment [OKN-007-(R)] and demonstrated significantly smaller tumors ($p = 0.0430$) (Fig. 4.3B) when compared with untreated animals (n=11) (Fig. 4.3A). It was also found that five pGBM mice did not respond [OKN-007-(NR)] to the OKN-007 therapy, and did not show statistical difference ($p = 0.7244$) when compared to the untreated group.

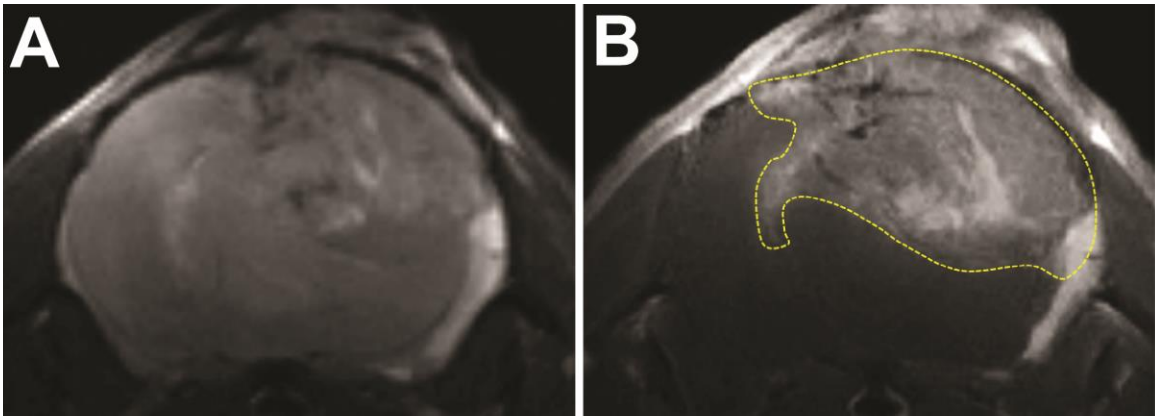

Figure 4.2. Morphological images before and after contrast agent (Gd-DTPA) injection in a pGBM mouse model. (A) T1-weighted MR image. Before contrast administration the tumor appeared as a mildly hyperintense mass without clear demarcation (B) T1-weighted MR image. Fifteen minutes after the contrast injection the IC3752 pGBM demonstrates enhancement, delineating the tumor (yellow dashed line).

Animal survival was assessed by comparing OKN-007–treated animals with untreated animals (Fig. 4.3C). It was found that six animals responded to the OKN-007 treatment and demonstrated significantly longer survival times (*p* = 0.0179) when compared with untreated animals (n=8). Conversely, five pGBM mice did not respond to the OKN-007 therapy, and showed no statistical difference (*p* = 0.4212) when compared to the untreated group.

^{1}H-MRS values were obtained in normal athymic nude mice (n = 7), and untreated (n = 6) and OKN-007–treated (n = 8) mice bearing IC-3752GBM gliomas. Figure 4.4 shows the regions where the single 8mm^3 voxel for ^{1}H-MR spectroscopy was placed in the brains of normal mice (Fig 4.4A) and mice bearing IC-3752GBM gliomas (Fig 4.4B). Figure 4.4C shows that the untreated IC-3752GBM pGBM mice demonstrated significantly lower NAA^t/Cho^t (*p* = 0.0001) and higher Cho^t/Cre^n (*p* = 0.0325), Cho^t/NAA^t (*p* = 0.0075), Lip0.9^t/Cre^n (*p* = 0.0363) and Lip1.3^t/Cre^n (*p* = 0.0009) ratios when compared to the normal athymic mouse brain. The Lip1.3^t/Cre^n (*p* = 0.0395), Lip0.9^t/Cre^n (*p* = 0.0257), Cho^t/NAA^t (*p* = 0.0167), and Cho^t/Cre^n (*p* = 0.0254) ratios were significantly lower in the OKN-007-(R) group than untreated pGBM at the end phase of tumor progression. The OKN-007-(R) group showed a significantly higher NAA^t/Cho^t (*p* = 0.0492) ratio than the untreated pGBM. There was no significant difference between the Cho^t/Cre^n (*p* = 0.498), NAA^t/Cho^t (p = 0.6912), Cho^t/NAA^t (*p* = 0.4231), and Lip0.9^t/Cre^n (*p* = 0.6205) ratios of the normal mouse brain compared to the OKN-007-(R) group. The OKN-007-(R) group showed a significantly higher Lip1.3^t/Cre^n (*p* = 0.0047) ratio than the normal mouse brain. There was no significant difference between the NAA^t/Cho^t (*p* = 0.2071), Cho^t/Cre^n (p = 0.7101), Cho^t/NAA^t (*p* = 0.5362), Lip0.9^t/Cre^n (*p* = 0.7277) and Lip1.3^t/Cre^n (*p* = 0.5163) ratios of the untreated group compared to the OKN-007-(NR) group.

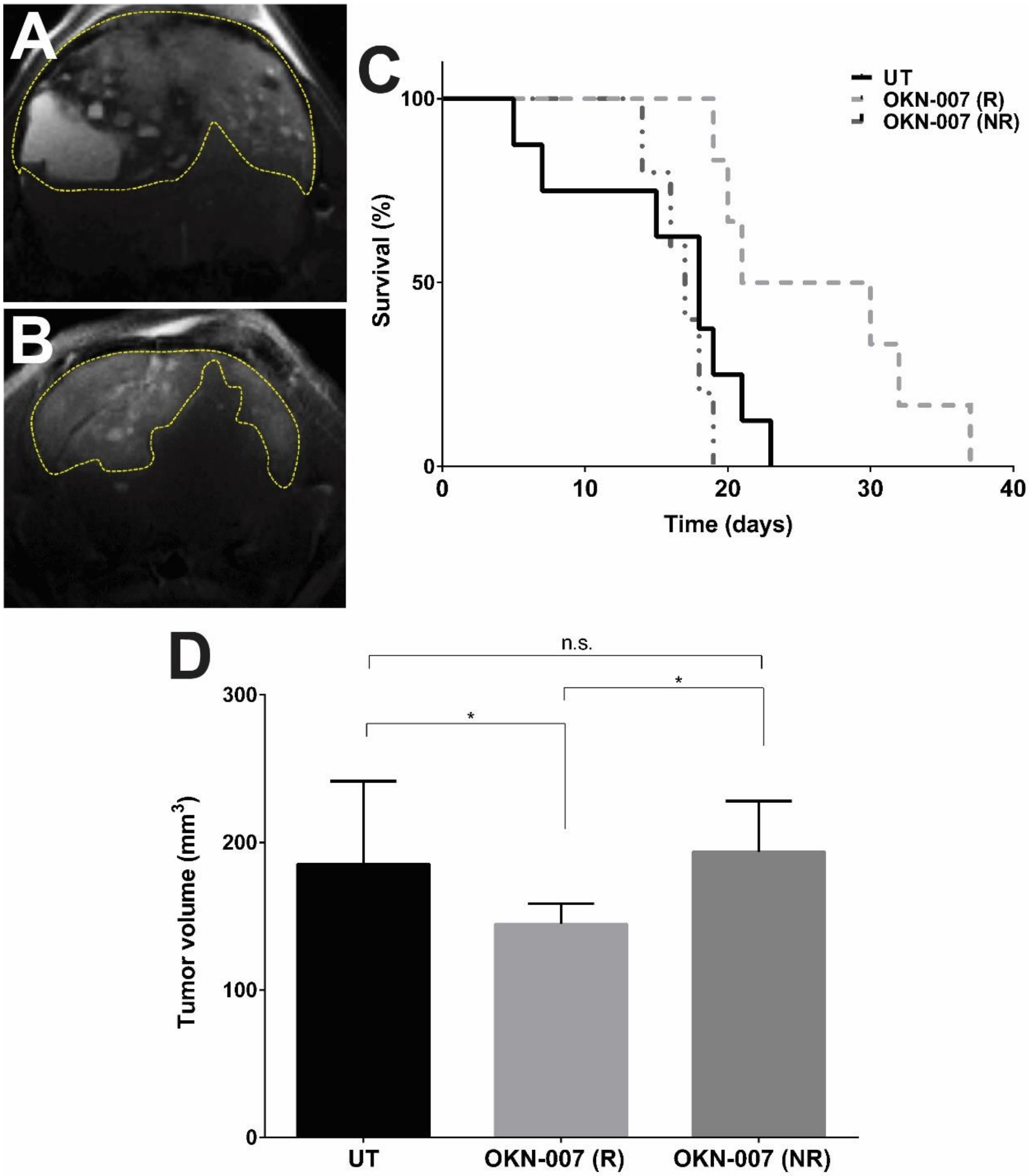

Figure 4.3. Effect of OKN-007 on tumor volumes and survival for IC3752 pGBM tumor bearing mice. Representative T2-weighted MR images of UT (A) and OKN-007 (B) treated IC 3752 pGBM-bearing mouse brains. (C) Six animals responded to the OKN-007 treatment and demonstrated significantly longer survival times (p = 0.0179) when compared with UT animals (n=8). Five pGBM mice did not respond to the OKN-007 therapy, and showed no statistical difference (p = 0.4212) between the UT and OKN-007 (NR) groups. (D) Five animals responded to the OKN-007 treatment [OKN-007 (R)] and demonstrated significantly smaller tumors (p = 0.0430) when compared with UT animals (n=11). However, five pGBM mice did not respond [OKN-007 (NR)] to the OKN-007 therapy, and there was no statistical difference (p = 0.7244) between the UT and OKN-007 (NR) group. Values are represented as means ± SD. Asterisks indicate statistically significant differences (*$p < 0.05$), wheras n.s. are not statistically significant.

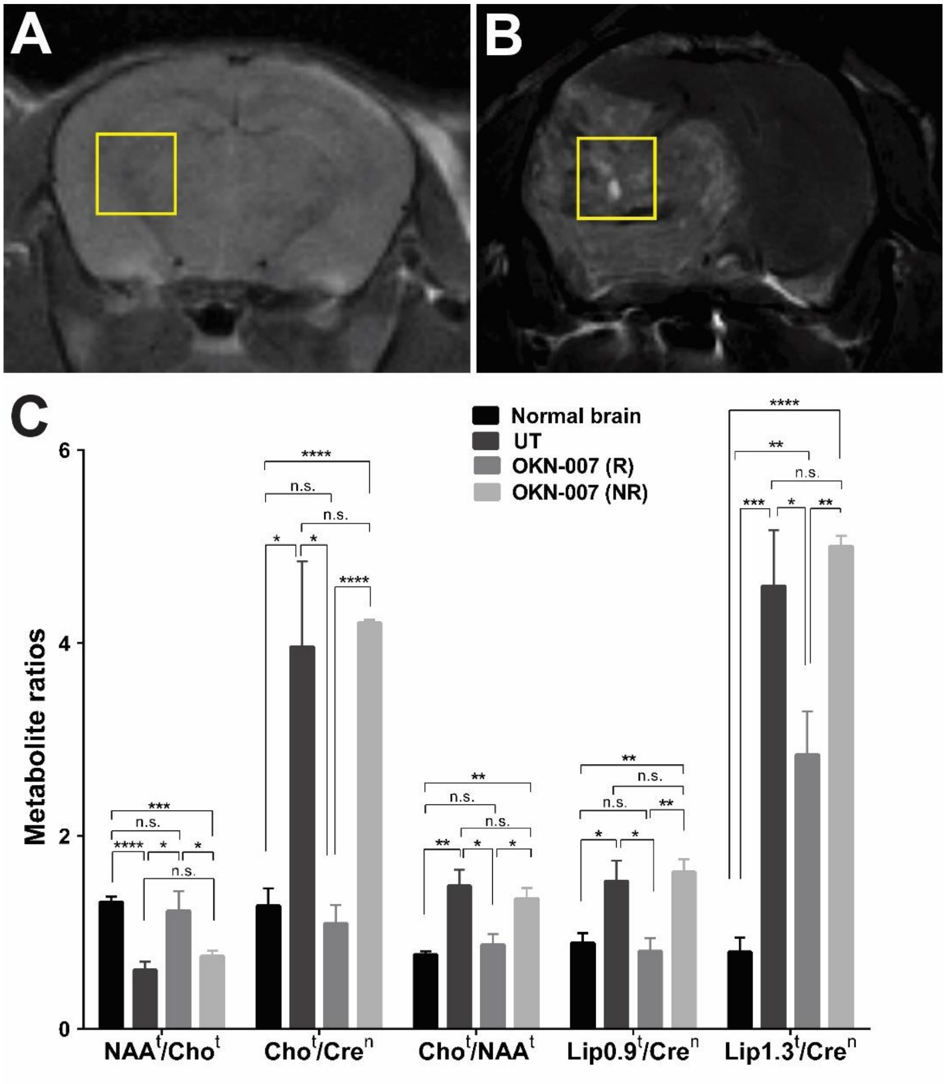

Figure 4.4. Brain metabolite ratios in normal and untreated vs. OKN-007 treated IC3752 pGBM tumor bearing mice. Representative locations of the 2 x 2x 2 mm^3 voxels used to perform 1H-MRS in normal mouse brain (A) and IC3752 pGBM tumor bearing mice (B). (C) The untreated IC3752 pGBM mice demonstrated a significantly lower NAAt/Chot ratio (p = 0.0001) and higher Chot/Cren (p = 0.0325), Chot/NAAt (p = 0.0075), Lip0.9t/Cren (p = 0.0363) and Lip1.3t/Cren (p = 0.0009) ratios when compared to the normal athymic mouse brains. The Lip1.3t/Cren (p = 0.0395), Lip0.9 t/Cren (p = 0.0257), Chot/NAAt (p = 0.0167), and Chot/Cren (p = 0.0254) ratios were significantly lower in the OKN-007-(R) group when compared to untreated pGBM at the end phase of tumor progression. The OKN-007-(R) group showed a significantly higher NAAt/Chot (p = 0.0492) ratio than the untreated pGBM. There was no significant difference between the Chot/Cren (p = 0.498), NAAt/Chot (p = 0.6912), Chot/NAAt (p = 0.4231), and Lip0.9t/Cren (p = 0.6205) ratios for the normal mouse brains compared to the OKN-007-(R) group. The OKN-007-(R) group showed a significantly higher Lip1.3t/Cren (p = 0.0047) ratio than the normal mouse brain. There was no significant difference between the NAAt/Chot (p = 0.2071), Chot/Cren (p = 0.7101), Chot/NAAt (p = 0.5362), Lip0.9t/Cren (p = 0.7277) and Lip1.3t/Cren (p = 0.5163) ratios for the untreated compared to the OKN-007-(NR) groups.

In our study, with the use of DWI, the untreated group showed significantly higher (*p* = 0.0060) (1.161 ± 0.04538, n=11) normalized ADC values in the tumor regions when compared to the normal mice brains (1.003 ± 0.009358, n=6) (Fig. 4.5A-G). The OKN-007–R treated group had significantly higher normalized ADC values (1.296 ± 0.04141, n=7) compared to the untreated group (p = 0.0432) or the normal mice brains (*p* = 0.0003). All OKN-007 treated animals were found to be responsive to the anticancer therapy based on the ADC ratios when compared to the untreated group (Fig. 4.5G).

When using perfusion imaging, the untreated group showed significantly higher (*p* < 0.0001) (0.1372 ± 0.04581, n=9) rCBF values for the tumor regions when compared to the normal mice brains (1.036 ± 0.03305, n=9) (Fig. 4.6A-G). The OKN-007–R treated group had significantly higher rCBF values (0.3624 ± 0.06599, n=4) compared to the untreated group (*p* = 0.0307) or the normal mice brains (*p* = 0.0004). There was no significant difference between rCBF values in the contralateral regions of OKN-007-R [104.8 ± 30.16 mL/(100g x min), n=4] and OKN-007-NR [111.9 ± 34.15 mL/(100g x min), n=2] or untreated [99.17 ± 19.50 mL/(100g x min), n=7] animals (Fig. 4.6G).

Tumor cell proliferation was evaluated via immunoexpression of the anti-Ki-67 antibody. The Ki-67 LI was significantly lower (*p* = 0.0181) in the OKN-007–R treated group (64.15 ± 0.5322, n=4) than in the untreated group (69.93 ± 1.524, n=6) (Fig. 4.7A–C). There was no significant difference (*p* = 0.1822) between the Ki-67 LI of the OKN-007–NR (78.33 ± 4.287, n=2) and untreated group.

Microvessel density (MVD) were measured via the immunoexpression of the anti-CD31 antibody. The MVD was significantly lower (*p* = 0.0358) in the OKN-007–R treated group (12.13 ± 1.648, n=3) than in the untreated group (20.41 ± 2.737, n=7) (Fig. 4.8A–C). There was no significant difference ($p = 0.3092$) between the MVD of the OKN-007–NR (22.55 ± 3.014, n=4) and untreated group.

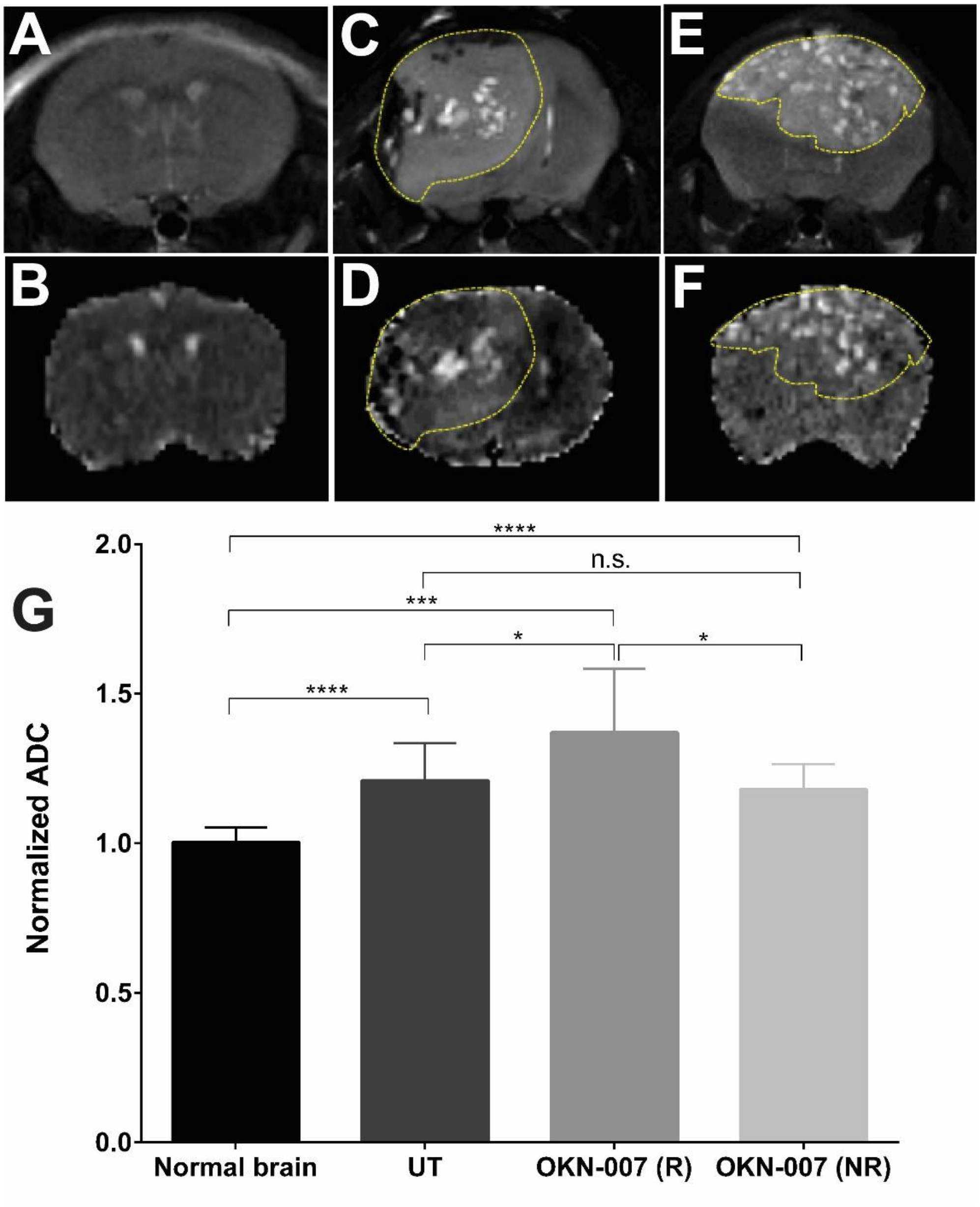

Figure 4.5. Effect of OKN-007 on diffusion measured as ADC values in IC3752 pGBM tumor bearing mice. T2-images (top) and diffusion maps (bottom) of normal mouse brain (A-B), untreated IC3752 pGBM (C-D), and OKN-007-R treated animal (E-F). (G) The untreated group had significantly higher ($p = 0.0060$) (1.161 ± 0.04538, n=11) normalized ADC values for the tumor region when compared to the normal mice brains (1.003 ± 0.009358, n=6). The OKN-007–R treated group showed significantly higher normalized ADC values (1.296 ± 0.04141, n=7) compared to the untreated group ($p = 0.0432$) and normal mice brains ($p = 0.0003$). Values are represented as means ± SD. Asterisks indicate statistically significant difference (*$p < 0.05$).

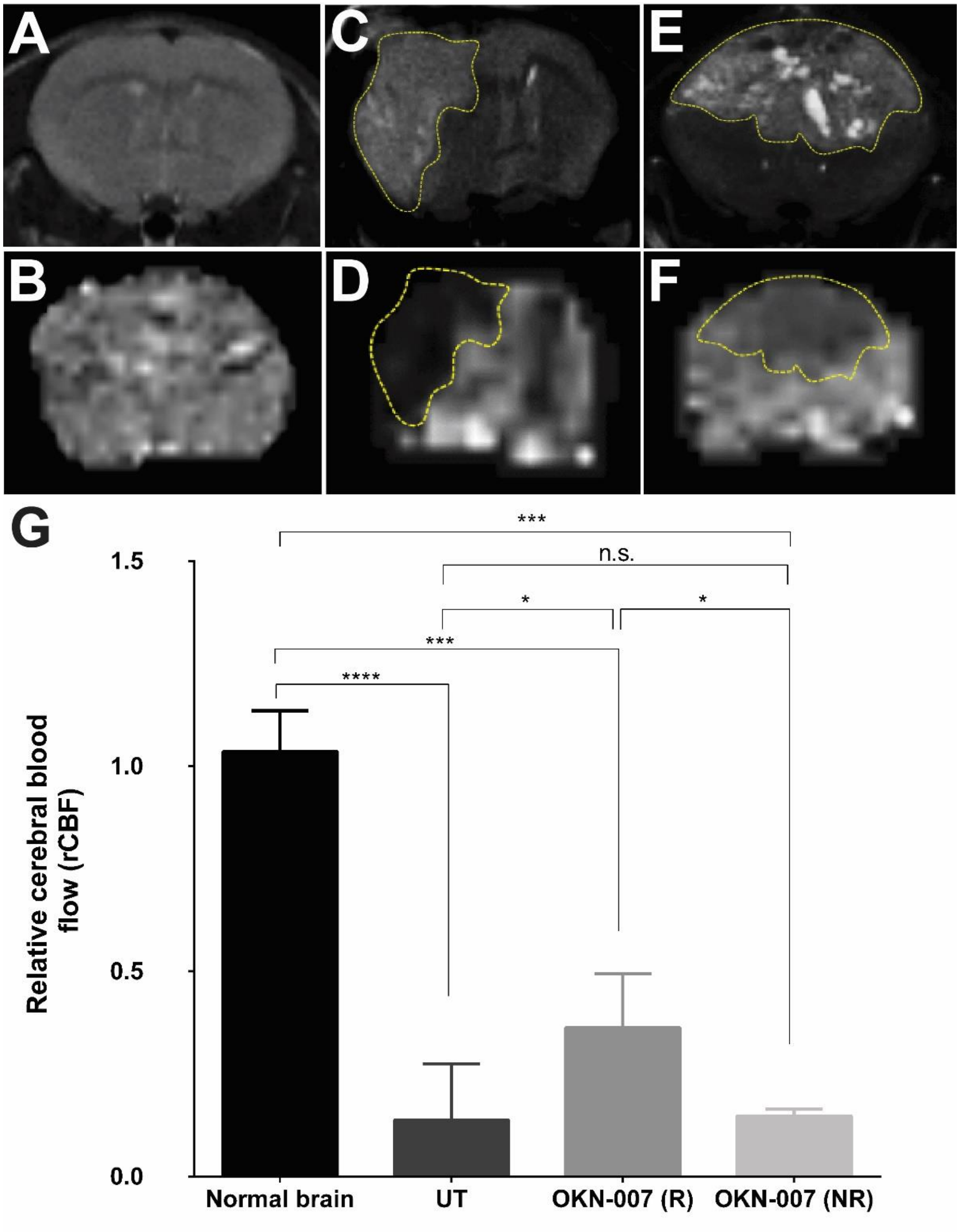

Figure 4.6. Effect of OKN-007 on perfusion rates measured as rCBF in IC3752 pGBM tumor bearing mice. T2-images (top) and perfusion maps (bottom) of normal mouse brain (A-B), untreated IC3752 pGBM (C-D), and OKN-007-R treated animal (E-F). (G) The untreated group showed significantly higher ($p < 0.0001$) (0.1372 ± 0.04581, n=9) rCBF values for the tumor regions when compared to the normal mice brains (1.036 ± 0.03305, n=9). The OKN-007–R treated group showed significantly higher rCBF values (0.3624 ± 0.06599, n=4) compared to the untreated group ($p = 0.0307$) or normal mice brains ($p = 0.0004$). Values are represented as means ± SD. Asterisks indicate statistically significant difference ($*p < 0.05$). n.s.: not statistically significant.

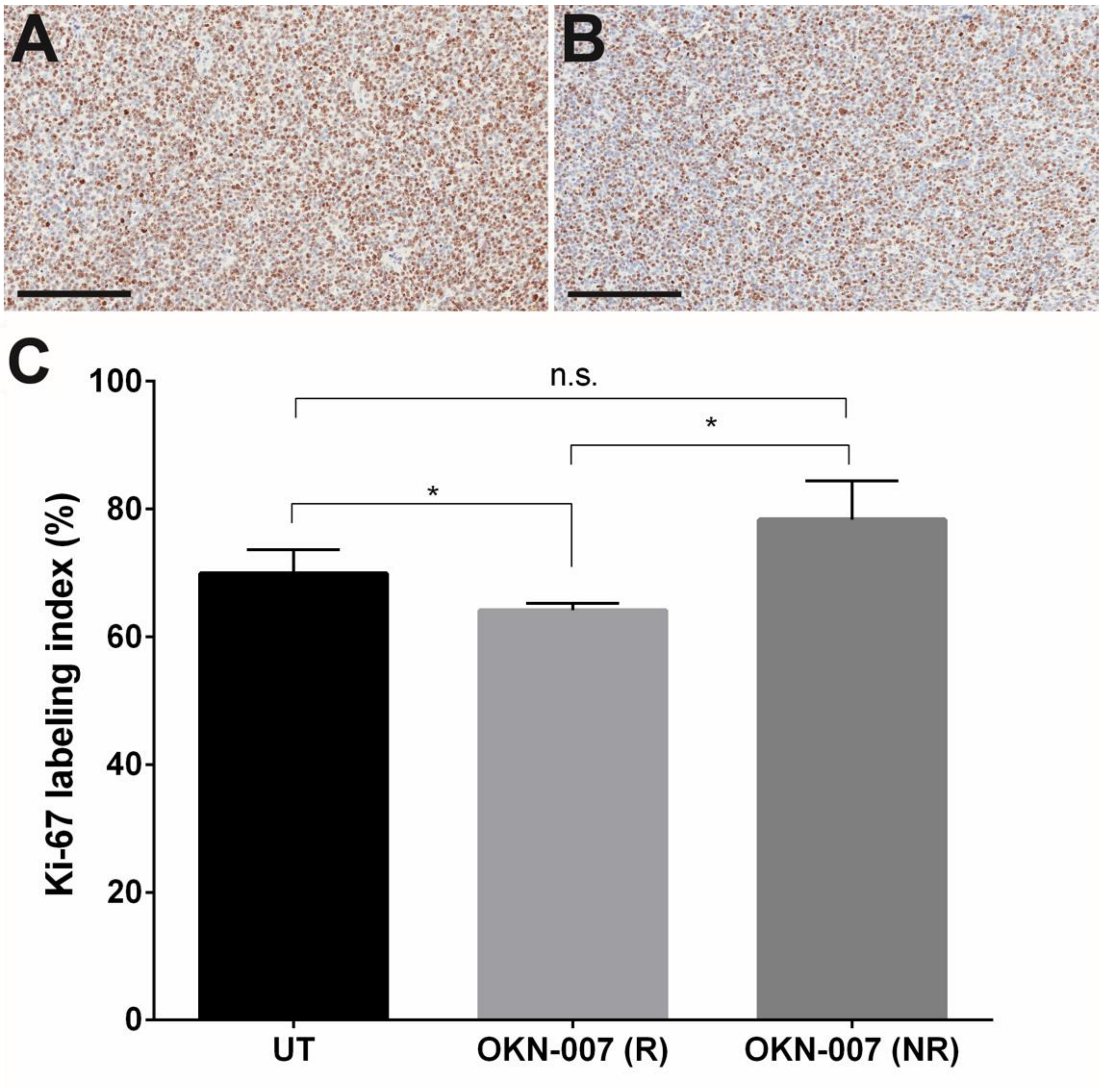

Figure 4.7. Effect of OKN-007 on cell proliferation in IC3752 pGBM tumor bearing mice. Immunohistochemistry images of Ki-67 levels in untreated (A) and OKN-007-treated (B) IC3752 pGBM tumors. (C) Ki-67 LI was significantly lower ($p = 0.0181$) in the OKN-007–R treated group (64.15 ± 0.5322, n=4) than in the untreated group (69.93 ± 1.524, n=6). There was no significant difference ($p = 0.1822$) between the Ki-67 LI of the OKN-007–NR (78.33 ± 4.287, n=2) and the untreated groups. Values are represented as means ± SD. Asterisks indicate statistically significant difference (*$p < 0.05$). n.s.: not statistically significant. Scale bar=200 μm.

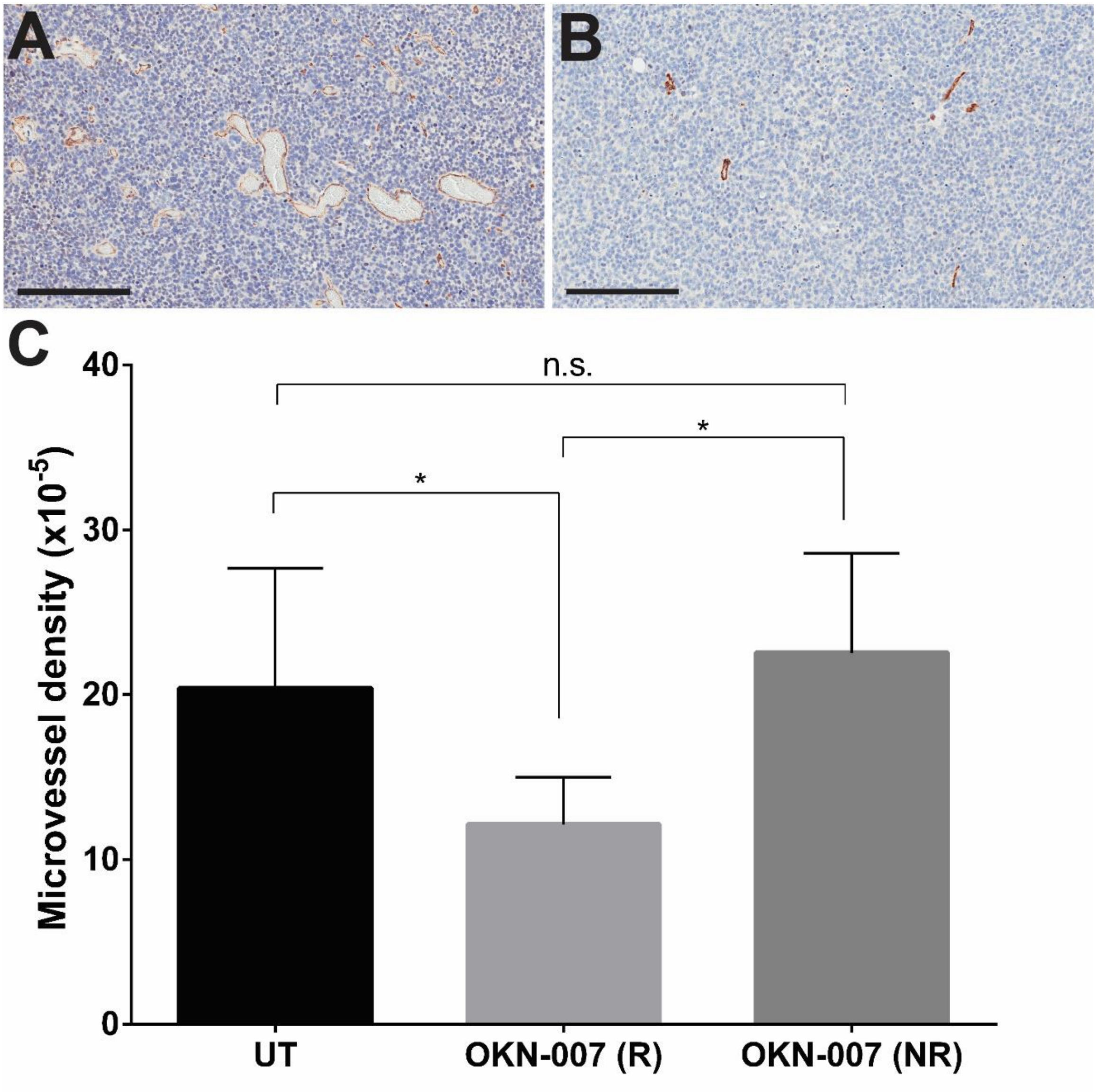

Figure 4.8. Effect of OKN-007 on microvessel density in IC3752 pGBM tumor bearing mice. Microvessel density (MVD) was measured via the immuno-expression of CD31. Immunohistochemistry images of CD31 levels in untreated (A) and OKN-007-treated (B) IC3752 pGBM tumors. (C) The MVD was significantly lower ($p = 0.0358$) in the OKN-007–R treated group (12.13 ± 1.648, n=3) than in the untreated group (20.41 ± 2.737, n=7). There was no significant difference ($p = 0.3092$) between the MVD for the OKN-007–NR (22.55 ± 3.014, n=4) and the untreated groups. The MVA was significantly lower ($p = 0.0009$) in the OKN-007–R treated group (60.26 ± 5.179, n=3) than in the untreated group (127.7 ± 13.27, n=9). There was no significant difference ($p = 0.5090$) between the MVA of the OKN-007–NR (147.0 ± 22.75, n=3) and the untreated groups. Values are represented as means ± SD. Asterisks indicate statistically significant differences (*$p < 0.05$, ** $p < 0.01$). n.s.: not statistically significant. Scale bar=200 μm.

OKN-007 significantly decreased the immunoexpression of PDGFR-α in the treated responsive group (*p* = 0.0429) (28.58 ± 4.743, n=4) when compared to the untreated animals (43.82 ± 3.779, n=6). There was no significant difference (*p* = 0.1400) between the immunoexpression of PDGFR-α of the OKN-007–NR (53.17 ± 3.905, n=3) and the untreated groups (Fig. 4.9).

OKN-007 also significantly decreased the immunoexpression of SULF2 in the treated responsive group (*p* = 0.0339) (23.99% ± 5.187, n=4) when compared to the untreated animals (53.17% ± 7.389, n=3). There was no significant difference (*p* = 0.4180) between the immunoexpression of SULF2 of the OKN-007–NR (45.66% ± 1.686, n=2) and the untreated groups (Fig. 4.10).

The immunoexpression of decorin was significantly higher (p = 0.0478) in the OKN-007–R treated group (22.86 ± 0.1479, n=2) compared to the untreated animals (11.73 ± 3.438, n=4). There was no significant difference (*p* = 0.0167) between the immunoexpression of decorin for the OKN-007–NR (18.44 ± 1.128, n=5) and the untreated groups (Fig. 4.11).

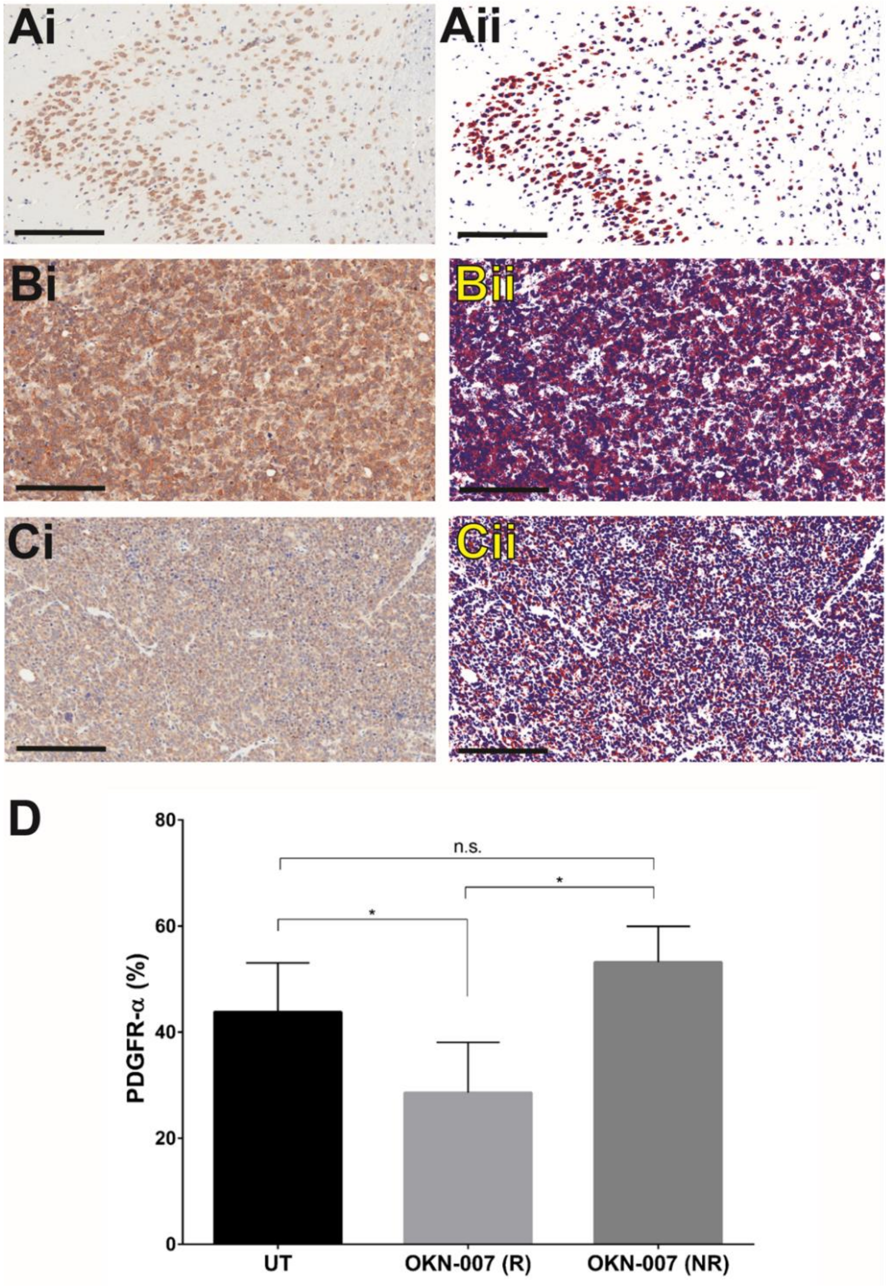

Figure 4.9. Effect of OKN-007 on the immunoexpression of PDGFR-α in IC3752 pGBM tumor bearing mice. (Ai-Ci) Immunoexpression of PDGFR-α in normal mouse brain, IC3752 pGBM UT, and OKN-007 treated animals, respectively. (Aii-Cii) Markup images for the immunoexpression of PDGFR-α in normal mouse brain, IC3752 pGBM UT, and OKN-007 treated animals, respectively. (D) OKN-007 significantly decreased the immunoexpression of PDGFR-α (%) in the treated responsive group ($p = 0.0429$) (28.58 ± 4.743, n=4) when compared to the untreated animals (43.82 ± 3.779, n=6). There was no significant difference ($p = 0.1400$) between the immunoexpression of PDGFR-α of the OKN-007–NR (53.17 ± 3.905, n=3) and the untreated groups. Values are represented as means ± SD. Asterisks indicate statistically significant difference ($*p < 0.05$). n.s.: not statistically significant. Red = positive, blue = background nuclear staining, white = neutral, background. Scale bar=200 μm.

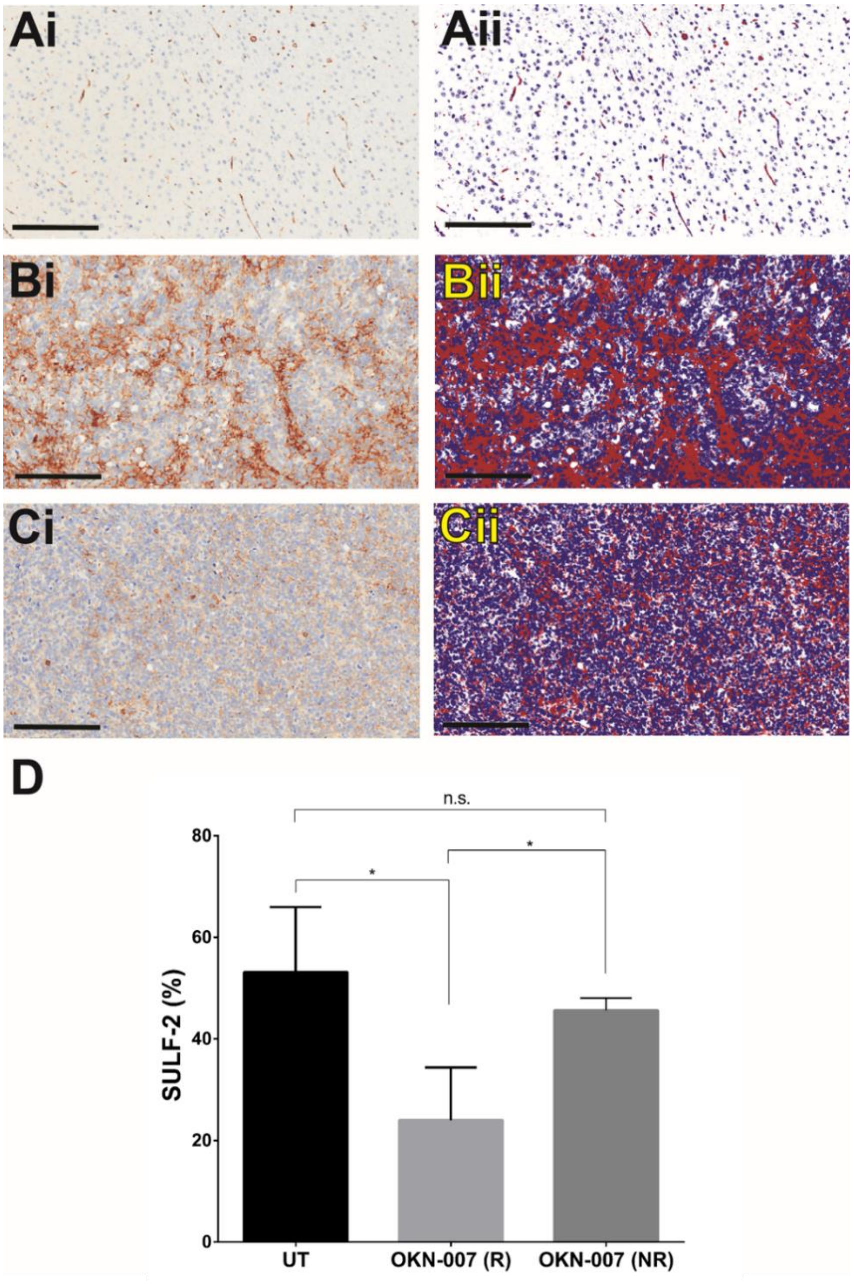

Figure 4.10. Effect of OKN-007 on the immunoexpression of SULF2 in IC3752 pGBM tumor bearing mice. (Ai-Ci) Immunoexpression of SULF2 in normal mouse brain, IC3752 pGBM UT, and OKN-007 treated animals, respectively. (Aii-Cii) Markup images for the immunoexpression of SULF2 in normal mouse brain, IC3752 pGBM UT, and OKN-007 treated animals, respectively. (D) OKN-007 significantly decreased the immunoexpression of SULF2 (%) in the treated responsive group ($p = 0.0339$) (23.99% ± 5.187, n=4) when compared to the untreated animals (53.17% ± 7.389, n=3). There was no significant difference ($p = 0.4180$) between the immunoexpression of SULF2 of the OKN-007–NR (45.66% ± 1.686, n=2) and the untreated groups. Values are represented as means ± SD. Asterisks indicate statistically significant difference (*$p < 0.05$). n.s.: not statistically significant. Red = positive, blue = background nuclear staining, white = neutral, background. Scale bar=200 μm.

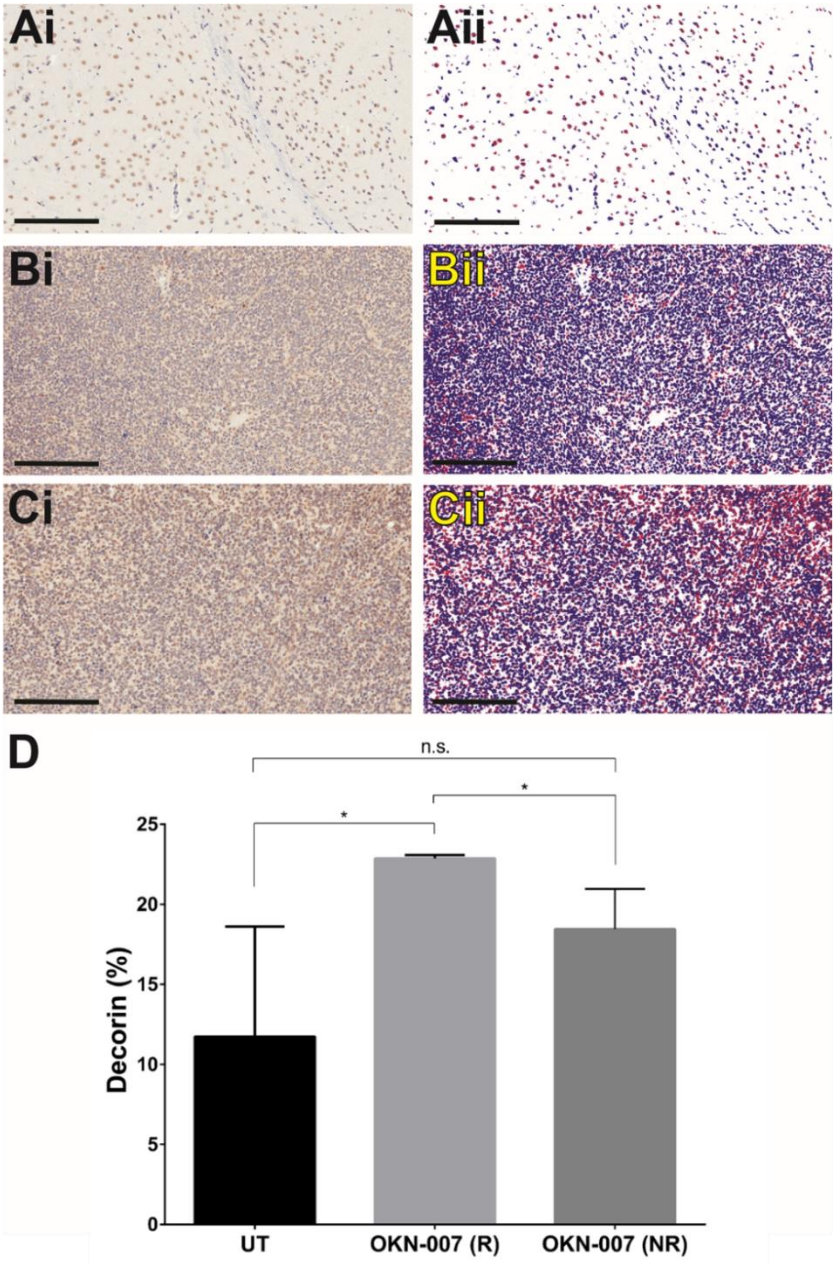

Figure 4.11. Effect of OKN-007 on the immunoexpression of decorin in IC3752 pGBM tumor bearing mice. (Ai-Ci) Immunoexpression of decorin in normal mouse brain, IC3752 pGBM UT, and OKN-007 treated animals, respectively. (Aii-Cii) Markup images for the immunoexpression of decorin in normal mouse brain, IC3752 pGBM UT, and OKN-007 treated animals, respectively. (D) The immunoexpression of decorin was significantly higher (p = 0.0478) in the OKN-007–R treated group (22.86 ± 0.1479, n=2) compared to the untreated animals (11.73 ± 3.438, n=4). There was no significant difference (p = 0.0167) between the immunoexpression of decorin for the OKN-007–NR (18.44 ± 1.128, n=5) and the untreated groups. Values are represented as means ± SD. Asterisks indicate statistically significant difference (*$p < 0.05$). n.s.: not statistically significant. Red = positive, blue = background nuclear staining, white = neutral. Scale bar=200 μm.

4.4 DISCUSSION

Animal modeling for primary brain tumors has undergone constant development over the last 60 years, and significant improvements have been made recently with the establishment of highly invasive glioblastoma models through the direct implantation of patient tumors [10, 46]. However, animal models for pediatric HGGs are still an underexploited tool to make rapid advances in human cancer prevention, diagnosis, and therapy.

This is the first description of the macroscopic, histological, immunohistochemistry and MRI characterizations of the novel orthotopic xenograft pediatric glioblastoma (pGBM) model IC-3752GBM [45], and assessement of the ability of OKN-007 to inhibit IC-3752GBM tumor cell growth. Previous reports are limited to the ^{1}H-MRS characterization of medulloblastomas in transgenic mice [14] and *in vitro* ^{1}H-MRS in other pGBM cell lines [15].

The anti-cancer response to OKN-007 in adult glioma models was previously reported by our group based on morphological (T_2-weighted) imaging, bioluminescence imaging, and immunohistochemistry assessments, in addition to survival data [12, 22-23]. OKN-007 was found to significantly decrease tumor volumes ($p < 0.05$), as measured by MRI, and increase survival ($p < 0.001$) in F98 glioma-bearing rats [23]. Assessment of the treatment response using other MR parameters, such as ^{1}H-MRS, DWI, and perfusion rates, was also performed by our group in C6 rat gliomas [11, 22], but the use of a multi-parametric approach has not been previously reported for any pediatric glioblastoma model.

From gross examination of the IC-3752GBM pGBM (Fig. 4.1A–B), the tumors were characterized as a yellowish gray, poorly demarcated mass, with multifocal areas of necrosis. Histological examination (Fig. 4.1C-E) revealed poorly demarcated, unencapsulated infiltrating neoplasms with marked cell atypia, a high mitotic index, and multifocal areas of necrosis and hemorrhaging, which is comparable to features for GBM in pediatric patients [2].

From contrast-enhanced *in vivo* morphological MR imaging (Fig. 4.2B), IC-3752GBM pGBM tumors were characterized as mildly to markedly hyperintense, with poorly defined margins, and peripheral infiltration , sharing similar MRI characteristics with human glioblastomas [49]. Morphological MR images were also used to determine the volumes of individual tumors, starting on day 25 after the cell implantation, and continuing throughout the entire experiment. For the entire study, the therapeutic responses to OKN-007 were evaluated as either responsive (OKN-007-R) or unresponsive (OKN-007-NR). One cohort of mice (n=5) were found to respond to OKN-007 treatment [OKN-007-(R)] and demonstrated significantly smaller tumors (p = 0.0430) when compared with untreated animals (n=11) (Fig. 4.3D). However, there were also non-responsive mice [OKN-007-(NR)] (n=5) that seemed to be not affected to the OKN-007 therapy. For the responsive mice, our results were similar to prior adult glioma studies of our group, which showed that OKN-007 had a dramatic effect on regressing tumor formation in rat F98 [23] and C6 [12, 22], and human U87 xenograft [23] glioma models.

The survival time of IC-3752GBM pGBM mice was also significantly increased in the responsive group after OKN-007 therapy, as we also have previously reported in adult glioma models [22-23]. The OKN-007-R group (n = 6) had a median survival of 25.5 days, which was significantly longer (p = 0.0179) than the median survival of 18 days for the untreated group (n = 8) (Fig. 4.3C). In our study, OKN-007 was able to increase the survival time by 7.5 days in the responsive group compared to the untreated animals. Considering that one mouse month is equivalent to ∼2.6 human years, based on a 4-year maximum life span [50-51], OKN-007 could potentially increase survival time in pediatric GBM patients by ~7-8 months.

We also assessed the OKN-007 treatment response by using other MR parameters, such as ^{1}H-MRS to measure tumor metabolites, DWI to assess structural alterations, and perfusion rates to evaluate microvascularity alterations. ^{1}H-MRS is a non-invasive technique that measures the concentration of a variety of biomolecules from a volume of interest [52].

MRS findings have been shown to be closely related to the histological features of glioma cells and can be used for evaluating tumor differentiation, grading, follow-up and radiotherapy planning [53-55]. MRS is also a valuable tool for identifying early changes in glioma metabolism and the extent of glioma infiltration [56-58]. The technique is widely available clinically and easily appended to a standard MRI examination, which is routinely performed at the time of diagnosis on children with brain tumors [59]. The principal metabolites that can be assessed by ^{1}H-MRS in brain tumors include choline (Cho, 3.2 ppm), creatine (Cre, 3.0 ppm), N-acetylaspartate (NAA, 2.0 ppm), and lipids (Lip; 0.9–1.3 ppm) [58].

Choline is a constituent molecule associated with the phospholipid metabolism of cell membranes and reflects membrane turnover [61]. Its concentration is slightly greater in white matter than in gray matter [61]. Increased Cho indicates greater membrane synthesis and cell proliferation [61]. Its concentration is markedly increased in cases of brain neoplasms [61]. Phosphocholine and glycerophosphocholine also contribute to the representation of the Cho peak in ^{1}H-MRS [61].

Creatine is a marker of aerobic energy metabolism in brain cells, and is present in larger concentrations in the gray matter than in the white [61]. Creatine and phosphocreatine, both of which contribute to the Cre pool, are found in both neurons and glial cells [61]. Cre and phosphocreatine remain relatively stable *in vivo,* and therefore their peak is often used as an internal concentration standard [62]. However, recent studies have suggested that the Cre levels may be altered in human gliomas [63].

N-acetyl aspartate, a free amino acid, is almost exclusively located in neurons and axons, and is the most prominent signal observed in ^{1}H-MRS for the CNS. The NAA peak in ^{1}H-MRS is decreased whenever there is neuron loss, such as in gliomas, ischemia and degenerative diseases [61]. A strong association between ^{1}H-MRS detectable lipids and tumor grade has been reported in adult gliomas [64-66] and childhood brain tumors [67] suggesting that high intracellular lipid levels are a non-invasive marker of brain tumor malignancy. Studies on cultured cells, *ex-vivo* tumor tissue and animal models have shown that an increase in MRS detectable lipids is associated with cell stress [68], apoptosis [69] and hypoxia as a result of compromised vascularity [70]. MRS detectable lipids are therefore associated with several factors known to be present in aggressive tumors that have a poor prognosis.

In our study, we measured the peak areas of Cho, Cre, NAA, Lip0.9, and Lip1.3 in the normal brain of athymic nude mice and untreated and OKN-007 treated IC-3752GBM pGBM bearing mice. Those values were used to determine the following ratios: tumor NAA to tumor Cho (NAA^t/Cho^t), tumor Cho to contralateral Cre (Cho^t/Cre^n), tumor Cho to tumor NAA (Cho^t/NAA^t), tumor Lip0.9 to contralateral Cre ($Lip0.9^t/Cre^n$), and tumor Lip1.3 to contralateral Cre ($Lip1.3^t/Cre^n$). The untreated IC-3752GBM pGBM mice demonstrated significantly lower NAA^t/Cho^t ($p = 0.0001$) and higher Cho^t/Cre^n ($p = 0.0325$), Cho^t/NAA^t ($p = 0.0075$), $Lip0.9^t/Cre^n$ ($p = 0.0363$) and $Lip1.3^t/Cre^n$ ($p = 0.0009$) ratios when compared to the normal athymic mouse brain (Fig. 4.4C), which corroborates with metabolite profiles observed in human GBM. Typical ^{1}H-MRS findings for cerebral gliomas includes reduction of NAA, variable levels of Cr, and an elevation in Cho and lipids, in proportion to glioma grade [71].

The role of mobile lipids in cancer has been the subject of many excellent reviews and articles [11-12, 70, 72-79]. In brain tumors, the elevation of lipid levels usually correlates with necrosis [72, 74, 80-81], and are considered as important biomarkers for diagnosis and monitoring the effects of treatment response [72]. A number of studies have also demonstrated that an increase in mobile lipids is associated with the onset of drug-induced apoptosis [68, 72]. OKN-007 significantly reduced the lipid peaks at 1.3ppm ($p = 0.0395$) and 0.9 ppm ($p = 0.0257$) in treated animals compared to the untreated group, which could be related to a decrease in tumor necrosis by OKN-007 in treated animals. This anticancer property of OKN-007 may be very beneficial for GBM patients, since necrosis is caused by tumor hypoxia as a result of increased cell proliferation and mitotic activity, as well as insufficient tissue perfusion [82], and it is present in over 85% of cases [83-86].

The IC-3752GBM pGBM bearing mice treated with OKN-007 showed a significantly lower Cho^t/NAA^t ratio ($p = 0.0167$) than the untreated group. The effect of OKN-007 on the Cho/NAA ratio in the IC-3752GBM pGBM model is remarkable, since it has been reported that the Cho/NAA ratio provides a sensitive method for detecting differences in tumor growth [87]. Furthermore, baseline Cho/NAA ratios and the percent change in Cho/NAA over time have also been associated with poor prognosis in childhood brain tumors [88-90]. Lower Cho/NAA ratios seem to be predictive of a poor outcome in children with recurrent primary brain tumors, and should be evaluated as a prognostic indicator in newly diagnosed childhood brain tumors [88].

The Cho^t/Cre^n ratios also significantly decreased ($p = 0.0254$) after OKN-007 treatment in responsive animals compared to untreated pGBM at the end phase of tumor progression (Fig 4.4C), indicating that the drug was also capable of decreasing tumor cell proliferation in ~50% of animals in this pediatric glioma model. The ^{1}H-MRS results were also confirmed with IHC that showed significantly lower ($p = 0.0181$) immunoexpression of Ki-67 (cell proliferation marker) in the OKN-007–R treated group compared to untreated animals (Fig. 4.7C).

Diffusion-weighted imaging (DWI) represents another promising imaging tool for tissue characterization, prediction, and the evaluation of therapeutic response in oncology [91]. DWI is routinely used to measure microscopic, random translational motion of water molecules within tissues. Any alterations in the tissue structure that disrupt the barriers of water diffusion, such as the breakdown of cell membranes or damage to fibers, would lead to changes in the diffusion properties within these regions. These diffusion characteristics can be quantified by estimating the ADC (Apparent Diffusion Coefficient). In tumors, ADC values can differentiate the cellular mechanisms involved in tumor development as well as responses to treatment such as cell proliferation, apoptosis, and/or necrosis [92]. Both intra- and extracellular spaces and their exchange contribute to the measured ADC [93]. DWI has also a tremendous potential for monitoring early changes in tumor cellularity that are thought to be reflective of treatment response [93]. As cellular density increases, the added tortuosity to extracellular mobility paths reduces water mobility and, consequently, the ADC value [94]. Processes that degrade cellular integrity, such as necrosis caused by therapy or tumor growth, are thought to increase the ADC of tissue [94-95]. Successful treatment of a tumor with a cytotoxic agent will result in significant damage to the tumor cells in the form of a loss of cell membrane integrity with a subsequent reduction in tumor cell density. This has a net effect of increasing the fractional volume of the interstitial space because of cell loss, resulting in an increase in the mobility (diffusion) of water within the damaged tumor tissue [93].

In our study, the untreated group showed significantly higher ($p = 0.0060$) (1.161 ± 0.04538, n=11) normalized ADC values for the tumor region when compared to the normal mice brain (1.003 ± 0.009358, n=6) (Fig. 4.5G). The OKN-007–R treated group showed significantly higher normalized ADC values (1.296 ± 0.04141, n=7) than the untreated group ($p = 0.0432$) and normal mice brains ($p = 0.0003$). Interestingly, all OKN-007 treated animals were responsive to the therapy based on the ADC ratios when compared to the untreated group. The observed increase in water ADC following therapy is directly related to the number of tumor cells killed and is thought to be due to the liberation of water into the extracellular space [94].

Arterial spin labeling (ASL) is a non-invasive magnetic resonance technique for tissue perfusion quantification without the application of contrast media. Perfusion is defined as the amount of blood delivered to capillary beds in a given tissue per unit time. Delivery of blood to a capillary bed is a critical indicator of tissue viability and function, and the analysis of perfusion [96], which has markedly contributed to the understanding of physiological and pathological processes in the human body [97]. Furthermore, the ASL technique has been useful for monitoring the effects of agents designed to modulate tumor blood flow and oxygenation (e.g., carbogen gas) [98], and for evaluating and guiding the use of anti-angiogenic agents [44].

Antiangiogenic therapy might affect tumor vessels in 3 different ways: no effect at all; excessive destruction of blood vessels and a reduction in perfusion leading to increased hypoxia, necrosis, and/or invasion; or after pruning of some abnormal vessels the overall structure of the remaining tumor vessels may resemble normal vessels, which potentially results in an increase in absolute blood perfusion [99]. In this study, we measured the changes in normalized relative cerebral blood perfusion (rCBF) in normal athymic mouse brains, and in untreated and OKN-007 treated IC-3752GBM pGBM mice, using the ASL perfusion MRI technique. The untreated group showed significantly lower ($p < 0.0001$) (0.1372 ± 0.04581, n=9) rCBF values for the tumor region when compared to the normal mice brain (1.036 ± 0.03305, n=9) (Fig. 4.6G). The OKN-007–R treated group showed significantly higher rCBF values (0.3624 ± 0.06599, n=4) compared to the untreated group ($p = 0.0307$) and significantly lower than normal mice brains ($p = 0.0004$). Interestingly, the drug did not seem to affect the normal perfusion of the brain, as no differences were found between values in the contralateral regions of OKN-007-R [104.8 ± 30.16 mL/(100g x min), n=4] and OKN-007-NR [111.9 ± 34.15 mL/(100g x min), n=2] and untreated [99.17 ± 19.50 mL/(100g x min), n=7] animals (Fig. 4.6G), being consistent with the findings from previous research studies in OKN-007-treated C6 gliomas [22]. Our results also corroborate with the literature that indicates that glioblastomas have lower blood perfusion rates than that of the surrounding normal brain because of their inefficient, irregular vessels that are leaky and dilated with a haphazard pattern of interconnection [99-100].

The positive effect of OKN-007 on perfusion and diffusion properties in IC-3752GBM pGBM bearing mice indicates a promising influence of the drug on tumor microvasculature, which was also shown previously in a rat adult glioma model by our group [22]. In our study, we were also able to demonstrate that OKN-007 acts as an antiangiogenic agent in the IC-3752GBM pGBM model. To support this notion, microvessel density (MVD) was significantly lower (p = 0.0358) in the OKN-007–R treated group than in the untreated group (Fig. 4.8C). The normalization of tumor vasculature is a necessary step for cancer therapies [101]. This effect may be mediated by the anti-inflammatory properties of OKN-007. Indeed, alterations to inflammatory pathways can modify angiogenesis [102], and inflammatory mediators are known to modulate blood–brain barrier permeability [103]. Therefore it could be expected from the anti-inflammatory properties of nitrone compounds, that administration of OKN-007 positively altered the integrity and function of the microvascular bed at the tumor site, consequently increasing the ADC ratios and rCBF values in responsive treated animals.

We also assessed the effect of OKN-007 regarding the immunoexpression of tumor signaling molecules such as *PDGFRα*, SULF2, and decorin in the IC-3752GBM pGBM model. Although childhood and adult HGGs share related histopathological characteristics, recent studies have shown substantial differences in the molecular features underlying pediatric and adult HGGs. The epidermal growth factor receptor is the predominant receptor tyrosine kinase targeted by both amplification and mutation in adult glioblastomas [104-105]. In contrast, *PDGFRα* is the most frequent target of focal amplification in pediatric HGGs arising within and outside the brainstem [106-110], and somatic mutations of *PDGFRα* have been recently reported in pediatric HGGs [108-109, 111]. Another study revealed that the high expression of phosphorylated *PDGFRα* has a significant association with malignant histology in pediatric gliomas [112]. The expression of *PDGFRα* has also been demonstrated in medulloblastomas and primitive neuroectodermal tumors, and an increase in *PDGFRα* gene copy numbers seems to be associated with poor survival in these tumors [113].

SULF2, a heparan sulfate endosulfatase, has been associated to different types of cancers including lung [114], breast [115], liver [116], gastric [117], and brain tumors [118]. In brain cancer, SULF2 has been directly implicated in driving tumorigenesis in murine and human malignant gliomas [119]. The SULF2 protein is highly expressed in primary human GBM, and SULF2 levels are inversely related to heparan sulfate proteoglycan (HSPG) 6O-sulfation in a murine model for GBM [119]. SULF2 gene expression is also significantly positively correlated with PDGFRα expression [120]. Furthermore, the ablation of SULF2 decreases tumor growth, prolongs host survival and decreases the activity of PDGFRα, as well as related downstream signaling pathways in human and mouse malignant gliomas [119].

Decorin is a small proteoglycan found in the extracellular matrix of a variety of tissues and cell types [120-121]. It interacts with a diversity of proteins that are involved in matrix assembly [122] and in the regulation of fundamental biological functions such as cell attachment [123], migration [124], and proliferation [125]. Decorin inhibits cell proliferation in several tumor cell types, including ovarian [123], liver [126], and brain tumor cells [127]. Similarly to SULF2, decorin is also associated to the PDGFRα pathway. Interestingly, decorin does not colocalize with PDGFRα, but binds directly to its natural ligand PDGF, directly blocking the activity of PDGFRα [126]. Furthermore, it is known that decorin antagonizes the angiogenic network [128] due to the inhibition of the production of VEGF (vascular endothelial growth factor) by tumor cells and can directly blocking of VEGFR2 (vascular endothelial growth factor receptor-2) at the same time [129].

Our current data showed that OKN-007 was able to significantly decrease the immunoexpression of SULF2 ($p = 0.0339$) in responsive mice compared to untreated animals, which has also been recently demonstrated in hepatocellular cancer cells [130]. Furthermore, OKN-007 was able to significantly decrease the immunoexpression of PDGFRα ($p = 0.0429$) and significantly increase the expression of decorin ($p = 0.0478$) in responsive IC-3752GBM pGBM tumor bearing mice, compared to untreated animals, which may be also associated to the inhibition of tumor angiogenesis and cell proliferation which was also observed in the OKN-007-R treated animals from this study. Figure 4.12 depicts the possible mechanism-of-action of OKN-007 in pGBM.

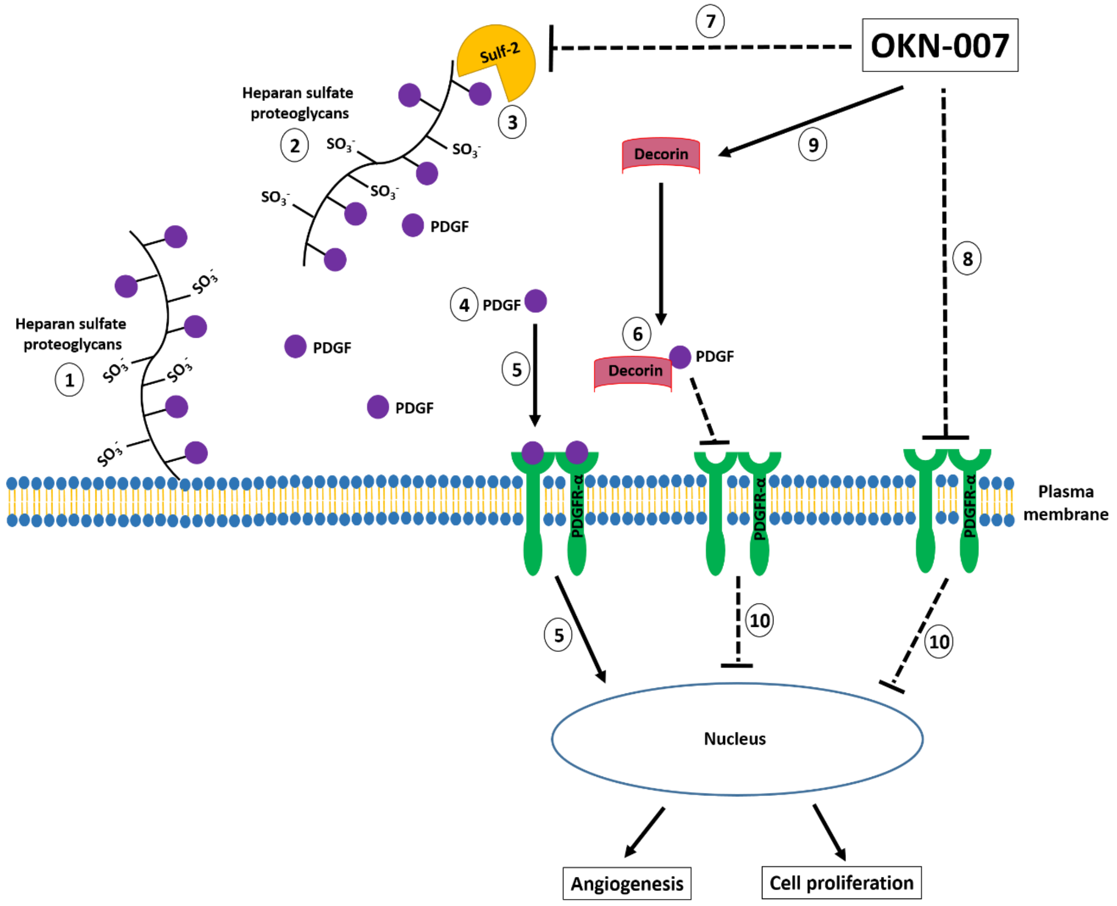

Figure 4.12. Schematic representation of possible mechanism of action of OKN-007 in IC3752 pGBM tumor bearing mice. Heparan sulfate proteoglycans (HSPG) consist of a protein core and heparan sulfate (HS) chains consisting of linear carbohydrate chains of repeating disaccharide units. Dependent on the HSPG core protein, HSPGs are found at the cell surface (1), in the extracellular matrix (2), or in secretory vesicles [119]. Essential for their function in cell signaling, the HS chains undergo extensive post-translational modifications, including sulfation on the 6-O- position of glucosamine [131]. By removing 6-O-sulfates on HS chains and mobilizing protein ligands from HSPG sequestration in the extracellular environment (3), the SULF-2 can increase the solubility of a variety of growth factors (e.g. PDGF) (4) thus increasing the activation of PDGFR-α and downstream signaling pathways in tumor cells (5) [119]. Similarly to SULF2, decorin is also associated to the PDGFRα pathway. Interestingly, decorin does not co-localize with PDGFRα, but binds directly to its natural ligand PDGF, directly blocking the activity of PDGFRα (6) [126]. Our current data showed that OKN-007 was able to decrease the immunoexpression of SULF2 (7) and PDGFRα (8), and increase the expression of decorin (9) in IC3752 pGBM tumor bearing mice, which may be also associated to the inhibition of tumor angiogenesis and cell proliferation (10) also observed in OKN-007 treated animals. SO3-: sulfate, PDGF: Platelet-derived growth factor. The schematic is a modification of combined schemes obtained from Oncotarget, 3(5): 568–575, Phillips JJ (2012) [119] (Copyright (2012) with permission from Impact Journals), and from FEBS Journal, 280(10):2150-2164, Baghy K et al., (2013) [126] (Copyright (2013) with permission from John Wiley and Sons).

4.5 CONCLUSIONS

The data taken as a whole indicates that OKN-007 may be an effective anti-cancer agent for some patients with pHGGs by inhibiting cell proliferation and angiogenesis, possibly via the PDGFRα pathway, and could be considered as an additional therapy for pediatric brain tumor patients. Currently, OKN-007 is an investigational drug in phase Ib/IIa clinical trials for recurrent adult GBM patients. Our future plan is to conduct clinical trials in pGBM patients using OKN-007 as an adjunct therapy to help inhibit tumor growth associated with this devastating disease in children.

4.6 REFERENCES

1. Bondy ML, Scheurer ME, Malmer B, Barnholtz-Sloan JS, Davis FG, Il'yasova D, et al. Brain Tumor Epidemiology Consortium. Brain tumor epidemiology: consensus from the Brain Tumor Epidemiology Consortium. Cancer. 2008; 113:1953-68.

2. Louis DN, Ohgaki H, Wiestler OD, Cavenee WK, Burger PC, Jouvet A, et al. The 2007 WHO classification of tumours of the central nervous system. Acta Neuropathol. 2007;114: 97-109.

3. Bielen A, Perryman L, Box GM, Valenti M, de Haven Brandon A, Martins V, et al. Enhanced efficacy of IGF1R inhibition in pediatric glioblastoma by combinatorial targeting of PDGFRα/β. Mol Cancer Ther. 2011;10:1407-18.

4. Broniscer A, Gajjar A. Supratentorial high-grade astrocytoma and diffuse brainstem glioma: two challenges for the pediatric oncologist. Oncologist. 2004; 9:197-206.

5. MacDonald TJ, Aguilera D, Kramm CM. Treatment of high-grade glioma in children and adolescents. Neuro Oncol. 2011; 13:1049-58.

6. Cage TA, Mueller S, Haas-Kogan D, Gupta N. High-grade gliomas in children. Neurosurg Clin N Am. 2012;23:515–523.

7. Fouladi M, Stewart CF, Blaney SM, Onar-Thomas A, Schaiquevich P, Packer RJ, et al. Phase I trial of lapatinib in children with refractory CNS malignancies: a Pediatric Brain Tumor Consortium study. J Clin Oncol. 2010; 28:4221-7.

8. Geoerger B, Morland B, Ndiaye A, Doz F, Kalifa G, Geoffray A, et al. Innovative Therapies for Children with Cancer European Consortium. Target-driven exploratory study of imatinib mesylate in children with solid malignancies by the Innovative Therapies for Children with Cancer (ITCC) European Consortium. Eur J Cancer. 2009;45:2342-51.

9. Broniscer A, Baker SJ, Stewart CF, Merchant TE, Laningham FH, Schaiquevich P, et al. Phase I and pharmacokinetic studies of erlotinib administered concurrently with radiotherapy for children, adolescents, and young adults with high-grade glioma. Clin Cancer Res. 2009;15:701–7.

10. Huszthy PC, Daphu I, Niclou SP, Stieber D, Nigro JM, Sakariassen PØ, et al. In vivo models of primary brain tumors: pitfalls and perspectives. Neuro Oncol. 2012;14:979-93.

11. Doblas S, He T, Saunders D, Hoyle J, Smith N, Pye Q, et al. In vivo characterization of several rodent glioma models by 1H MRS. NMR Biomed. 2012;25:685-94.

12. He T, Doblas S, Saunders D, Casteel R, Lerner M, Ritchey JW, et al. Effects of PBN and OKN007 in rodent glioma models assessed by 1H MR spectroscopy. Free Radic Biol Med. 2011;51:490-502.

13. Jones TS, Holland EC. Animal models for glioma drug discovery. Expert Opin Drug Discov. 2011;6:1271-83.

14. Hekmatyar SK, Wilson M, Jerome N, Salek RM, Griffin JL, Peet A, et al. ^{1}H nuclear magnetic resonance spectroscopy characterisation of metabolic phenotypes in the medulloblastoma of the SMO transgenic mice. Br J Cancer. 2010;103:1297-304.

15. Al-Saffar NM, Marshall LV, Jackson LE, Balarajah G, Eykyn TR, Agliano A, et al. Lactate and choline metabolites detected in vitro by nuclear magnetic resonance spectroscopy are potential metabolic biomarkers for PI3K inhibition in pediatric glioblastoma. PLoS One. 2014;9:e103835.

16. Liu Z, Zhao X, Wang Y, Mao H, Huang Y, Kogiso M, et al. A patient tumor-derived orthotopic xenograft mouse model replicating the group 3 supratentorial primitive neuroectodermal tumor in children. Neuro Oncol. 2014;16:787-99.

17. Yu L, Baxter PA, Voicu H, Gurusiddappa S, Zhao Y, Adesina A, et al. A clinically relevant orthotopic xenograft model of ependymoma that maintains the genomic signature of the primary tumor and preserves cancer stem cells in vivo. Neuro Oncol. 2010;12:580-94.

18. Mullins CS1, Schneider B, Stockhammer F, Krohn M, Classen CF, Linnebacher M. Establishment and characterization of primary glioblastoma cell lines from fresh and frozen material: a detailed comparison. PLoS One. 2013;8:e71070.

19. Pietsch T, Scharmann T, Fonatsch C, Schmidt D, Ockler R, Freihoff D, et al. Characterization of five new cell lines derived from human primitive neuroectodermal tumors of the central nervous system. Cancer Res. 1994;54:3278-87.

20. Grunda JM, Wang D, Clines GA. Development and characterization of murine models of medulloblastoma extraneural growth in bone. Clin Exp Metastasis. 2013;30:769-79.

21. Xu J, Erdreich-Epstein A, Gonzalez-Gomez I, Melendez EY, Smbatyan G, Moats RA, et al. Novel cell lines established from pediatric brain tumors. J Neurooncol. 2012;107:269-80.

22. Garteiser P, Doblas S, Watanabe Y, Saunders D, Hoyle J, Lerner M, et al. Multiparametric assessment of the anti-glioma properties of OKN007 by magnetic resonance imaging. J Magn Reson Imaging. 2010;31:796-806.

23. Towner RA, Gillespie DL, Schwager A, Saunders DG, Smith N, Njoku CE, et al. Regression of glioma tumor growth in F98 and U87 rat glioma models by the Nitrone OKN-007. Neuro Oncol. 2013;15:330-40.

24. Floyd RA, Kopke RD, Choi CH, Foster SB, Doblas S, Towner RA. Nitrones as therapeutics. Free Radic Biol Med. 2008;45:1361-74.

25. Floyd RA, Chandru HK, He T, Towner R. Anti-cancer activity of nitrones and observations on mechanism of action. Anticancer Agents Med Chem. 2011;11:373-379.

26. Choudhri AF, Klimo P Jr, Auschwitz TS, Whitehead MT, Boop FA. 3T Intraoperative MRI for Management of Pediatric CNS Neoplasms. AJNR Am J Neuroradiol. 2014;35:2382-7.

27. Suero-Abreu GA, Praveen Raju G, Aristizábal O, Volkova E, Wojcinski A, Houston EJ, Pham D, et al. In vivo mn-enhanced MRI for early tumor detection and growth rate analysis in a mouse medulloblastoma model. Neoplasia. 2014;16:993-1006.

28. Wu G, Pang H, Ghimire P, Liu G. (1)H magnetic resonance spectroscopy and diffusion weighted imaging findings of medulloblastoma in 3.0T MRI: A retrospective analysis of 17 cases. Neural Regen Res. 2012;7:2554-9.

29. Panigrahy A, Krieger MD, Gonzalez-Gomez I, Liu X, McComb JG, Finlay JL, et al. Quantitative short echo time 1H-MR spectroscopy of untreated pediatric brain tumors: preoperative diagnosis and characterization. AJNR Am J Neuroradiol. 2006;27:560–572.

30. Tzika AA, Cheng LL, Goumnerova L, Madsen JR, Zurakowski D, Astrakas LG, et al. Biochemical characterization of pediatric brain tumors by using in vivo and ex vivo magnetic resonance spectroscopy. J Neurosurg. 2002;96:1023–1031.

31. Wilson M, Cummins CL, Macpherson L, Sun Y, Natarajan K, Grundy RG, et al. Magnetic resonance spectroscopy metabolite profiles predict survival in paediatric brain tumours. Eur J Cancer. 2013;49:457-64.

32. Albers MJ, Krieger MD, Gonzalez-Gomez I, Gilles FH, McComb JG, Nelson MD, et al. Proton-decoupled 31P MRS in untreated pediatric brain tumors. Magn Reson Med. 2005;53:22–29.

33. Bucci MK, Maity A, Janss AJ, Belasco JB, Fisher MJ, Tochner ZA, et al. Near complete surgical resection predicts a favorable outcome in pediatric patients with nonbrainstem, malignant gliomas: results from a single center in the magnetic resonance imaging era. Cancer. 2004;101:817-24.

34. Steffen-Smith EA, Shih JH, Hipp SJ, Bent R, Warren KE. Proton magnetic resonance spectroscopy predicts survival in children with diffuse intrinsic pontine glioma. J Neurooncol. 2011;105:365-73.

35. Porto L, Kieslich M, Franz K, Lehrbecher T, Pilatus U, Hattingen E. Proton magnetic resonance spectroscopic imaging in pediatric low-grade gliomas. Brain Tumor Pathol. 2010;27:65-70.

36. Blamek S, Larysz D, Ficek K, Sokół M, Miszczyk L, Tarnawski R. MR spectroscopic evaluation of brain tissue damage after treatment forpediatric brain tumors. Acta Neurochir Suppl. 2010;106:183-6.

37. Yeom KW, Lober RM, Andre JB, Fisher PG, Barnes PD, Edwards MS, et al. Prognostic role for diffusion-weighted imaging of pediatric optic pathway glioma. J Neurooncol. 2013;113:479-83.

38. Pillai S, Singhal A, Byrne AT, Dunham C, Cochrane DD, Steinbok P. Diffusion-weighted imaging and pathological correlation in pediatric medulloblastomas-"They are not always restricted!". Childs Nerv Syst. 2011;27:1407-11.

39. Yeom KW, Mitchell LA, Lober RM, Barnes PD, Vogel H, Fisher PG, et al. Arterial spin-labeled perfusion of pediatric brain tumors. AJNR Am J Neuroradiol. 2014;35:395-401.

40. Srinivasan R, Phillips JJ, Vandenberg SR, Polley MY, Bourne G, Au A, et al. Ex vivo MR spectroscopic measure differentiates tumor from treatment effects in GBM. Neuro Oncol. 2010; 12: 1152–1161.

41. Colagrande S, Carbone SF, Carusi LM, Cova M, Villari N. Magnetic resonance diffusion-weighted imaging: extraneurological applications. Radiol Med. 2006;111:392-419.

42. Bozgeyik Z, Onur MR, Poyraz AK. The role of diffusion weighted magnetic resonance imaging in oncologic settings. Quant Imaging Med Surg. 2013; 3: 269–278.

43. Silva AC, Kim SG, Garwood M. Imaging blood flow in brain tumors using arterial spin labeling. Magn Reson Med. 2000;44:169-73.

44. Sorensen AG, Emblem KE, Polaskova P, Jennings D, Kim H, Ancukiewicz M, et al. Increased survival of glioblastoma patients who respond to antiangiogenic therapy with elevated blood perfusion. Cancer Res. 2012;72:402-7.

45. Liu Z, Zhao X, Mao H, Baxter PA, Huang Y, Yu L, et al., Intravenous injection of oncolytic picornavirus SVV-001 prolongs animal survival in a panel of primary tumor-basedorthotopic xenograft mouse models of pediatric glioma. Neuro Oncol. 2013;15,9:1173-85.

46. Shu Q, Wong KK, Antalffy BA, Su JM, Adesina AM, Yu LT, et al., Direct orthotopic transplantation of fresh surgical specimen preserves cancer stem cell pool in clinically relevant mouse models of medulloblastoma and glioma. Stem Cells 2008;26:1414-1424.

47. Baskerville TA, McCabe C, Weir CJ, Macrae IM, Holmes WM. Noninvasive MRI measurement of CBF: evaluating an arterial spin labelling sequence with 99mTc-HMPAO CBF autoradiography in a rat stroke model. J Cereb Blood Flow Metab. 2012;32:973-7.

48. Ralte AM, Sharma MC, Karak AK, Mehta VS, Sarkar C. Clinicopathological features, MIB-1 labeling index and apoptotic index in recurrent astrocytic tumors. Pathol Oncol Res. 2001;7:267-78.

49. Bernstein M, Mitchel SB. Neuro-oncology: The Essentials. New York: Thieme Medical, 2014.

50. Miller RA, Harper JM, Dysko RC, Durkee SJ, Austad SN. Longer life spans and delayed maturation in wild-derived mice. Exp Biol Med (Maywood). 2002;227:500-8.

51. Banerjee, ER. Perspectives in Regenerative Medicine. Springer; 2014.

52. Sorensen AG. Magnetic resonance as a cancer imaging biomarker. J Clin Oncol. 2006; 24:3274-81.

53. Chen J, Huang SL, Li T, Chen XL. In vivo research in astrocytoma cell proliferation with 1H-magnetic resonance spectroscopy: correlation with histopathology and immunohistochemistry. Neuroradiology. 2006;48:312–318.

54. Narayana A, Chang J, Thakur S, Huang W, Karimi S, Hou B, et al. Use of MR spectroscopy and functional imaging in the treatment planning of gliomas. Br J Radiol.2007;80:347–354.

55. Sankar T, Caramanos Z, Assina R, Villemure JG, Leblanc R, Langleben A, et al. Prospective serial proton MR spectroscopic assessment of response to tamoxifen for recurrent malignant glioma. J Neurooncol. 2008;90:63–76.

56. Mirbahai L, Wilson M, Shaw CS, McConville C, Malcomson RD, Griffin JL, et al. 1 H magnetic resonance spectroscopy metabolites as biomarkers for cell cycle arrest and cell death in rat glioma cells. Int J Biochem Cell Biol. 2011;43:990–1001.

57. Stadlbauer A, Buchfelder M, Doelken MT, Hammen T, Ganslandt O. Magnetic resonance spectroscopic imaging for visualization of the infiltration zone of glioma. Cen Eur Neurosurg.2011;72:63–69.

58. Stadlbauer A, Moser E, Gruber S, Buslei R, Nimsky C, Fahlbusch R, et al. Improved delineation of brain tumors: an automated method for segmentation based on pathologic changes of 1 H-MRSI metabolites in gliomas. Neuroimage. 2004;23:454–461.

59. Wilson M, Cummins CL, Macpherson L, Sun Y, Natarajan K, Grundy RG, et al. Magnetic resonance spectroscopy metabolite profiles predict survival in paediatric brain tumours. Eur J Cancer. 2013;49:457-64.

60. Bertholdo D, Watcharakorn A, Castillo M. Brain proton magnetic resonance spectroscopy: introduction and overview. Neuroimaging Clin N Am. 2013;23:359-80.

61. Ramin SL, Tognola WA, Spotti AR. Proton magnetic resonance spectroscopy: clinical applications in patients with brain lesions. Sao Paulo Med J. 2003;121:254-9.

62. Malisza KL, Kozlowski P, Peeling J. A review of in vivo 1H magnetic resonance spectroscopy of cerebral ischemia in rats. Biochem. Cell Biol. 1998;76:487–496.

63. Lupo JM, Cha S, Chang SM, Nelson SJ. Analysis of metabolic indices in regions of abnormal perfusion in patients with high-grade glioma. AJNR Am J Neuroradiol. 2007;28:1455-61.

64. Murphy PS, Rowland IJ, Viviers L, Brada M, Leach MO, Dzik-Jurasz AS. Could assessment of glioma methylene lipid resonance by in vivo (1)H-MRS be of clinical value? Br J Radiol. 2003;76:459–463.

65. Negendank W, Li CW, Padavic-Shaller K, Murphy-Boesch J, Brown TR. Phospholipid metabolites in 1H-decoupled 31P MRS in vivo in human cancer: implications for experimental models and clinical studies. Anticancer Res.1996;16:1539–1544.

66. Kaminogo M, Ishimaru H, Morikawa M. Diagnostic potential of short echo time MR spectroscopy of gliomas with single-voxel and point-resolved spatially localised proton spectroscopy of brain. Neuroradiology. 2001;43(5):353–363.

67. Astrakas LG, Zurakowski D, Tzika AA. Noninvasive magnetic resonance spectroscopic imaging biomarkers to predict the clinical grade of pediatric brain tumors. Clin Cancer Res. 2004;10(24):8220–8228.

68. Delikatny EJ, Cooper WA, Brammah S, Sathasivam N, Rideout DC. Nuclear magnetic resonance-visible lipids induced by cationic lipophilic chemotherapeutic agents are accompanied by increased lipid droplet formation and damaged mitochondria. Cancer Res. 2002;62(5):1394–1400.

69. Griffin JL, Lehtimaki KK, Valonen PK. Assignment of 1H nuclear magnetic resonance visible polyunsaturated fatty acids in BT4C gliomas undergoing ganciclovir–thymidine kinase gene therapy-induced programmed cell death. Cancer Res. 2003;63:3195–3201.

70. Zoula S, Rijken PF, Peters JP. Pimonidazole binding in C6 rat brain glioma: relation with lipid droplet detection. Br J Cancer. 2003;88(9):1439–1444.

71. Kousi E, Tsougos I, Tsolaki E, Fountas KN, Theodorou K, Fezoulidis I, et al. Spectroscopic evaluation of glioma grading at 3T: the combined role of short and long TE. ScientificWorldJournal. 2012;2012:546171.

72. Delikatny EJ, Chawla S, Leung DJ, Poptani H. MR-visible lipids and the tumor microenvironment. NMR Biomed. 2011;24:592-611.

73. Negendank W, Sauter R. Intratumoral lipids in 1H MRS in vivo in brain tumors: experience of the Siemens cooperative clinical trial. Anticancer Res. 1996;16:1533-8.

74. Gillies RJ, Morse DL. In vivo magnetic resonance spectroscopy in cancer. Annu Rev Biomed Eng. 2005;7:287-326.

75. Blankenberg FG, Katsikis PD, Storrs RW, Beaulieu C, Spielman D, Chen JY, et al. Quantitative analysis of apoptotic cell death using proton nuclear magnetic resonance spectroscopy. Blood. 1997;89:3778-86.

76. Li X, Vigneron DB, Cha S, Graves EE, Crawford F, Chang SM, et al. Relationship of MR-derived lactate, mobile lipids, and relative blood volume for gliomas in vivo. AJNR Am J Neuroradiol. 2005;26:760-9.

77. de Certaines JD, Le Moyec L, Sequin F, Eliat PA, Constans JM. Nuclear Magnetic Resonance Spectroscopy of Lipids in Cancer. Curr Org Chem. 2007; 11:529–546.

78. Hakumäki JM, Kauppinen RA. 1H NMR visible lipids in the life and death of cells. Trends Biochem Sci. 2000;25:357-62.

79. Bulik M, Jancalek R, Vanicek J, Skoch A, Mechl M. Potential of MR spectroscopy for assessment of glioma grading. Clin Neurol Neurosurg. 2013;115:146-53.

80. Kuesel AC, Sutherland GR, Halliday W, Smith IC. 1H MRS of high grade astrocytomas: mobile lipid accumulation in necrotic tissue. NMR Biomed. 1994;7:149-55.

81. Barba I, Cabañas ME, Arús C. The relationship between nuclear magnetic resonance-visible lipids, lipid droplets, and cell proliferation in cultured C6 cells. Cancer Res. 1999; 59:1861-8.

82. Kao HW, Chiang SW, Chung HW, Tsai FY, Chen CY. Advanced MR imaging of gliomas: an update. Biomed Res Int. 2013;2013:970586.

83. Barker FG 2nd, Davis RL, Chang SM, Prados MD. Necrosis as a prognostic factor in glioblastoma multiforme. Cancer. 1996;77:1161-6.

84. Homma T, Fukushima T, Vaccarella S, Yonekawa Y, Di Patre PL, Franceschi S, et al. Correlation among pathology, genotype, and patient outcomes in glioblastoma. J Neuropathol Exp Neurol. 2006;65:846-54.

85. Miller CR, Dunham CP, Scheithauer BW, Perry A. Significance of necrosis in grading of oligodendroglial neoplasms: a clinicopathologic and genetic study of newly diagnosed high-grade gliomas. J Clin Oncol. 2006;24:5419-26.

86. Pierallini A, Bonamini M, Pantano P, Palmeggiani F, Raguso M, Osti MF, et al. Radiological assessment of necrosis in glioblastoma: variability and prognostic value. Neuroradiology. 1998;40:150-3.

87. McKnight TR, Lamborn KR, Love TD, Berger MS, Chang S, Dillon WP, et al. Correlation of magnetic resonance spectroscopic and growth characteristics within Grades II and III gliomas. J Neurosurg. 2007;106:660–666.

88. Warren KE, Frank JA, Black JL, Hill RS, Duyn JH, Aikin AA, et al. Proton magnetic resonance spectroscopic imaging in children with recurrent primary brain tumors. J Clin Oncol. 2000; 18:1020-6.

89. Tzika AA, Astrakas LG, Zarifi MK, Zurakowski D, Poussaint TY, Goumnerova L, et al. Spectroscopic and perfusion magnetic resonance imaging predictors of progression in pediatric brain tumors. Cancer. 2004; 100:1246-56.

90. Marcus KJ, Astrakas LG, Zurakowski D, Zarifi MK, Mintzopoulos D, Poussaint TY, et al. Predicting survival of children with CNS tumors using proton magnetic resonance spectroscopic imaging biomarkers. Int J Oncol. 2007;30:651-7.

91. Heijmen L, Verstappen MC, Ter Voert EE, Punt CJ, Oyen WJ, de Geus-Oei LF, et al. Tumour response prediction by diffusion-weighted MR imaging: ready forclinical use? Crit Rev Oncol Hematol. 2012;83:194-207.

92. Castillo M, Smith JK, Kwock L, Wilber K. Apparent diffusion coefficients in the evaluation of high-grade cerebral gliomas. AJNR Am J Neuroradiol. 2001; 22:60-4.

93. Ross BD, Moffat BA, Lawrence TS, Mukherji SK, Gebarski SS, Quint DJ, et al. Evaluation of cancer therapy using diffusion magnetic resonance imaging. Mol Cancer Ther. 2003; 2:581-7.

94. Chenevert TL, Stegman LD, Taylor JM, Robertson PL, Greenberg HS, Rehemtulla A, et al. Diffusion magnetic resonance imaging: an early surrogate marker of therapeutic efficacy in brain tumors. J Natl Cancer Inst. 2000;92:2029-36.

95. Mardor Y, Roth Y, Ochershvilli A, Spiegelmann R, Tichler T, Daniels D, et al. Pretreatment prediction of brain tumors' response to radiation therapy using high b-value diffusion-weighted MRI. Neoplasia. 2004;6:136-42.

96. Kim SG. Perfusion MR imaging: Evolution from initial development to functional studies. Neuroimage. 2012;62:672-5.

97. Schraml C, Schwenzer NF, Claussen CD, Martirosian P. Examination of Tissue Perfusion by Arterial Spin Labeling (ASL). Curr Radiol Rep. 2013;1: 93-101

98. Silva AC, Kim SG, Garwood M. Imaging blood flow in brain tumors using arterial spin labeling. Magn Reson Med. 2000;44:169-73.

99. Jain RK. Normalizing tumor vasculature with anti-angiogenic therapy: a new paradigm for combination therapy. Nat Med. 2001;7:987–9.

100. Goel S, Duda DG, Xu L, Munn LL, Boucher Y, Fukumura D, et al. Normalization of the vasculature for treatment of cancer and other diseases. Physiological Reviews. 2011;91:1071–121.

101. Jain RK. Normalization of tumor vasculature: an emerging concept in antiangiogenic therapy. Science. 2005;307:58–62.

102. Xu W, Liu LZ, Loizidou M, Ahmed M, Charles IG. The role of nitric oxide in cancer. Cell Res. 2002;12:311–320.

103. Anda T, Yamashita H, Khalid H, Tsutsumi K, Fujita H, Tokunaga Y, et al. Effect of tumor necrosis factor-alpha on the permeability of bovine brain microvessel endothelial cell monolayers. Neurol Res. 1997;19:369–376.

104. Huse JT, Holland EC. Targeting brain cancer: advances in the molecular pathology of malignant glioma and medulloblastoma. Nat Rev Cancer. 2010;10:319-31.

105. Furnari FB, Fenton T, Bachoo RM, Mukasa A, Stommel JM, Stegh A, et al. Malignant astrocytic glioma: genetics, biology, and paths to treatment. Genes & development. 2007;21:2683–710.

106. Paugh BS, Broniscer A, Qu C, Miller CP, Zhang J, Tatevossian RG, et al. Genome-wide analyses identify recurrent amplifications of receptor tyrosine kinases and cell-cycle regulatory genes in diffuse intrinsic pontine glioma. Journal of clinical oncology: official journal of the American Society of Clinical Oncology.2011;29:3999–4006.

107. Paugh BS, Qu C, Jones C, Liu Z, Adamowicz-Brice M, Zhang J, et al. Integrated molecular genetic profiling of pediatric high-grade gliomas reveals key differences with the adult disease. Journal of clinical oncology: official journal of the American Society of Clinical Oncology. 2010;28:3061–8.

108. Puget S, Philippe C, Bax DA, Job B, Varlet P, Junier MP, et al. Mesenchymal transition and PDGFRA amplification/mutation are key distinct oncogenic events in pediatric diffuse intrinsic pontine gliomas. PloS one. 2012;7:e30313.

109. Zarghooni M, Bartels U, Lee E, Buczkowicz P, Morrison A, Huang A, et al. Whole-genome profiling of pediatric diffuse intrinsic pontine gliomas highlights platelet-derived growth factor receptor alpha and poly (ADP-ribose) polymerase as potential therapeutic targets. Journal of clinical oncology: official journal of the American Society of Clinical Oncology. 2010;28:1337–44.

110. Huse JT, Holland EC. Targeting brain cancer: advances in the molecular pathology of malignant glioma and medulloblastoma. Nat Rev Cancer. 2010;10:319-31.

111. Schwartzentruber J, Korshunov A, Liu XY, Jones DT, Pfaff E, Jacob K, et al. Driver mutations in histone H3. 3 and chromatin remodelling genes in paediatric glioblastoma. Nature. 2012;482:226–31.

112. Thorarinsdottir HK, Santi M, McCarter R, Rushing EJ, Cornelison R, Jales A, et al. Protein expression of platelet derived growth factor receptor correlates with malignant histology and PTEN with survival in childhood gliomas. Clin Cancer Res.2008;14:3386–3394.

113. Blom T, Roselli A, Häyry V, Tynninen O, Wartiovaara K, Korja M, et al. Amplification and overexpression of KIT, PDGFRA, and VEGFR2 in medulloblastomas and primitive neuroectodermal tumors. J Neurooncol. 2010;97:217–224.

114. Lemjabbar-Alaoui H, van Zante A, Singer MS, Xue Q, Wang YQ, Tsay D, et al. Sulf-2, a heparan sulfate endosulfatase, promotes human lung carcinogenesis. Oncogene. 2010;29:635-46.

115. Morimoto-Tomita M, Uchimura K, Bistrup A, Lum DH, Egeblad M, Boudreau N, et al. Sulf-2, a proangiogenic heparan sulfate endosulfatase, is upregulated in breast cancer. Neoplasia. 2005;7:1001-10.

116. Lai JP, Oseini AM, Moser CD, Yu C, Elsawa SF, Hu C, et al. The oncogenic effect of sulfatase 2 in human hepatocellular carcinoma is mediated in part by glypican 3-dependent Wnt activation. Hepatology. 2010;52:1680-9.

117. Hur K, Han TS, Jung EJ, Yu J, Lee HJ, Kim WH, et al. Up-regulated expression of sulfatases (SULF1 and SULF2) as prognostic and metastasis predictive markers in human gastric cancer. J Pathol. 2012; 228:88-98.

118. Wade A, Robinson AE, Engler JR, Petritsch C, James CD, Phillips JJ. Proteoglycans and their roles in brain cancer. FEBS J. 2013; 280:2399-417.

119. Phillips JJ, Huillard E, Robinson AE, Ward A, Lum DH, Polley MY, et al. Heparan sulfate sulfatase SULF2 regulates PDGFRα signaling and growth in humanand mouse malignant glioma. J Clin Invest. 2012; 122:911-22.

120. Hocking A, Shinomura T, McQuillan D. Leucine rich repeat glycoproteins of the extracellular matrix. Matrix Biol. 1998;17:1-19.

121. Krusius T, Ruoslathi E. Primary structure of an extracellular matrix proteoglycan core protein deduced from cloned cDNA. Proc Natl Acad Sci USA 1986;83:7683-7687.

122. Thieszen S, Rosenquist T. Expression of collagens and decorin during aortic arch artery development: implications for matrix pattern formation. Matrix Biol. 1995; 14:573-582.

123. Merle B, Malaval L, Lawler J, Delmas P, Clezardin P. Decorin inhibits cell attachment to thrombospondin-1 by binding to a KKTR-dependent cell adhesive site present within the N-terminal domain of thrombospondin-1. J Cell Biochem .1997;67:75-83

124. Merle B, Durussel L, Delmas PD, Clezardin P. Decorin inhibits cell migration through a process requiring its glycosaminoglycan side chain. J Cell Biochem. 1999;75:538-546.

125. Nash MA, Loercher AE, Freedman RS. In vitro growth inhibition of ovarian cancer cells by decorin: synergism of action between decorin and carboplatin. Cancer Res. 1999;59:6192-6196.

126. Baghy K, Horváth Z, Regős E, Kiss K, Schaff Z, Iozzo RV, et al. Decorin interferes with platelet-derived growth factor receptor signaling in experimental hepatocarcinogenesis. FEBS J. 2013;280:2150-64.

127. Santra M, Katakowski M, Zhang RL, Zhang ZG, Meng H, Jiang F, et al. Protection of adult mouse progenitor cells and human glioma cells by de novo decorin expression in an oxygen- and glucose-deprived cell culture model system. J Cereb Blood Flow Metab. 2006;26:1311-22.

128. Neill T, Painter H, Buraschi S, Owens RT, Lisanti MP, Schaefer L, et al. Decorin antagonizes the angiogenic network: concurrent inhibition of Met, hypoxia inducible factor 1α, vascular endothelial growth factor A, and induction of thrombospondin-1 and TIMP3. J Biol Chem. 2012;287:5492-506.

129. Grant DS, Yenisey C, Rose RW, Tootell M, Santra M, Iozzo RV. Decorin suppresses tumor cell-mediated angiogenesis. Oncogene. 2002; 21:4765-77.

130. Zheng X, Gai X, Han S, Moser CD, Hu C, Shire AM, et al. The Human Sulfatase 2 Inhibitor 2,4-Disulfonylphenyl-tert-Butylnitrone (OKN-007) has an Antitumor Effect in Hepatocellular Carcinoma Mediated via Suppression of TGFB1/SMAD2 and Hedgehog/GLI1 Signaling. Genes Chromosomes Cancer. 2013; 52:225-36.

131. Bernfield M1, Götte M, Park PW, Reizes O, Fitzgerald ML, Lincecum J, Zako M. Functions of cell surface heparan sulfate proteoglycans. Annu Rev Biochem. 1999;68:729-77.

CHAPTER V

General conclusions

The overall hypothesis (H_0) of my PhD dissertation was to explore the anticancer properities in different glioma animal models. This principal hypothesis was evaluated in four different studies, which were based on the OKN-007 activity to decrease tumor necrosis, tumor cell proliferation, and free radical and VEGFR-2 levels in adult gliomas, as well as based on OKN-007 anticancer activity in a pediatric glioma mouse model (Fig 5.1).

Overall hypothesis (H_0): OKN-007 is an effective anti-glioma agent

<u>Adult glioma models</u>

- H_1: OKN-007 decreases tumor necrosis and cell proliferation in a F98 rat glioma model
- H_2: OKN-007 decreases free radical levels in a F98 rat glioma model
- H_3: OKN-007 decreases VEGFR-2 levels in a GL261 mouse glioma model

<u>Pediatric glioma model</u>

- H_4: OKN-007 has anticancer activity in a pediatric glioma mouse model

Figure 5.1 - Hypotheses tested in this PhD dissertation.

These studies demonstrated that OKN-007 was able to increase the survival time, decrease tumor volume, tumor cell proliferation, tumor necrosis, and tumor angiogenesis in both adult and pediatric gliomas (Fig 5.2). OKN-007 also increased tumor cell apoptosis and decreased free radical levels in adult gliomas (Fig 5.2). Further studies to establish the target pathway of OKN-007, which may be TGFβ1, will need to be conducted. Furthermore, OKN-007 decreased the immunoexpression of PDGFR-α and SULF-2, and increased the immunoexpression of decorin in pediatric gliomas (Fig 5.2). The PDGFR pathway may be a possible target for OKN-007 in pediatric gliomas, which will need to be further studied.

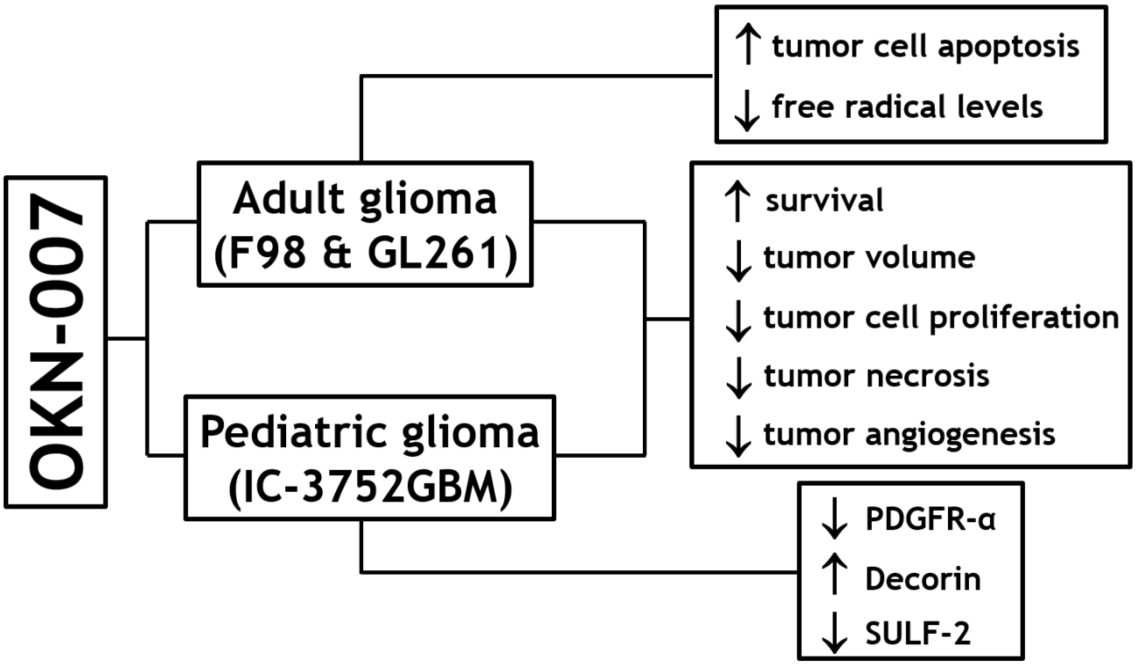

Figure 5.2 – Schematic summary for the results obtained in this PhD dissertation.

VITA

Patricia Coutinho de Souza

Candidate for the Degree of

Doctor of Philosophy

Thesis: ASSESSMENT OF THE THERAPEUTIC EFFECTS OF OKN-007 IN RODENT GLIOMA MODELS USING ADVANCED MRI TECHNIQUES

Major Field: Veterinary Biomedical Sciences

Biographical:

Education:

Completed the requirements for the Doctor of Philosophy in Veterinary Biomedical Sciences at Oklahoma State University, Stillwater, Oklahoma in May, 2015.

Completed the requirements for the Master of Science in Experimental and Comparative Pathology at University of São Paulo, São Paulo, Brazil in February, 2010.

Completed the requirements for Residency Training in Veterinary Anatomic Pathology Federal University of Minas Gerais, School of Veterinary Medicine, Belo Horizonte, Minas Gerais, Brazil in February, 2007.

Doctor of Veterinary Medicine at Federal University of Viçosa, Viçosa, Minas Gerais, Brazil in January, 2005.

Professional Memberships:

International Society for Magnetic Resonance in Medicine
American Association for Cancer Research